Source Regions of Sea Salt Aerosols in Dome C Under Present Day and Last Glacial Maximum Conditions

Master Thesis

Faculty of Science, University of Bern

Linnea Bühler

April 24, 2023

Supervisors:

Prof. Dr. C. C. Raible

Prof. Dr. H. Fischer

Climate and Environmental Physics

Physics Institute, University of Bern

Abstract

Sea salt aerosol (SSA) concentration in ice cores varies over long time scales, most noticeably between glacial and interglacial times. The trajectories and formation processes of SSA are impacted by these changes and their concentrations can therefore serve as a proxy for changes in atmospheric circulation patterns above and around Antarctica. This study investigates the reasons for the changes in SSA concentration in ice cores from Dome C, Antarctica, between the preindustrial period (PI) and the Last Glacial Maximum (LGM), and the source regions of SSAs, and how they differ for the two time periods. To obtain the pathways of air parcels and the aerosols' source regions, 10-day back-trajectories are calculated using the FLEXTRA trajectory model. The wind field inputs are from CESM1.2 for the PI (about 1850 CE) and the LGM (about 20.000 years BP). The ERA5 reanalysis data for present-day conditions (PD, 1990 to 2000) is used to test the validity of the CESM1.2 model. The potentially aerosol-carrying air parcels are then filtered by applying thresholds needed for the formation, transport, and deposition of SSA, whose sensitivities are analyzed together with the sensitivity of spatial and temporal resolution of the data. The temporal resolution of one hour leads to an increase in trajectories of 23% compared to the resolution of six hours, while changing the spatial resolution from $1^\circ \times 1^\circ$ to $0.25^\circ \times 0.25^\circ$ has very little impact on trajectories in the summer, but leads to a reduction of trajectories of about 70% in winter. The comparison of ERA5 and CESM1.2 in the same temporal and spatial resolutions yields a stronger peak in CESM1.2 in trajectory numbers in January and December, which mirrors higher atmospheric SSA concentrations in coastal Antarctic stations in austral summer.

The analysis regarding the changes in sea salt aerosol concentration and source regions between the LGM and the PI carried out with CESM1.2 data, finds that wet deposition plays a minor role in depositing aerosols at Dome C, with 10% of the total deposition flux in the

PI, and only 2% in the LGM. This can be attributed to the small precipitation rates in the LGM where water vapor and precipitation in Antarctica are lower still than in present-day conditions. The total deposition flux, assumed to be proportional to the number of points where sea salt aerosols can be taken up, is twice as large in the LGM as in the PI, also because of lower precipitation and thereby less wash-out en route. Because accumulation rates are twice as high in the PI as in the LGM, this leads to a final sea salt concentration in the ice from calculated trajectories that is approximately 4 times higher in the LGM than in the PI, which corresponds to sea salt concentrations measured in the ice in Dome C for the two time periods. The main source region in the LGM for Dome C stretches from the Amundsen Sea to the Amery Ice Shelf, and largely consists of sea ice aerosols, while the largest number of open ocean aerosols originates from the Southern Ocean between Antarctica and Australia, and fewer from all around the Antarctic continent. The PI open ocean aerosols also derive mostly from south of Australia, while weaker source regions are located around Antarctica. The sea ice source is much less pronounced in the PI (35%) than in the LGM (63%), because of less overall sea ice extent. No continuous pressure pattern anomalies between the LGM and the PI are present annually. Pressure differences between the two time periods can therefore not be determined to be the cause for the strong difference in sea salt aerosol concentrations in the ice.

Contents

1 Introduction **1**

2 State of Knowledge **5**

2.1 Sea Salt Aerosols 5

2.1.1 Formation of Aerosols 7

2.1.2 Transport and Deposition of Aerosols 10

2.2 Meteorology of Antarctica 12

3 Data and Methods **17**

3.1 Datasets 17

3.1.1 Reanalysis ERA5 17

3.1.2 The Community Earth System Model Version 1.2 21

3.2 Methods 24

3.2.1 FLEXTRA - Trajectory calculation 25

3.2.2 Pre-Processing 28

3.2.3 Thresholds and data preparation 29

4 Results **33**

4.1 Testing of trajectory criteria 34

4.1.1 Wet deposition criterion 35

4.1.2 Transport criterion 35

4.1.3 Input height criterion 36

4.1.4 Formation criterion 37

4.1.5 End height 40
4.2 Impact of temporal and spatial resolution on trajectories 40
4.3 Comparison of ERA5 and CESM1.2 45
4.4 LGM and PI 52
4.4.1 Impact of LGM and PI on Sea Salt Aerosol trajectories 52
4.4.2 Impact of large-scale circulation patterns 66

5 Discussion **75**

6 Conclusion and outlook **81**

7 Appendix **83**

References **89**

Chapter 1

Introduction

Ice cores are one of the longest climate archives on Earth. Due to the low accumulation rates in East Antarctica, resulting in very thin layers of ice per year, the ice covers very long time periods [*Casado et al.*, 2018], e.g. up to 420,000 years at Vostok [*Petit et al.*, 1999], and 800,000 years at Dome C [*EPICA Community Members*, 2004; *Jouzel and Masson-Delmotte*, 2007]. Gaining and processing information about climate proxies from ice core data is a crucial step for understanding past climate variations. This understanding can foster our knowledge of the causes and effects of changes in the climate system. The resulting process understanding, in turn, will also help to model future climate. Aerosols are one crucial component of ice cores that contain information about past climate, as they change the atmospheric radiation budget by scattering and absorbing solar radiation, and serve as cloud condensation nuclei, hence influencing the climate [*Wagner et al.*, 2004]. Moreover, their concentration in the ice correlates with their concentration in the air. Since different types of aerosols require specific conditions for their formation and transport, conclusions on past atmospheric conditions and climate conditions in their source area can be drawn based on the composition of the ice cores' layers.

This study will focus on sea salt aerosols (SSAs), one of the most abundant aerosols from natural sources, and at the same time the ones that most notably impact atmospheric radiation, particularly above the sea [*Haywood et al.*, 1999]. They range in size from several nanometers up to 100 μm [*Yu et al.*, 2019] and their concentration in Antarctica has been

continuously measured since 1983 [*Weller et al.*, 2011]. Because of the low accumulation rates, the distinction between annual layers is not very accurate in the interior of East Antarctica, resulting in the measurement of SSA concentration on multiannual averages instead of annual resolution (cf. Figure 1.1). In addition, the source regions of SSAs are unknown, as is how much the regions might differ between glacial and interglacial times. Hence, it is necessary to determine the source regions using a back-trajectory tool, with wind fields from a reanalysis and model simulations for the present and the past. The trajectories and their determined source regions can then help in reconstructing the atmospheric dynamics.

Trajectories will be tracked from EPICA Dome C in East Antarctica (cf. Figure 1.2), since the research group of Past Climate and Biogeochemical Studies on Ice Cores at the University of Bern has conducted studies on the ice cores collected from Dome C.

From Dome C, back-trajectories will be calculated in order to find the most prominent source regions of the sea salt aerosols, both for recent atmospheric conditions and for the Last Glacial Maximum (LGM, around 20 000 years BP). In recent times, the reanalysis dataset ERA5 with a horizontal resolution of 0.25° is available. For the LGM, the model output of CESM1.2 is used. Due to the differences between the two datasets, the comparability needs to be tested

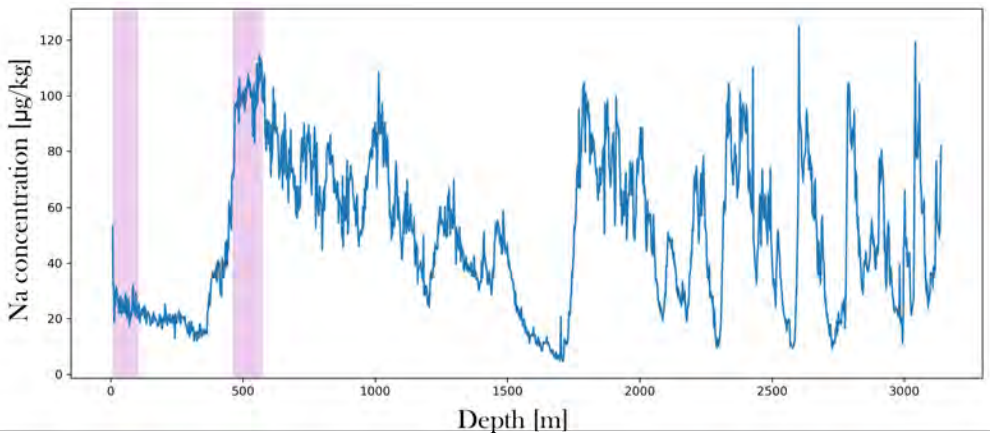

Figure 1.1: Concentration of the sea salt aerosol Na^+ in Dome C. Colored are the depths that correlate to Preindustrial to 20th century and Last Glacial Maximum (20-18 ky BP). Source: *Wolff et al.* [2006].

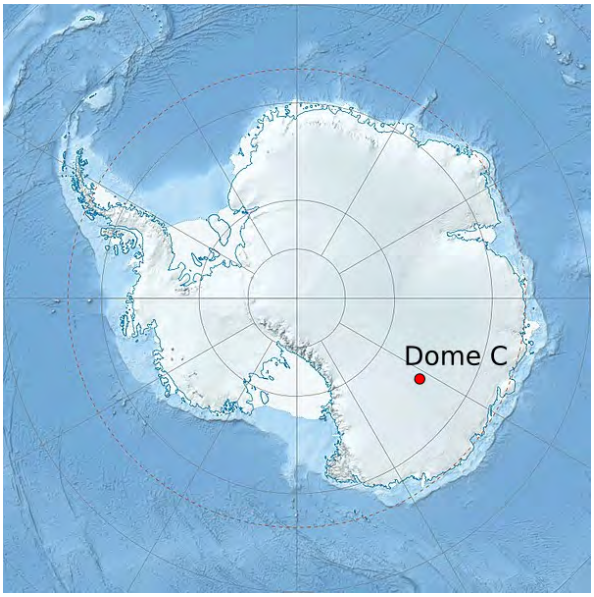

Figure 1.2: Location of EPICA Dome C. Source: *Wikipedia contributors* [2022a].

beforehand to determine the influence of both spatial (0.25° and 1°) and temporal (1-hourly and 6-hourly) resolution. Subsequently, ERA5 and CESM1.2 will be compared for a similar period of time, this being 1990 to 1999 (present day, PD) and for 10 years with conditions from approximately 1850 (Preindustrial, PI). This will facilitate the estimation of differences between the reanalysis and the model. Thereafter, the back trajectories for the two periods are calculated using the FLEXTRA trajectory method.

The trajectories allow a closer observation of the processes that influence the concentration of aerosols on the way from their source to the deposition. This means that thresholds for the processes of formation, transportation, and deposition will be applied to filter out trajectories where SSAs are unlikely to be present. The sensitivity of thresholds for these processes needs to be analyzed before the trajectories are filtered, and analyzed in terms of the SSA potential source regions.

Therefore, the main research questions of this thesis are:

- What are the source regions of sea salt aerosols deposited at Dome C? How do the source regions differ for the Preindustrial and the Last Glacial Maximum?

- How well can CESM1.2 represent the trajectories?

- Which processes are important in explaining the different source regions between the Preindustrial and the Last Glacial Maximum?

To this end, the next chapters will first give an overview of sea salt aerosols, their formation, and transport processes and properties, and the atmospheric conditions above Antarctica (Chapter 2). Chapter 3 focuses on the two datasets ECMWF ERA5 and Community Earth System Model Version 1.2, the FLEXTRA trajectory calculation tool, and methods used in this study. It also highlights the threshold parameters used for filtering the trajectories. Chapter 4 describes the results of the filtering sensitivity and the spatial and temporal sensitivity analyses and shows the trajectory source regions and their changes between LGM and PI. Subsequently, we will discuss their meaning and potential reasons for the changes in Chapter 5.

Chapter 2

State of Knowledge

As the name suggests, sea salt aerosols originate from the ocean surface, in particular from salty seawater. Antarctica, surrounded by the Southern Ocean in all directions, is thus an obvious candidate for aerosol deposition. However, it is not easy to identify which part of the Southern Ocean the aerosols come from. To constrain the source regions of SSAs deposited in Antarctica, it is important to understand the underlying processes which consist of formation, transport, and deposition, as well as the characteristic climatic conditions that are in force in Antarctica. To this end, Section 2.1 gives the foundations of what we know about SSAs, the conditions needed for their formation, both above open ocean and on sea ice, how and when transport of aerosols is possible, and in what form deposition of aerosols takes place. Subsequently, section 2.2 presents an overview of the meteorology of Antarctica during the LGM, and how climatic changes have affected it during the Preindustrial and over the last hundred years.

2.1 Sea Salt Aerosols

Generally speaking, atmospheric aerosols are small, either solid or liquid particles varying from a couple of nanometers to several hundred µm in size, that greatly affect the Earth's radiative balance. Due to the different types of aerosols and their direct and indirect influences, any effects on climate associated with aerosols still have large uncertainties. Unlike aerosols that have a positive radiative forcing, such as Black Carbon from fossil fuel combustion [*Matsui*

et al., 2018], SSAs have a more intricate impact on the global climate. They directly scatter solar radiation but can also indirectly act as cloud condensation nuclei, influencing cloud microphysical processes and precipitation patterns [*Lewis and Schwartz*, 2004]. Overall, one differentiates between primarily and secondarily produced aerosols, and those of natural and anthropogenic sources. While primary production describes the formation of the aerosol particle right at the source, secondary production involves a chemical conversion of a gas to a particle which then constitutes the aerosol [*lv et al.*, 2020]. Sea salt aerosols - as depicted in Figure 2.1 - are natural, primary aerosols, originating from the sea, and have a diameter of several nanometers to hundred micrometers. Studies have shown that in the Southern Ocean, the sea salt aerosols of 1 to 2 µm radius contribute the most SSA mass to the atmosphere [*Murphy et al.*, 2019; *Yu et al.*, 2019]. After their formation, SSAs are transported to and later deposited at their end site. If their deposition takes place in Antarctica, the SSAs are buried under subsequent precipitation and will be archived in the ice. Thus, the SSA concentrations can be directly measured using ice cores, but the determination of their actual source regions is not straightforward, since the following three main processes determine the aerosols' life cycle, as can be seen in Figure 2.2: (i) formation at the source region, (ii) transport of the aerosol, and (iii) its deposition which will be further analyzed in 2.1.1 and 2.1.2, respectively.

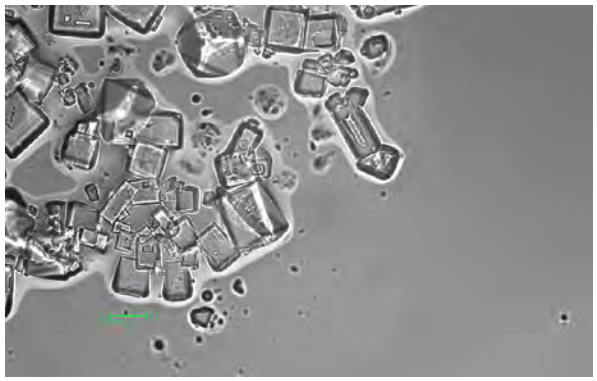

Figure 2.1: SSAs under the microscope. Source: *Petty* [2009].

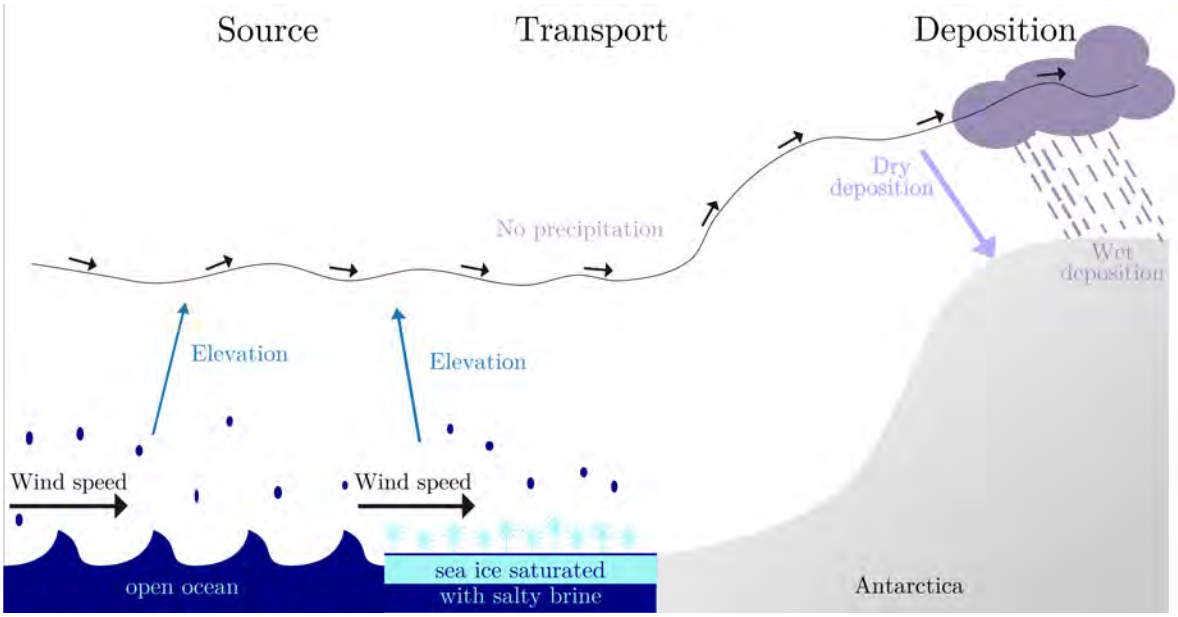

Figure 2.2: Processes involved in the production, transport, and deposition of SSAs.

2.1.1 Formation of Aerosols

As already mentioned above, SSAs originate either from the open sea or sea ice. For both processes, wind speed close to the ocean surface is an essential prerequisite for SSA formation. For open ocean formation, the wind drives surface waters to a higher speed than the water below, forming waves that trap air bubbles in the water when they break, as highlighted in Figure 2.3. For this to occur, a minimal relative wind velocity of 4 m s^{-1} is required [*Prijith et al.*, 2013; *O'Dowd and de Leeuw*, 2007; *Yoav et al.*, 2010; *Lewis and Schwartz*, 2004]. Subsequently, as shown in Figure 2.3, the trapped bubbles ascend to the ocean's surface and burst, forming the film and the jet drops shown in Figure 2.3. The spray splashing upwards from the topmost water layer constitutes the film drops. Every bubble generates up to hundreds of individual film drops, with sizes of 0.01–2 µm [*Richter and Veron*, 2016]. A jet drop, on the other hand, is formed by the vertical column of water inside the already burst, closing bubble, from the water that floods back into the empty space [*Lewis and Schwartz*, 2004]. For each bursting bubble, only a few jet drops form, and depending on the size of their respective parent bubble, their diameters range between 2 µm and 100 µm [*Richter and*

Veron, 2016]. Theoretically, owing to their small sizes, both film and jet drops possess the potential to become aerosol particles - however, besides wind speed, the respective angle at which they have been expelled from the water is also crucial. If this angle is too shallow, the drops fall back into the ocean before being carried away by the wind [*Lhuissier and Villermaux*, 2012]. Even though higher wind speeds ($\geq$ 7 m s^{-1}, *Veron* [2015]) additionally generate spume drops which are simply scraped water drops off a crashed wave [*Lewis and Schwartz*, 2004], the spume drops do not contribute to SSA formation. This is due to their large size of up to several millimeters in radius [*Veron et al.*, 2012], thus, they are not small enough to be taken up into the air [*Monahan et al.*, 1986].

Sea salt aerosols can also be formed on sea ice which is a rather recent discovery. This is attributed to the fact that they make up only a small part of the overall SSA concentration,

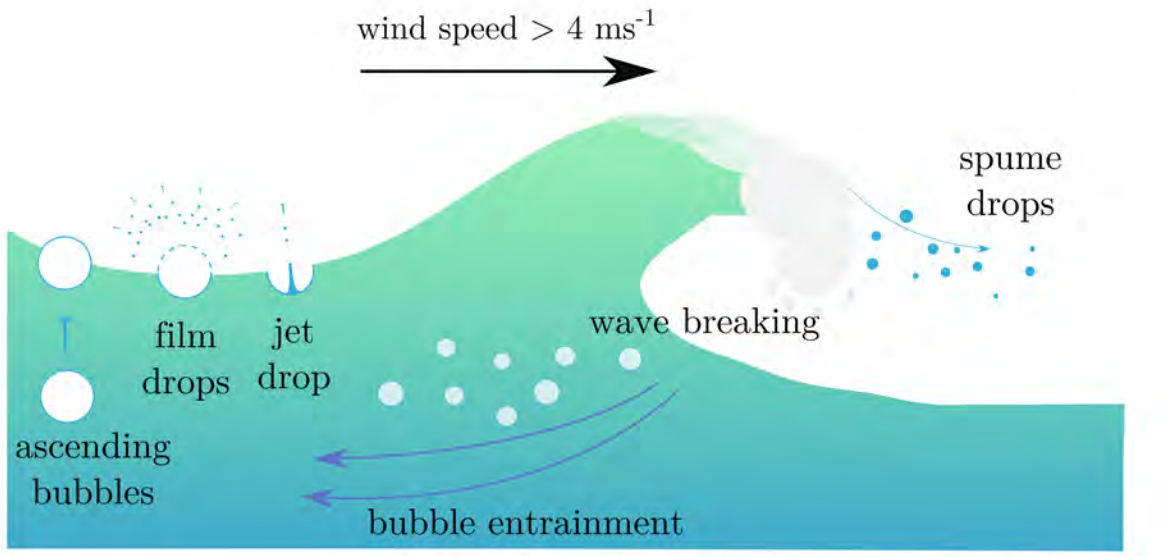

Figure 2.3: Formation of open ocean SSAs. Breaking waves lead to bubble entrainment in the water. Ascending bubbles burst as they reach the surface, and the resulting spray is film drops. When water floods back into the empty space, the rush forms jet drops that are ejected vertically from the water's surface.

due to the comparably much smaller surface area of sea ice [*Frey et al.*, 2019]. However, recent studies have observed a peak in large SSA particles during winter and spring months and during glacial periods [*Rankin and Wolff*, 2003; *Jourdain et al.*, 2008; *Legrand et al.*, 2017]. Since these colder periods coincide with maxima of sea ice extent, the theory that only open ocean can produce SSAs fails to explain the increase in SSAs of these sizes and the fact that deposition regions are significantly farther away from the open ocean. Hence, the peak can only be explained by sea ice being a substantial additional formation area. Moreover, a sulfate depletion of SSAs above Antarctica compared to its abundance in sea water can only originate from sea ice, strongly supporting this theory [*Frey et al.*, 2019]. Typically, sea ice aerosols are produced by two source processes, either blowing snow or frost flowers. Blowing snow describes the lifting of surface snow on sea ice, mostly during strong winds, also referred to as blowing snow events. For blowing snow to introduce sea salt aerosol into the atmosphere, waves spilling over the ice shelves need to saturate the snow with salty sea water, called salty brine, which is necessary for the presence of salt in the snow. This leads to the process being spatially limited to the ice margins or leads in the sea ice, where ice can be flooded by seawater. When the strong winds take up salty snow and lift it high enough, the snow sublimates, leaving behind only the SSA [*Rhodes et al.*, 2017]. Note that the snow cannot sublimate near the ocean surface because the atmospheric layer is nearly fully saturated with water. However, since the saturation decreases with increasing height [*Mann et al.*, 2000], the sublimation of snow is possible at higher altitudes [*Déry and Yau*, 2001]. Therefore, according to *Frey et al.* [2019], the minimum wind velocity U_t for blowing snow to occur depends on the ambient temperature T_a [°C]:

$$U_t = U_{t0} + 0.0033(T_a + 27.27)^2, \tag{2.1}$$

where U_{t0} =6.975 ms^{-1} is the smallest possible value for U_t. The second process includes so-called frost flowers (cf. Figure 2.4), which are ice crystals, saturated with salty brine, that grow from the sea ice surface [*Perovich and Richter-Menge*, 1994]. Their formation takes place in cold and mostly calm conditions, and most often on young sea ice [*Xu et al.*, 2016]. However, a minimum wind speed is needed here to destroy the finely structured frost flowers, and to take them up in the air to become aerosols [*Obbard et al.*, 2009]. Similar to blowing

snow, frost flower production is assumed to onset at a velocity of 7 ms^{-1} because of the stability of the crystals [*Roscoe et al.*, 2011; *Obbard et al.*, 2009].

2.1.2 Transport and Deposition of Aerosols

In order to understand the accumulation of SSAs at a final location - which, for the purpose of this work will be Dome C, one needs to dive into the respective processes of aerosol transportation and deposition. From their areas of formation, the aerosols are lifted by either turbulent eddies or large-scale convection. Nonetheless, if the wind is not strong enough, not all aerosols have a long life span, as some simply drop back into the ocean or onto the ice [*Lewis and Schwartz*, 2004]. As can be inferred from Figure 2.5, which shows the prevalence of SSAs depending on latitude and height, the sea salt concentration in the air is comparably high up to a height of about 2 km (at ca. 0.5 to 1 μgm^{-3}). With increasing altitude, the concentration quickly decreases to below 0.01 μgm^{-3}. This implies that vertical transport regularly occurs to about 2 km height, and SSAs can be taken up by air parcels up to that altitude. The rest of their transport to the deposition location must take place without any precipitation, since, otherwise, the aerosols will be washed out and deposited beforehand. Within the scope of this work, the pathway that the air parcels take and which leads them to Dome C is calculated by the FLEXTRA trajectory method.

In general, SSAs settle on the surface by either wet or dry deposition. The former describes

Figure 2.4: Frost flowers in the Arctic, on young ice. Source: *Wikipedia contributors* [2022b].

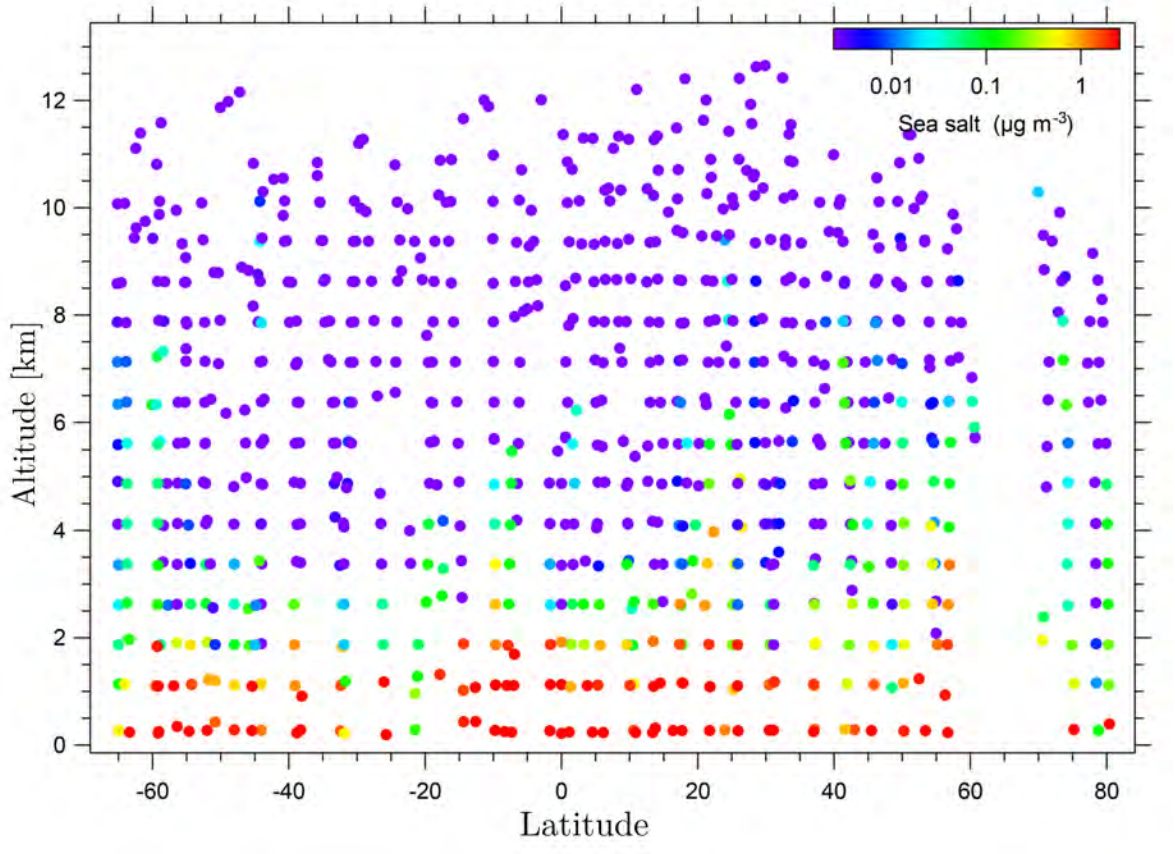

Figure 2.5: Mean over all longitudes of sea salt concentration in the air above oceans, varying with height and latitude. Source: *Murphy et al.* [2019].

the process of washing aerosol particles out of the air by precipitation. This is called scavenging, and happens mostly in rain or snow, where sub-cloud aerosols are collected by falling precipitation and subsequently washed out [*Cherrier et al.*, 2017; *Zíková and Ždímal*, 2016]. Moreover, since aerosols provide a surface for water vapor to condense on, and consequently form water droplets, they also serve as cloud condensation nuclei. When the droplets fall, so do the aerosols in the droplets, leading to their deposition. The overall deposition flux J_{wet} over Dome C linearly depends on the snow rate, since the prevailing precipitation in the Antarctic Plateau is snow, with

$$J_{wet} = \epsilon A C_{air}, \tag{2.2}$$

where A is the precipitation accumulation rate, ϵ is the effective snow scavenging ratio, which describes the efficiency of snow capturing aerosols, at 2,000±800 g_{air} g_{snow}^{-1} for sea salt [*Yang et al.*, 2015; *Schüpbach et al.*, 2018], and C_{air} is the concentration of the aerosol in the air. Dry deposition J_{dry}, on the other hand occurs by turbulent mixing, Brownian diffusion, impaction, and gravitational settling of particles, strongly dependent on particle size and wind speed [*Barber et al.*, 2004]. It depends on the dry deposition velocity v_{dry}:

$$J_{dry} = v_{dry} C_{air}. \tag{2.3}$$

For particles larger than 1 µm, which is the main size bin for sea salt aerosols in the Southern Ocean, gravitational settling is the main dry deposition process [*Carslaw*, 2022]. In the case of SSAs, its velocity $v_{settling}$ dictates the total dry deposition velocity with

$$v_{settling} = \frac{2}{9}(\rho - \rho_{air}) g \frac{r^2}{\eta}, \tag{2.4}$$

where r describes the radius and ρ and ρ_{air} the density of the aerosols and the air, respectively. The gravitational acceleration is described by g, and η is the dynamic viscosity of the medium, in this case, air. According to *Emerson et al.* [2020], the minimum v_{dry} is 0.1 cm s^{-1} for radii of 0.25 µm, and it increases to 1 to 2 cm s^{-1} for particles of 1 to 2 µm radius, the main particle size for Southern Ocean sea salt aerosols. The final concentration of sea salt in the ice C_{ice} is then given by

$$C_{ice} = \frac{v_{dry} + \epsilon A}{A} C_{air}. \tag{2.5}$$

2.2 Meteorology of Antarctica

A sound understanding of the meteorology of Antarctica is essential for interpreting trajectories, justifying the parameters and thresholds used for the filtering of trajectories, and explaining what leads to changes in SSA source regions. To this end, Figure 2.6 gives a general overview of Antarctica and its defining features. Usually, one divides Antarctica into i) East Antarctica, comprising the biggest part, and where Dome C is located (marked in red), ii) West Antarctica, separated from East Antarctica by the Transantarctic Mountains, and iii) the Antarctic Peninsula. East Antarctica has an elevation of about 4 km at its highest

point and a very steep coast. Surface winds that fall off this coast gain immense velocities of up to 300 km h^{-1} [*Stohl and Sodemann*, 2010; *Trewby*, 2002]. These surface winds are called katabatic winds, and are further strengthened by the high-pressure system over the Antarctic continent, and the circumpolar trough, a low-pressure belt around Antarctica. Moreover, this circumpolar trough enables the formation of cyclones over the oceans surrounding the Antarctic, leading to a strong upward transport. Note that these cyclones play an important role in bringing moisture to the continent, and as such are responsible for much of the sea salt concentrations in Antarctica [*Fischer et al.*, 2007].

Besides being the windiest, Antarctica is also the coldest and driest continent on Earth [*Riffenburgh*, 2014]. While the mean annual temperature of the interior is about -57 °C, with annual precipitation as low as 2 to 3 cm, this was even more extreme during the LGM. LGM temperatures are estimated to be around 9 °C colder in Antarctica than today (cf. Figure 2.7), compared to a global temperature change of -6 °C [*Jouzel et al.*, 2003], while precipitation was only approximately 50% of precipitation today [*Werner et al.*, 2001].

The most important Empirical Orthogonal Function of the Southern Ocean and Antarctic pressure is the Southern Annular Mode (SAM), which correlates to the Southern polar jet's strength and position [*Fogt and Marshall*, 2020]. The SAM is defined as the difference in normalized sea level pressure SLP at 40°S and 65°S [*Silvestri et al.*, 2022]. The phases of SAM change on decadal to millennial timescales [*Reynhout et al.*, 2019], with a positive SAM index indicating a high-pressure system in the mid-latitudes and a low-pressure system in the high-latitudes, while the opposite holds true for the negative SAM phase. On a centennial timescale, we are now in a positive SAM phase, which has become stronger since the beginning of the industrial period [*Silvestri et al.*, 2022; *Reynhout et al.*, 2019; *Kaplan et al.*, 2020], generally attributed to anthropogenic climate change. This positive phase leads to stronger westerly winds that shift poleward towards Antarctica and are responsible for higher temperatures above the Antarctic interior and lower precipitation [*Fogt and Marshall*, 2020]. During the LGM, *Kim et al.* [2014] argued that the SAM index was weaker than now, resulting in a colder and wetter climate over the Antarctic continent, with weaker and northward-shifted westerlies, which are visible in Figure 2.8. This result is in agreement with the assumption by

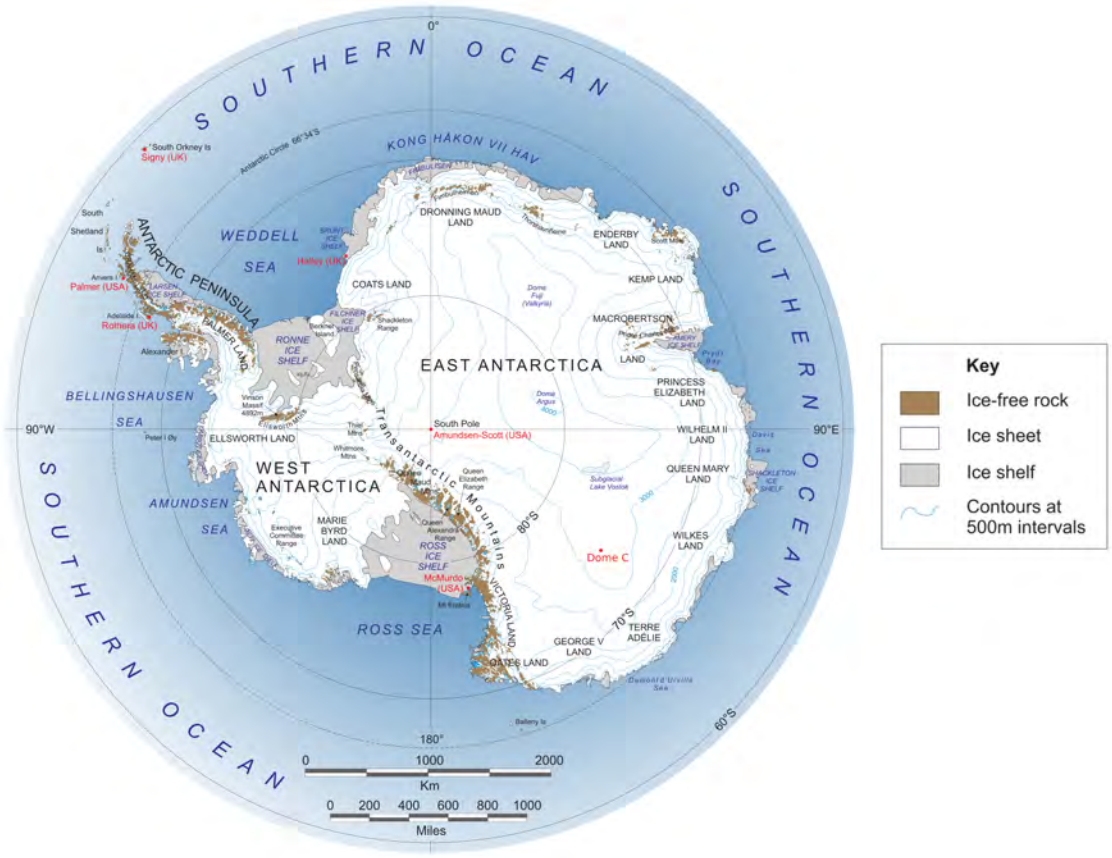

Figure 2.6: The Antarctic continent and its most prominent features. Dome C is marked in red in the lower part of East Antarctica. Source: *British Antarctic Survey* [2015].

Silvestri et al. [2022] that changes in insolation significantly influence changes in the SAM index, by leading to higher meridional temperature gradients, and thereby meridional pressure gradients. Earth's different orbital parameters during the LGM change the distribution of solar radiance, leading to the aforementioned changes in insolation [*Cao et al.*, 2019]. Insolation during the LGM was about 40 to 50 W m^{-2} lower than today. On top of that, radiative forcing, which affects the quantity of radiation that is absorbed by the Earth, has changed significantly over time. The total radiative forcing, consisting of greenhouse gases, land and sea ice albedo feedback, and aerosol feedback, has increased from -8 W m^{-2} to approximately 2.3 W m^{-2} between the LGM and 2013 [*Jansen et al.*, 2007; *Myhre et al.*, 2013]. *Wu et al.* [2022] stated that insolation in the Southern Hemisphere, along with CO_2 concentrations, is

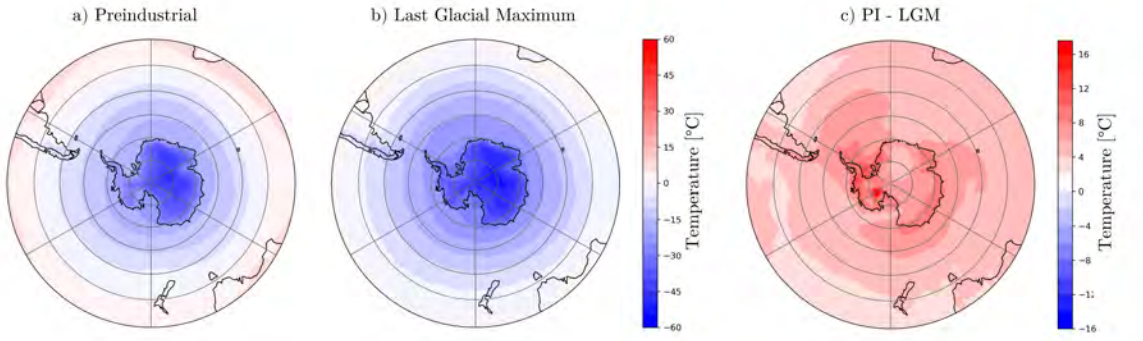

Figure 2.7: Mean annual surface temperatures in the Antarctic during a) the preindustrial, b) the Last Glacial Maximum, and c) the difference in temperature between PI and LGM, from the CESM1.2 simulation described in Section 3.1.2.

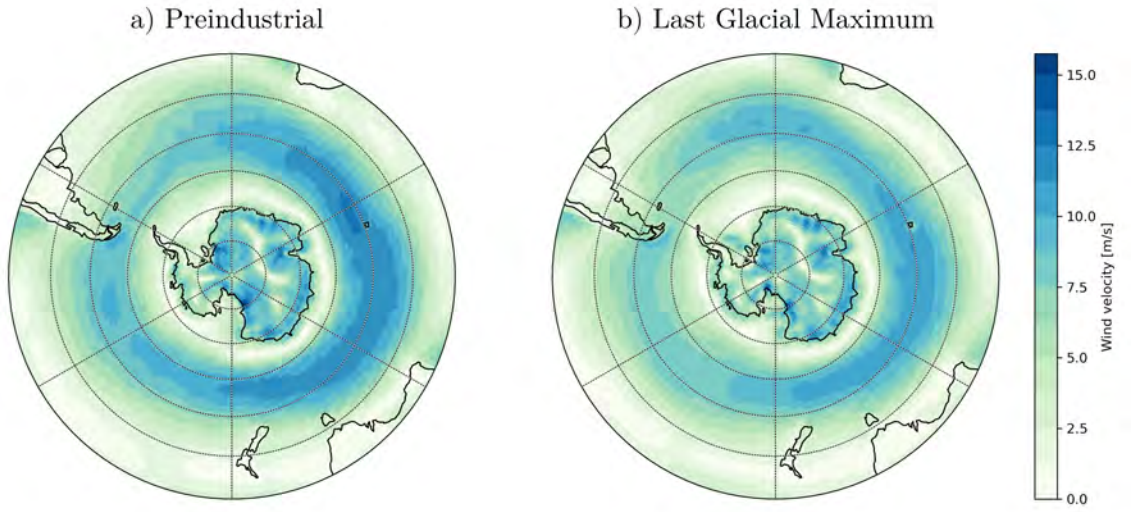

Figure 2.8: Mean annual wind velocities at CESM1.2 lowest model level in the Antarctic and Southern Ocean during a) the preindustrial and b) the Last Glacial Maximum.

also one of the most important parameters affecting sea ice cover because of their influences on temperature. Sea ice, on the other hand, has positive feedback on temperature via its albedo, which reduces Earth's absorption of solar radiation, leading to a cooler climate.

Another important climatic difference between the LGM and the PD that applies not only to Antarctica, but the whole world, is a shift in seasons, also caused by orbital changes. The insolation pattern during the LGM was shifted forward in the year by approximately four weeks, so that the winter months are May, June, and July, rather than just June, July, and August, as under current climatic conditions [*Buzan et al.*, 2023].

Chapter 3

Data and Methods

This chapter presents the datasets and methods which, build the foundation of the study. Section 3.1 introduces the reanalysis ERA5 and the Community Earth System Model Version 1.2 with their resolutions, which time periods they cover in this study, and how the data was collected or calculated. Section 3.2 then explains the FLEXTRA trajectory tool and its principle, how the data was adapted to make it fit for use, and how it was filtered.

3.1 Datasets

The model used for the comparison of PI and LGM is the Community Earth System Model Version 1.2. To validate the model's accuracy in the Antarctic region and the data's suitability for back-trajectory calculation, we will first analyze the difference between CESM1.2 and ERA5, a reanalysis dataset, which represents the best estimate of the reality.
In the following, we will describe the setups and features of ERA5 and CESM1.2.

3.1.1 Reanalysis ERA5

ERA5 is an atmospheric reanalysis dataset that is provided by the European Centre for Medium-Range Weather Forecasts (ECMWF), covering the entire globe in an hourly resolution from 1950 until today [*Hersbach et al.*, 2020]. Reanalyses are a combination of observations and models, which provide a complete and global dataset. Because of the regular input of observations, reanalyses are by definition physically consistent and plausible models

Dataset	Period	Year	Temporal Resolution	Spatial Resolution
ERA5	PD	1990-1999 CE	hourly & 6-hourly data	1°×1° & 0.25°×0.25°
CESM1.2	PI	1850 CE	6-hourly data	1°×1°
CESM1.2	LGM	19050 BCE	6-hourly data	1°×1°

Table 3.1: Datasets and resolutions used for Common Era (CE) and Before Common Era (BCE).

[*Cucchi et al.*, 2020]. The combination of observations and model is achieved by the four-dimensional variational data assimilation technique 4D-Var, based on an observation window of 12 hours. In this window, a short-term forecast is compared with the observational data (cf. Fig. 3.1). The best dynamical and statistical combination of the two is found by reducing the error, determined by a complex function that takes into account the credibility of the forecast and potential measurement errors of the observations and their evolution over time. The interested reader is advised to consult *Bannister* [2007] for further information on error calculation. From this corrected forecast, the model computes forecasting data for the next 12 hours, which then in turn serve as the starting point for the next time window [*Hersbach et al.*, 2020]. For each time step, the forecast accounts for the interaction of atmosphere, land, ocean waves, sea surface temperature, and sea ice components.

In addition to the observations, information about radiative forcing such as solar irradiance and greenhouse gases are added as boundary conditions [*Cucchi et al.*, 2020]. Furthermore, boundary conditions on sea surface level are included in ERA5. The Met Office Hadley Centre and EUMETSAT provide daily sea surface temperature and sea ice concentrations, which are the reanalysis products HadISST2.1.1.0 and OSI SAF (409a), respectively [*Hersbach et al.*, 2020].

The atmospheric data are provided on a horizontal grid of 0.25° and on 137 vertical levels, to a height of up to 1 Pa. The levels are hybrid sigma/pressure levels (cf. Figure 3.2), where the levels follow the terrain (sigma) in the lower levels and even out toward the top of the atmosphere where they follow the pressure levels [*Collins et al.*, 2004].

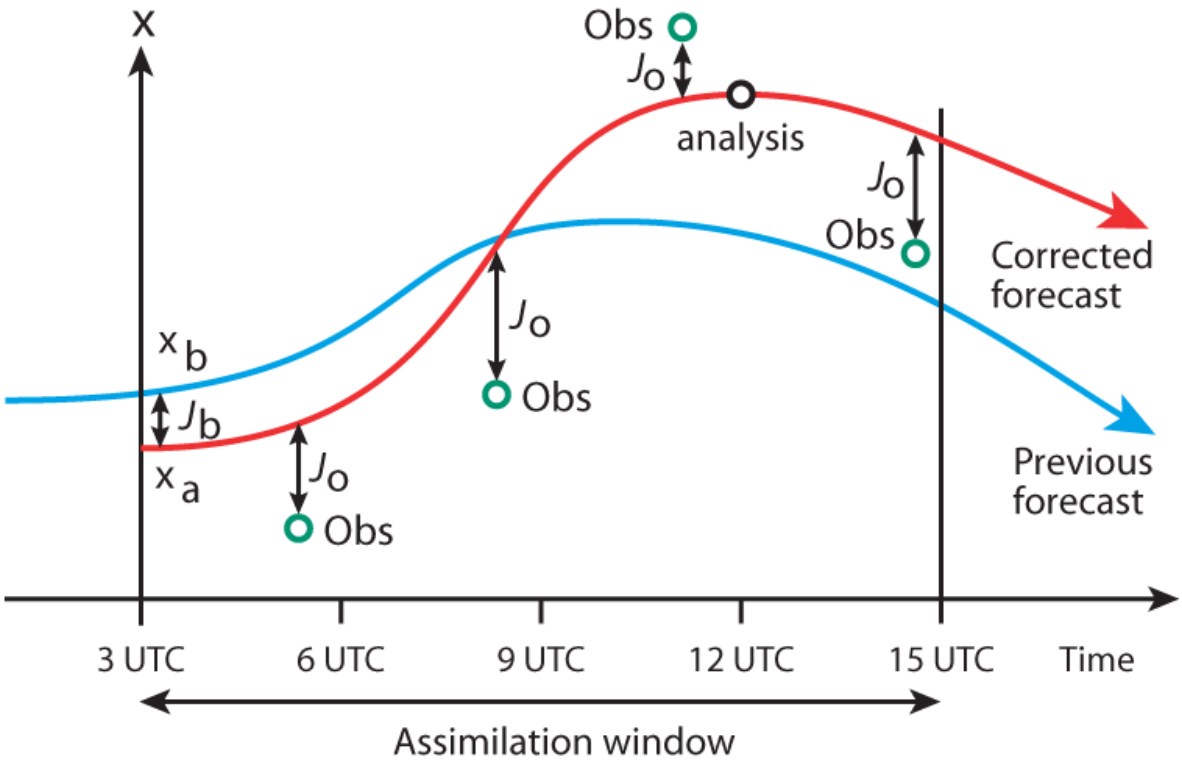

Figure 3.1: Assimilation of analysis data *Obs* (green) and short-term forecast x_b (blue) during a 12-hour-period. The settlement of the two is x_a (red), which is statistically and dynamically optimal, by minimizing the error functions J_b and J_o. Source: *ECMWF* [2017].

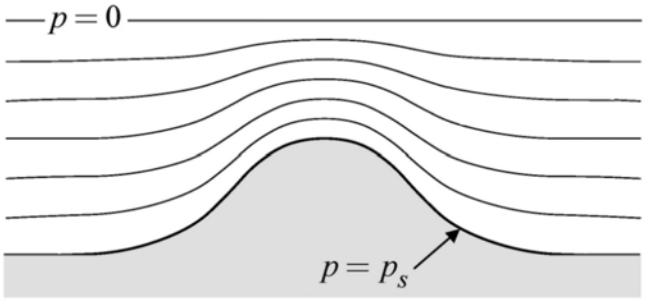

Figure 3.2: Hybrid sigma/pressure levels. The lowest level adheres to the terrain, and thus the surface pressure, and the levels flatten out so that the highest levels are in accordance with the pressure lines. Source: *Chow et al.* [2019].

Despite the spatially and temporally high resolution, however, ERA5 has some biases over Antarctica. For example, *Jiangping et al.* [2021] found a cold bias (maximal value of -1.2 °C) throughout the austral summer months and a warm bias of up to 0.4 °C due to overestimation of sensible heat fluxes in the winter. These biases may have an influence on the calculation of back-trajectories. ERA5 also overestimates precipitation over the Antarctic continent, especially on the Antarctic plateau [*Roussel et al.*, 2020]. *Wang et al.* [2020] showed a general underestimation of cloud cover by ERA5, with a mean of 0.70 compared to 0.75 in observations. Figure 3.3 shows that this underestimation is evident for cloud cover situations above 0.3, while ERA5 overestimates cloud cover for situations with fewer clouds. *Caton Harrison et al.* [2022] considered ERA5 the best of three analyzed reanalyses with an overall low negative wind bias.

ERA5 provides the data for the back-trajectory analyses from 1990 to 2000 for the southern latitudes, i.e., 30°S to 90°S, in an hourly resolution. The impact of the spatial resolution on aerosol backtracing is investigated through the differences in datasets of 0.25°×0.25° and 1°×1° resolution (ca. 30 km and 111 km at the equator, respectively). While the fine resolution is ERA5's standard output, the coarser resolution is achieved by interpolation of the data. The interpolation for continuous parameters is a bilinear interpolation, while nearest-neighbor interpolation is used for discrete fields such as vegetation [*Maciel et al.*, 2017].

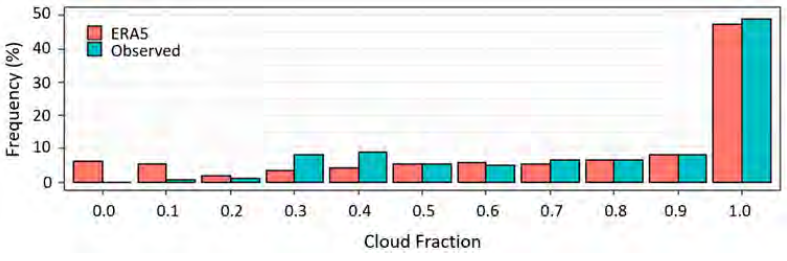

Figure 3.3: Prevalence of cloud covers in ERA5 (red) compared to observations (blue). Source: *Wang et al.* [2020].

3.1.2 The Community Earth System Model Version 1.2

The Community Earth System Model Version 1.2 (CESM1.2) is provided by the National Center for Atmospheric Research (NCAR) and other research institutes as a collaborative model [*Hurrell et al.*, 2013]. Released in 2010, it is a fully coupled general circulation model with four components: atmosphere, ocean, land, and sea-ice, that interact with each other via a coupler (cf. Figure 3.4). It simulates Earth's climate for the past, present, and future and includes a variety of physical parametrizations such as land use changes due to anthropogenic activities, and chemical and physical processes that affect aerosol development.

CESM1.2 uses the Community Atmospheric Model 5 (CAM5) as an atmospheric component. While the final horizontal resolution is evenly distributed in approximately 1° (1.25° in longitude and 0.9° in latitude), the vertical direction is divided into 30 unevenly distributed levels with the top being at a pressure of ca. 5.1×10^{-4} Pa [*Neale et al.*, 2010]. As in ERA5, the level distribution is a hybrid sigma/pressure structure (cf. Section 3.1.1). It uses a finite-volume dynamical core [*Neale et al.*, 2010], where the horizontal discretization is based on a multidimensional, mass-conserving, and semi-Lagrangian scheme [*Lin and Rood*, 1997], and a vertical quasi-Lagrangian discretisation [*Collins et al.*, 2004]. Inside this core, each physical process implemented in the atmospheric model is described individually. The dynamical core

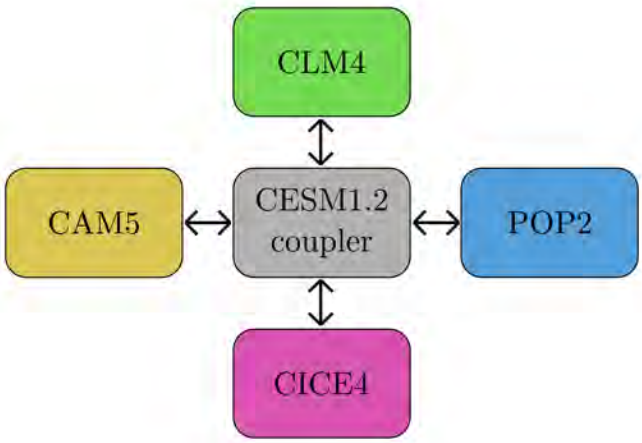

Figure 3.4: Coupler and components of CESM1.2. Modified from *Buzan et al.* [2023].

D and physical parametrisation P are coupled by

$$\frac{\partial \phi}{\partial t} = D(\phi) + P(\phi) \ , \tag{3.1}$$

where ϕ is any time-dependent variable, such as wind-speed or temperature [*Neale et al.*, 2010].

The land model, called the Community Land Model 4 (CLM4), has the same horizontal grid as the atmospheric model and is divided into 15 vertical levels [*Oleson et al.*, 2010]. Each grid cell in the model is attributed to land units (urban, lake, vegetated, wetland, glacier), which are composed of snow and soil columns (up to 5 and 15 levels, respectively), and up to 16 plant functional types [*Oleson et al.*, 2010].

Both the ocean and sea-ice simulations use freezing points that depend on salinity and have the same horizontal grid of approximately 1°×1°. The ocean model is the general ocean circulation model Parallel Ocean Program Version 2 (POP2), where, as for the atmospheric model, additional parametrization have been updated since the last version [*Smith and Gent*, 2010]. While the resolution in the zonal direction is constantly at 1.125°, the meridional resolution changes from approximately 0.27° at the equator to 0.53° at 32 °S and stays this way until the South Pole (cf. Table 3.2). POP2 is vertically resolved by 60 levels [*Hurrell et al.*, 2013].

The sea-ice model is based on the CICE Version 4 [*Hunke and Lipscomb*, 2010], which has eight vertical layers of sea ice, which are relevant for accurately calculating temperature and salinity distribution [*Danabasoglu et al.*, 2020]. CICE outputs the sea ice cover with the help of a thermodynamic model. This model calculates snow and ice growth under consideration of snowfall and vertical and radiative fluxes. Additional ice dynamics and transport models account for ice velocities and movements.

The simulations were initialized by bringing the fully-coupled model to quasi-steady state on a resolution of 2°×2° [*Buzan et al.*, 2023]. As soon as the absolute radiation imbalance is < 0.32 Wm^{-2}, which is considered quasi-steady state, time-varying variables from the ocean and sea ice models are taken from the last years of the fully-coupled model as boundary conditions. Then, the atmospheric and land models CAM5 and CLM4 are run with these boundary conditions on a 1°×1° horizontal grid. This data on a finer resolution is used for

Latitude	Zonal resolution			
	ocean		atmosphere	
	in °	in km	in °	in km
Equator	0.27	30	1.25	138.8
-15°	0.39	41.8	1.25	134
-30°	0.51	49.4	1.25	120.2
-45°	0.53	41.6	1.25	98.1
-60°	0.53	29.4	1.25	69.4
-75°	0.53	15.2	1.25	35.9
-85°	0.53	5.1	1.25	12.1

Table 3.2: Zonal resolution of the model components in the CESM1.2.

the back trajectories and analysis.

The CESM1.2 model was brought into a quasi-steady state for two simulations: one control simulation at Preindustrial times for intermodel comparison of ERA5 and CESM1.2, and one for the LGM at around 21,000 years BP. The PI control is a scientifically supported simulation provided by the NCAR [*Buzan et al.*, 2023]. For the LGM simulation, the orbital parameters are adjusted according to Table 3.3 [*Buzan et al.*, 2023], while we implemented greenhouse gas concentrations and land use changes from the Paleoclimate Modelling Intercomparison Project version 4 [*Kageyama et al.*, 2017]. Boundary conditions for ice sheet extent, ice sheet heights, and sea level come from the ICE-6G_C model [*Peltier et al.*, 2014]. As the volume of the Antarctic ice sheet is assumed to have changed only marginally since the LGM, changes in ice sheet extent and height conditions have been applied only to the Northern Hemisphere. Boundary conditions of Antarctica, therefore, are the same for both PI and LGM scenarios.

While comparing CESM1 to ERA-Interim, *Park et al.* [2013] found a general overestimation of sea-ice around and snow cover on Antarctica in CESM1.2, which leads to an albedo-induced cold bias over the continent.CESM1.2 also strongly underestimates wind velocities in the Southern Ocean, as depicted in Figure 3.5. The wind speeds on the Antarctic continent,

Period	Year	Obliquity	Eccentricity	Precession
PI	1850 CE	23.453°	0.016764	280.327°
LGM	19050 BCE	22.9490°	0.018994	294.425°

Table 3.3: Orbital parameters in the CESM1.2 for the Common Era (CE) and Before Common Era (BCE). Source: *Buzan et al.* [2023].

however, are well represented in the model.

3.2 Methods

This section describes the different tools that are used for the calculation of trajectories, their subsequent filtering, and the necessary preprocessing for these steps. Section 3.2.1 gives an overview of the particle trajectory tool FLEXTRA. The steps that need to be taken for preparing the data for the FLEXTRA trajectory tool are described in Section 3.2.2. Section 3.2.3 lists the different parameters used for filtering the trajectories, how they are calculated, and the exact values applied as thresholds.

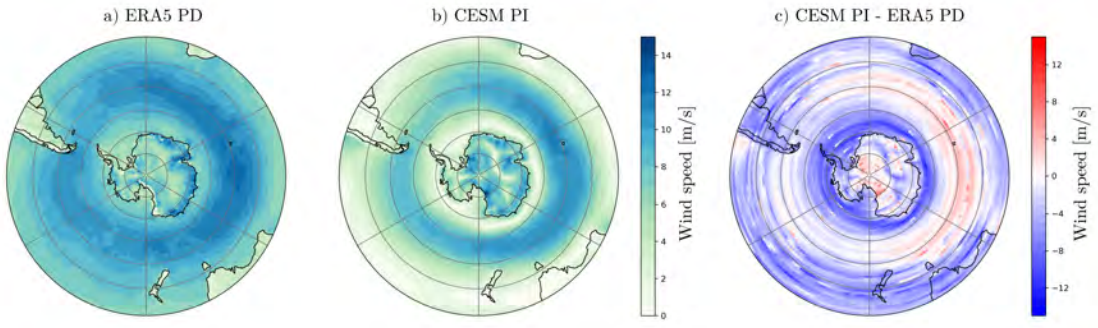

Figure 3.5: Annual mean wind velocity of a) ERA5, b) CESM1.2, and c) the CESM1.2 bias compared to ERA5.

3.2.1 FLEXTRA - Trajectory calculation

In this study, we use FLEXTRA to calculate the backward trajectories of SSAs deposited in Antarctica. FLEXTRA is a trajectory method written in FORTRAN 77 code, which is used to calculate three-dimensional backward trajectories including their uncertainties. FLEXTRA calculates the backward movement of an air parcel from a defined end location and time. While within FLEXTRA, temperature T, horizontal wind velocity u (in zonal direction) and v (in meridional direction), vertical velocity w are input as three-dimensional vector fields, surface pressure and topography are based on a two-dimensional representation (cf. Table 3.4). Those fields require the same spatial and temporal resolution, and the three-dimensional fields must also have the same number of levels [*Stohl*, 2000]. Under the hood, FLEXTRA

Name	Short Name	Number	SL/ML	Units
Mean Sea level pressure	*msl*	151	SL	Pa
Standard deviation of orography	*sdor*	160	SL	m
Temperature	T	130	ML	K
U component of wind	u	131	ML	m
V component of wind	v	132	ML	m^{-1}
Eta-coordinate vertical velocity	$\dot{\eta}$	077	ML	s^{-1}

Table 3.4: Required parameters for FLEXTRA use, on Single Level (SL, three-dimensional), or Multi Level (ML, four-dimensional).

uses the *Petterssen* [1941] differential equation to calculate the trajectories:

$$\frac{d\mathbf{X}}{dt} = \dot{\mathbf{X}}[\mathbf{X}(t)] \ , \tag{3.2}$$

where t denotes the time, $\mathbf{X}$ the position vector, and $\dot{\mathbf{X}}$ the wind velocity vector. Thus, the change of the trajectory's position per time step equals the wind velocity and direction at that position. Neither the trajectory's position $\mathbf{X}$ nor its change with time $\frac{d\mathbf{X}}{dt}$ are known but can be ascertained via Taylor expansion. The second order Taylor expansion of Equation 3.2 results in the following constant acceleration scheme, which is solved iteratively:

$$\mathbf{X}(t_1) \approx \mathbf{X}(t_0) + \frac{1}{2}\Delta t[\dot{\mathbf{X}}(t_0) + \dot{\mathbf{X}}(t_1)] \quad \text{initialized with} \quad \mathbf{X}^1(t_1) = \mathbf{X}(t_0) + \Delta t\dot{\mathbf{X}}(t_0) \ , \quad (3.3)$$

where $\Delta t = t_1 - t_0$ is the time step, and both $\mathbf{X}$ and $\dot{\mathbf{X}}$ are taken at t_0 and t_1. In the initializing equation, the wind velocity of the new position is not taken into account, but the first approximation $\mathbf{X}^1(t_1)$ depends only on the wind speed at the starting point. The wind velocity of the first estimate is then inserted as $\dot{\mathbf{X}}(t_1)$ into the next iteration. Thus, the new position of the air parcel will be approximately as far away from the starting point as the mean velocity of the two points times the time step. It usually takes about three iterations to reach convergence, which is typically defined by an absolute tolerance of 0.0001 grid points difference between two iterations [*Stohl*, 2000]. In practice, this works as exemplified in Figure 3.6, where the back-trajectory (purple) is calculated from the red endpoint, at a specific height. The length and direction of each purple arrow depend on the strength and direction of the wind velocities of both the point it starts from and its end position.

A FLEXTRA run is structured as in Figure 3.7: after setting the endpoint of the back-trajectory (in our case Dome C) and its height (here 50 m, 500 m, and 1500 m) and inputting the wind fields to FLEXTRA, the aforementioned iteration step, followed by uncertainty and output data calculation, is repeated for 240 hours, i.e., 10 days, or until the trajectory leaves the studied area and reaches 30°S. For each time step, FLEXTRA outputs position, date and time, pressure, potential temperature, and potential vorticity. Since most trajectory points do not land exactly on the grid points, the gridded data needs to be interpolated before the output. The interpolation used by FLEXTRA for the horizontal, vertical, and temporal dimensions is bicubic, polynomial, and linear, respectively. *Stohl et al.* [1995] has termed this combination the most accurate interpolation method. Potential vorticity can be used to estimate uncertainty since it is conserved under adiabatic conditions. Thus, it can be used to roughly determine the uncertainty of upper-level trajectories, where the conservation of potential vorticity is better fulfilled than for lower levels, due to mixing processes or diabatic effects.

In the lower levels, potential vorticity cannot be used as an estimate for trajectory uncertainty. There, uncertainty can be gauged by the so-called ensemble method. It adds both small

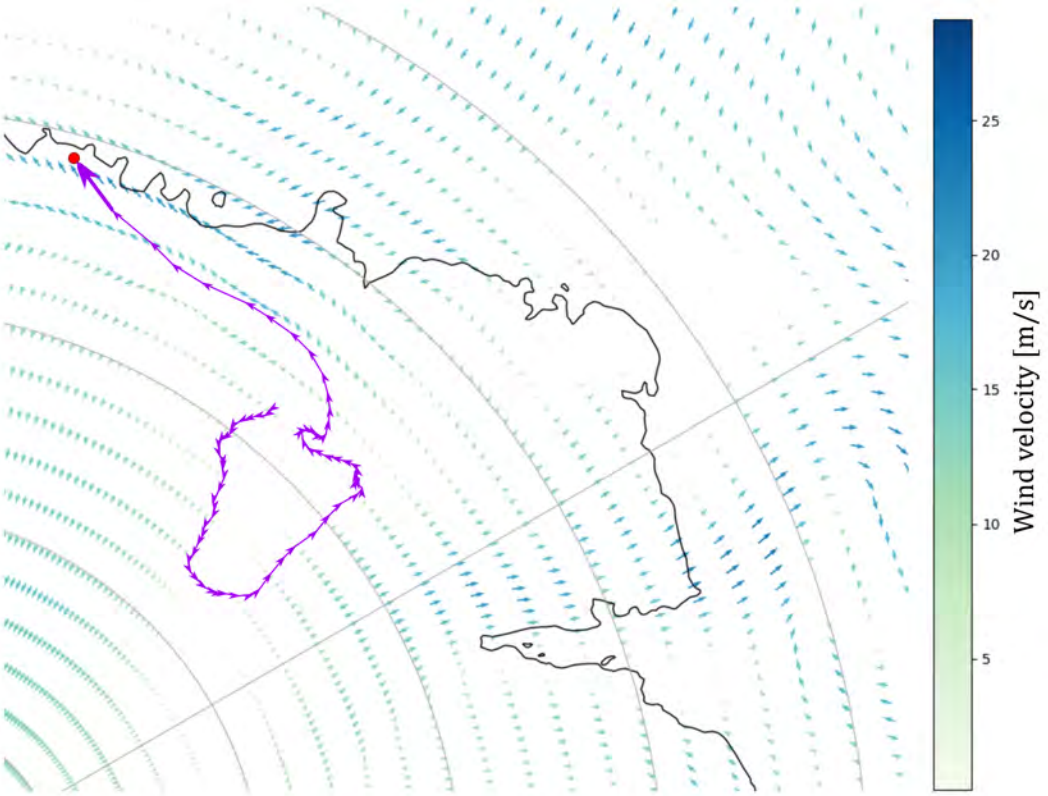

Figure 3.6: Example of back-trajectory calculation via FLEXTRA on an exemplary wind velocity field of the first time step (bold arrow), where the red dot is the designated end and each purple arrow signifies one calculated backward time step, based on the respective wind fields. The background arrows are scaled to wind velocity.

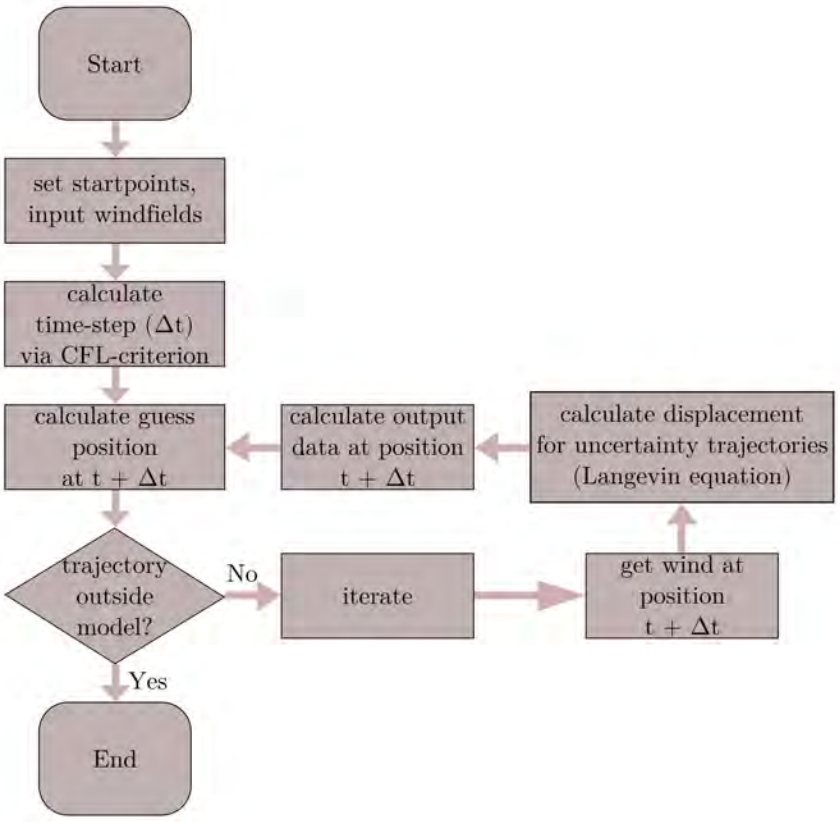

Figure 3.7: Flowchart of the trajectory calculation of the FLEXTRA program.

position errors and random errors whose amplification is calculated according to a stochastic differential equation (Langevin equation) for the duration of the trajectory. This gives an estimate for uncertainties along the trajectory [*Stohl*, 2000].

3.2.2 Pre-Processing

Since by design, FLEXTRA requires input data from ECMWF, data from ERA5 only has to be pre-processed by the tool Flex-Extract, which, as the name suggests, extracts smaller files of the original dataset. The files are split temporally so that a file contains only the parameters necessary for FLEXTRA in the required spatial resolution and field for one time step. However, while the pre-processing of ERA5 is rather straightforward, this is not the case when dealing with CESM data. The extraction of data split by time steps is similar to ERA5, whereas the calculation of the vertical velocity using CESM1.2 data is more complex. Unlike

FLEXTRA which uses the hybrid η based coordinate system, as in Figure 3.2, with inherent vertical velocity $\dot{\eta}$ [s^{-1}], CESM, as a pressure-based model, outputs the vertical velocity only in pressure-based coordinates (ω) in Pa s^{-1}. Therefore, $\dot{\eta}$ has to be calculated beforehand, using the divergence and surface pressure of each grid point. As described by *Bluestein* [1992], the calculation of the divergence dv works as follows:

$$dv = \frac{\partial v}{\partial y} + \frac{\partial u}{\partial x} - \frac{v}{a}\tan(\phi) \ . \tag{3.4}$$

Here, u and v are the wind velocities in longitudinal (x) and latitudinal (y) direction, respectively, a the radius of the Earth, and ϕ the latitude. The surface pressure PS is used to compute the pressure P_k on each level k, with the hybrid vertical coefficients A_k and B_k, which are inherent to the model:

$$P_k = A_k + B_k * PS \ . \tag{3.5}$$

The final calculation of $\dot{\eta}$ also takes into account the horizontal wind velocities u and v, and the x and y components of $\log(PS)$, $\frac{\partial PS}{\partial L}$ and $\frac{\partial PS}{\partial M}$, respectively:

$$\dot{\eta} = -dv * (P_{k+1} - p_k) - (B_{k+1} - B_k)PS * \frac{u\frac{\partial PS}{\partial L} + v\frac{\partial PS}{\partial M}}{\cos PAR} \ , \tag{3.6}$$

where PAR is the field of Gaussian parallels, ranging from 0 at the equator to 1 at the poles. When the $\dot{\eta}$ computation is done, the back-trajectory calculation can be run for CESM, too.

3.2.3 Thresholds and data preparation

The data output of FLEXTRA used in our analysis is latitude, longitude, time and date, pressure, height above sea level and height above orography, and potential vorticity. The particular processes of formation, transport, and deposition of sea salt aerosols discussed in Section 2.1 need specific conditions. Therefore, we use parameters such as 10 meter wind velocity, precipitation, and sea ice cover and apply the respective thresholds to the trajectories. While these parameters can be downloaded directly from ECMWF for the PD, they have to be post-processed for the CESM output. The thresholds themselves originate from careful deliberation of the current understanding of the processes, sensitivities, and reliability of the data due to its resolution. For each parameter, the calculation (if necessary), the sensitivity,

and the consequent threshold are explained in the following. The calculated values of precipitation rr, 10 meter horizontal wind $\vec{v}_{10}$, and sea ice cover ci are subsequently implemented into the FLEXTRA output files to fit the position of the trajectory at the given time and location.

Precipitation

Precipitation limits the transport possibilities by raining out sea salt aerosols on the trajectory path and enables wet deposition. When working with atmospheric models, usually a minimal precipitation rr of 0.3 mm day^{-1} is assumed to represent the actual existence of precipitation. This equals an hourly rr of 0.01 mm hour^{-1}. Since precipitation is used for two thresholds, they are listed separately: Precipitation as an indicator for wet deposition acts locally, in the Dome C grid cell. A sensitivity study was performed with rr necessary for wet deposition larger than 0.04, 0.02, and 0.01 mm hour^{-1} in Section 4.1. Secondly, precipitation is also the factor that leads to aerosols raining out of the air parcel. Consequently, a limit has to be set, over which we assume no aerosols were left in the air parcel to reach Dome C. The grid cell size of 1° encompasses quite a large area, and precipitation on Earth is not uniformally distributed over such a large area. To overcome this problem, a sum of precipitation over the last 24 hours of a trajectory was set as a limit, with the assumption that washing out is more likely to happen if precipitation occurs over 24 hours. This has been tried for rr below 0.5, 1, and 3 mm day^{-1}.

In both datasets, rr is the sum of convective precipitation cp and large-scale precipitation lsp. While the ERA5 output gives accumulated rr in hourly (m hour^{-1}) resolution, which we only converted to mm hour^{-1}, the CESM1.2 output accumulates rr over six hours, which was simply divided by six and then treated with the same precipitation threshold. For the ERA5 6-hourly control period, we accumulated rr over the last six hours and then treated the data just as for the CESM output.

10 meter horizontal wind

The 10 meter horizontal wind $\vec{v}_{10}$ serves as an indicator for the formation of aerosols and for the possibility of dry deposition. The threshold for wave formation, and thereby SSA formation, has been suggested by several authors (e.g., *O'Dowd and de Leeuw* [2007], *Glantz et al.* [2009], *Liu et al.* [2021]) to lie at 4 ms^{-1}. However, *Murphy et al.* [2019] showed that the background sea salt aerosol concentration is still relatively high up to an altitude of about 2 km, while *Bian et al.* [2019] showed a significant dip in SSA concentration only at about 4 km altitude, suggesting that air parcels can pick up aerosols from the constant background SSA concentration, even without strong winds generating SSAs at the water surface. Hence, we reduced the wind speed criteria to 3 ms^{-1}, and also filtered the trajectories without taking the formation wind speed into account. The wind speed for dry deposition is more straightforward, in that the air parcel has to remain at or over Dome C long enough for SSAs to be able to reach the surface by dry deposition during that time. This is most common for $\vec{v}_{10} \leq 5$ ms^{-1} at the deposition point [*Saral*, 2018]. Those are the two thresholds applied in our filtering method. Both in ERA5 and CESM1.2, the wind is given only in east- u and northward v direction, so the total horizontal wind $\|\vec{v}_h\|$ has to be calculated by

$$\|\vec{v}_h\| = \sqrt{u^2 + v^2} \ . \tag{3.7}$$

Note that ERA5 outputs $\vec{v}_{10}$, the wind velocity at 10 m above the Earth's surface. CESM1.2, however, does not have a level close enough to Earth's surface for $\vec{v}_{10}$. Instead, it gives the wind at the lowest model level, which lies between 40 to 70 m above the surface.

Height of trajectory

Since sea salt aerosols are formed at sea level, their concentration decreases with increasing height [*Murphy et al.*, 2019]. To be sure that the trajectory is at a height where sea salt aerosols are present, the maximum height above sea level at the formation point needs to be defined. A useful parameter is the boundary layer height, which was not available as output by CESM1.2. Because the boundary layer heights of PD vary from 600 to 1400 m in the Southern Ocean, thresholds of 1,000 and 1,500 m are applied. To analyze the sensitivity, we

also include height thresholds of 2,000 and 2,500 m.

Sea ice cover

Sea ice cover ci helps determine the process involved in SSA formation. Since both open ocean and sea ice formation are possible as soon as $0 < ci < 100\%$, we select boundaries in which one of the processes is more likely, in order to distinguish them. We assume that for $ci > 90\%$, no SSAs can be formed because so little water can imbue the ice with salt. The sea ice formation is set at $50\% < ci \leq 90\%$, while $ci \leq 30\%$ is interpreted as open ocean sea salt.

In both ERA5 and CESM1.2, ci is given as a fraction of the area that is covered by sea ice, between 0 and 1. Thus, no conversions were necessary to align the two datasets.

Chapter 4

Results

The main interest of this study are differences in sea salt aerosol source regions from the Last Glacial Maximum to the Preindustrial, which are presented in this chapter. Before we come to the analysis of source regions in the LGM and PI, we need to analyze parameters that influence the final results. As mentioned in Section 3.2.3, some of the filtering criteria are not unequivocally defined in the literature. Furthermore, the two datasets impact the calculated trajectories differently. Thus, the sensitivities of filtering criteria are studied in Section 4.1, and, based on these findings, one or more criteria will be determined for the rest of the study. In Section 4.2, the impact on trajectories of both temporal and spatial resolution is examined, as the two datasets differ there. Section 4.3 describes the differences between CESM1.2 and ERA5 that are given by factors other than their resolution. The heart of this study, the differences from the Last Glacial Maximum to Preindustrial are presented in Section 4.4, with the sea salt aerosols' source regions being analyzed in Section 4.4.1, and the large-scale circulation patterns leading to these differences in Section 4.4.2.

Before all these results are presented, a few expressions must be defined. The starting point of each trajectory is the time-wise starting point in an uninterrupted single-arc, that has the longest time to cover before it makes it to Dome C. Dome C, on the other hand, is the end point of each trajectory, as in our study, all trajectories were calculated from there. We also differentiate between whole trajectories, input points, and initial points, which are all visible in Figure 4.1, where Figure 4.1a shows the whole trajectories, with each point from the initial

point to Dome C. The input points (cf. Figure 4.1b), can be the starting point of a trajectory, or located anywhere along it, as long as they fulfill the input and formation criteria. Initial points (cf. Figure 4.1c) i.e., the starting point of each trajectory, are the first point of a trajectory where precipitation is not high enough to be filtered out by the transport criterion.

4.1 Testing of trajectory criteria

The thresholds for filtering the sea salt aerosols for the processes of formation, transport, and deposition, which could not be gathered from the literature were ascertained by sensitivity studies. For each process, several trajectory thresholds were applied as a filter criterion on 10 years of trajectories calculated from hourly ERA5 data with a 1°×1° resolution, and their influences on the number and pattern of left-over trajectories are compared in the following. In cases where the sensitivity of the criterion is very small, and only negligible impacts of the different thresholds on trajectories are discernible, the broadest threshold is selected. In the case of high sensitivities and thus large differences between different thresholds, we provide a reason for why a threshold was chosen. We will start with presenting the wet deposition

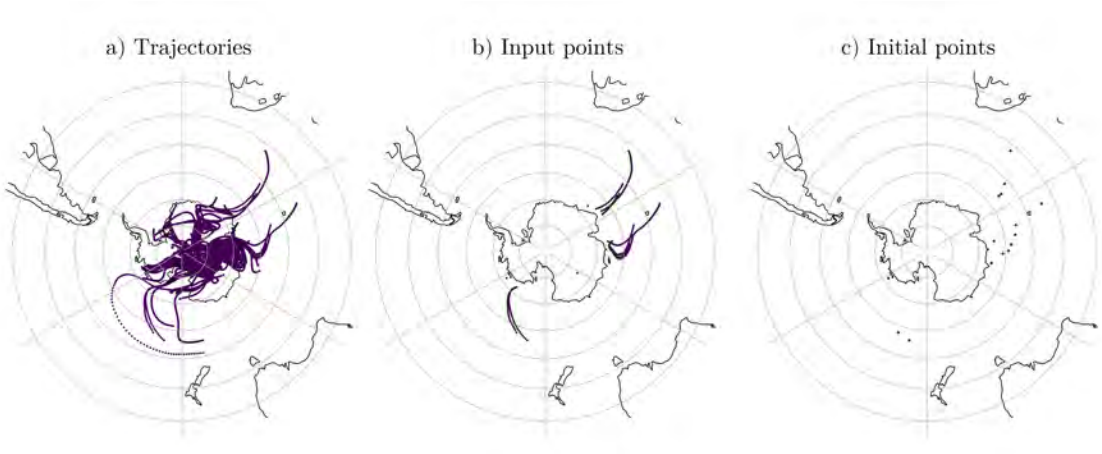

Figure 4.1: Example plots for whole trajectories (each point from start to Dome C, input points (points that fulfill the input criterion), and initial or starting points (only the first point of each filtered trajectory).

criterion and then go backward in time until the criterion for the formation of SSAs.

4.1.1 Wet deposition criterion

Models have a tendency to simulate very small amounts of precipitation, so a lower-bound value must be defined below which we will artificially set the precipitation to zero. Usually, a minimum of 0.3 mm day^{-1} is set as a lower boundary condition for model values to count as precipitation. This corresponds to hourly precipitation of roughly 0.01 mm hour^{-1}. The trajectories' sensitivity was tested with hourly precipitation rates of 0.02 and 0.04 mm hour^{-1}, for both wet and dry deposition. Figure 4.2 shows that the number of trajectories for dry deposition at Dome C changes very little with an increasing threshold ($\#_{traj}(0.01)$=126,733, $\#_{traj}(0.02)$=128,796, and $\#_{traj}(0.04)$=129,686), while trajectory numbers for wet deposition strongly decrease ($\#_{traj}(0.01)$=12,008, $\#_{traj}(0.02)$=5,979, $\#_{traj}(0.04)$=1,660). Hence, we will apply a threshold of 0.01 mm hour^{-1} in the following analysis since this is consistent with meteorological assumptions on models. Besides that, most trajectories are left over after filtering with a threshold of 0.01 mm hour^{-1}.

4.1.2 Transport criterion

This part of the filtering seeks to determine points in trajectories where the precipitation is so large that all SSAs which might be present in the air parcel would be washed out. The first step for this is to use the same precipitation thresholds (0.01, 0.02, 0.04 mm hour^{-1}) as in Section 4.1.1. However, for those three thresholds, almost none of the trajectories are left. This can be explained by the coarse data resolution of 1°×1°. Seeing as the grid cells are so large, the precipitation might not be taking place in the same region the air parcel is passing through. To account for the grid size, we used cumulative thresholds over a whole day instead of hourly thresholds. For each time step, the precipitation of the last 24 hours is accumulated, and this value is compared to thresholds of roughly 0.5, 1, and 3 mm day^{-1}. Figure 4.3 shows that significantly more trajectories survive the transport with a higher threshold both for dry and wet deposition. Given the fact that very few of the wet deposition trajectories are left after filtering them with thresholds of 0.5 ($\#_{traj}(0.5)$=3,530) and 1 mm day^{-1} ($\#_{traj}(1)$=7,018),

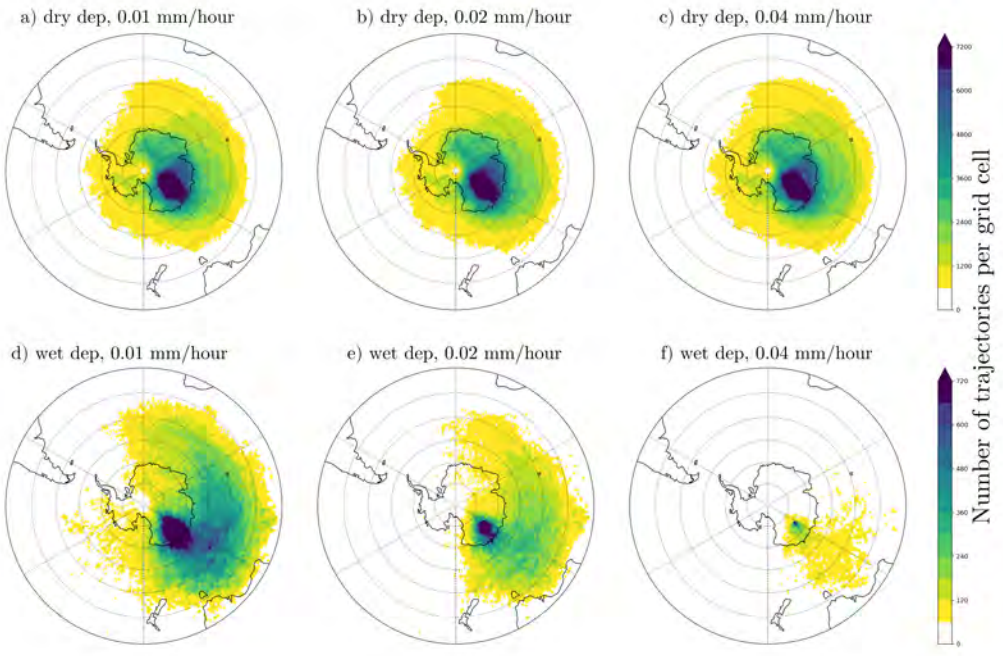

Figure 4.2: Dry (a to c) and wet deposition at Dome C (d to f) with precipitation criteria 0.01, 0.02, and 0.04 mm hour^{-1}. Shown in color is the number of trajectories per grid cell.

compared to 3 mm day ($\#_{traj}(3)$=12,605), we use the cumulative threshold of 3 mm day^{-1} for the transport criterion.

4.1.3 Input height criterion

Another factor to be considered is the input height which describes at which height it is still likely for SSAs to be present, so they may be taken up by an air parcel. This was debated to be equal to the boundary layer height [*Thomas et al.*, 2022]. However, the boundary layer height above the Southern Ocean with an altitude of about 600 to 1,000 m is very low. As earlier discussed in Section 2.1.2, *Murphy et al.* [2019] and *Bian et al.* [2019] showed that SSA concentration is still fairly high above 1,000 m, suggesting that SSA can be taken up at greater heights. To investigate the effect of the input height, we have compared heights of 1,000, 1,500, 2,000, and 2,500 m and their effects on the number of trajectories. The density plots of different input heights show increases in number of trajectories with

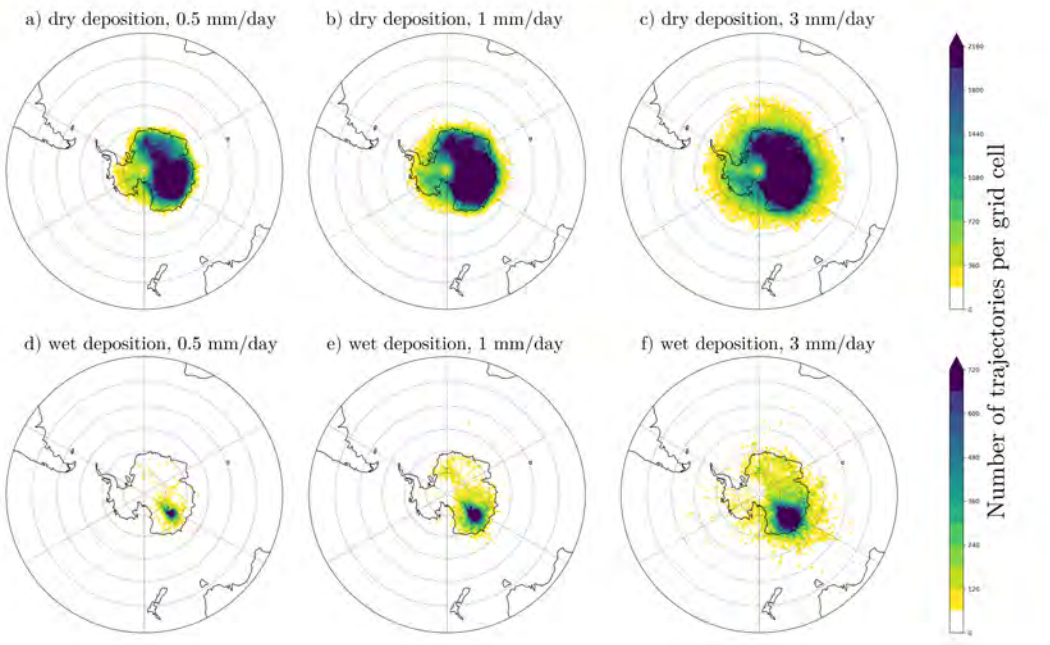

Figure 4.3: Wet (a to c) and dry (d to f) deposition trajectories over 15 years with precipitation criteria 0.5, 1, and 3 mm day^{-1}. Shown in color is the number of trajectories per grid cell.

increased height criterion (cf. Fig. 4.4), while the overall pattern remains the same for any input heights. Figure 4.5 shows the heights of the trajectories and highlights that the number of trajectories, while staying in the same range, increases from 1,000 to 2,500 m ($\#_{traj}(1,000)$ =63,760, $\#_{traj}(1,500)$ =78,524, $\#_{traj}(2,000)$ =88,473, $\#_{traj}(2,500)$ =99,706), but the overall height of trajectories increases from left to right, as the height criterion also increases. Given the concentrations discussed in 2.1.2 and found by *Bian et al.* [2019], it seems reasonable to use the 2,500 m threshold as input height criterion to ensure that no trajectories containing aerosols are missed.

4.1.4 Formation criterion

This criterion was initially introduced to parameterize the conditions necessary for the formation of sea salt aerosols - be that open ocean or sea ice aerosols. Many studies (e.g., *O'Dowd and de Leeuw* [2007], *Glantz et al.* [2009], *Liu et al.* [2021]) agreed on the threshold

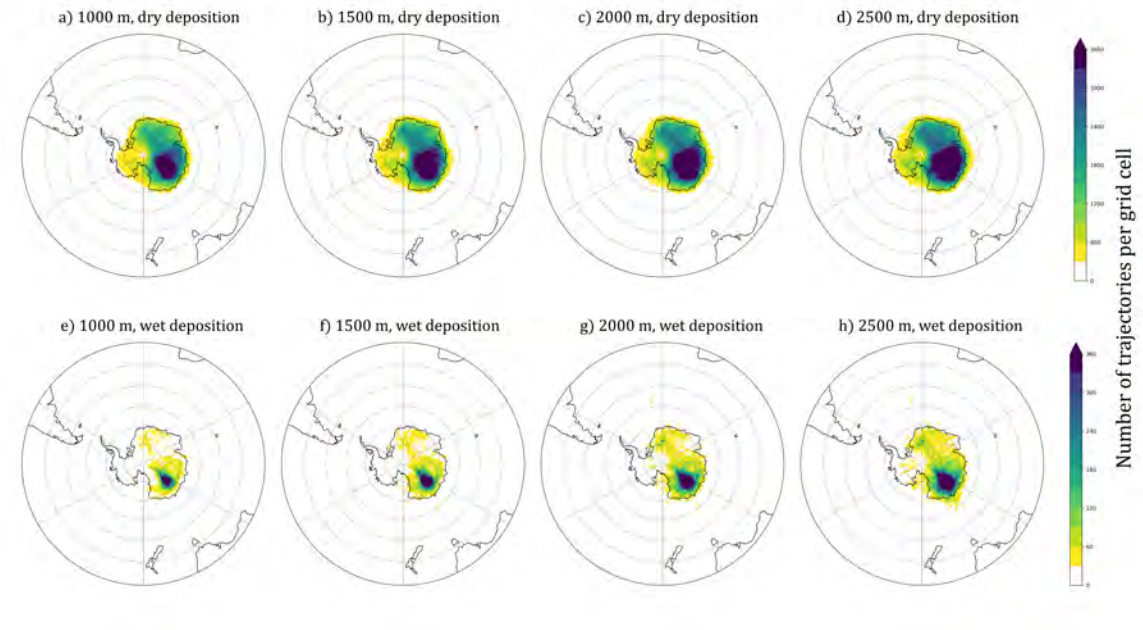

Figure 4.4: Density of trajectories per grid point for the different boundary layer height criteria 1,000, 1,500, 2,000, and 2,500 m for dry deposition (a to d) and wet deposition (e to h).

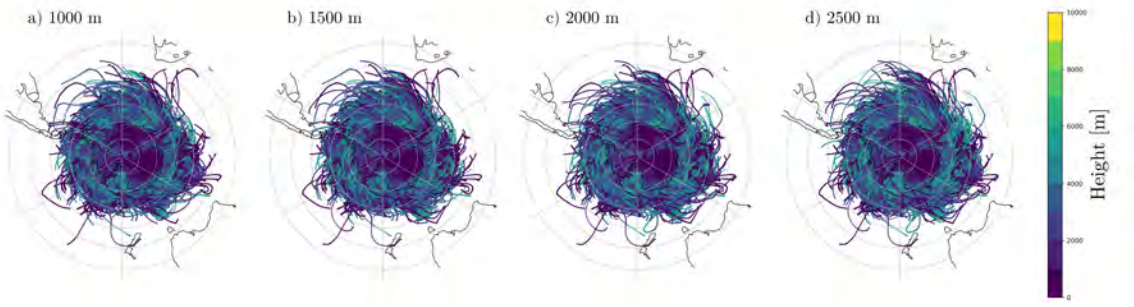

Figure 4.5: Boundary layer height criteria a) 1,000, b) 1,500, c) 2,000, and d) 2,500 m. The shading characterizes the trajectories' heights at each point.

of wind speed $\vec{v}_{10}$ =4 m s^{-1} for SSA formation. However, as discussed in Section 2.1.2, a significant background concentration of SSA over the ocean exists. Hence, for an air parcel to take up SSAs, their respective formation does not need to have occurred immediately before uptake, and not necessarily in the same grid cell. The two alternatives to this strict threshold are either weakening the threshold (threshold of 3 m s^{-1}) or abandoning a wind criterion altogether because it is not relevant to the presence of SSAs in the air. As shown in Figure 4.6, the differences in the number of trajectories and the trajectory density between the thresholds are minimal. For dry deposition, the number of trajectories for the strongest threshold is $\#_{traj}(4)$ =107,773, while for the weakest threshold, a large number still remains $\#_{traj}(nocrit)$ =107,964. The numbers of trajectories for wet deposition are very close to each other, as well ($\#_{traj}(4)$ =12,594, $\#_{traj}(nocrit)$ =12,605). Thus, we will refrain from using a criterion, as the sensitivity of the threshold is low.

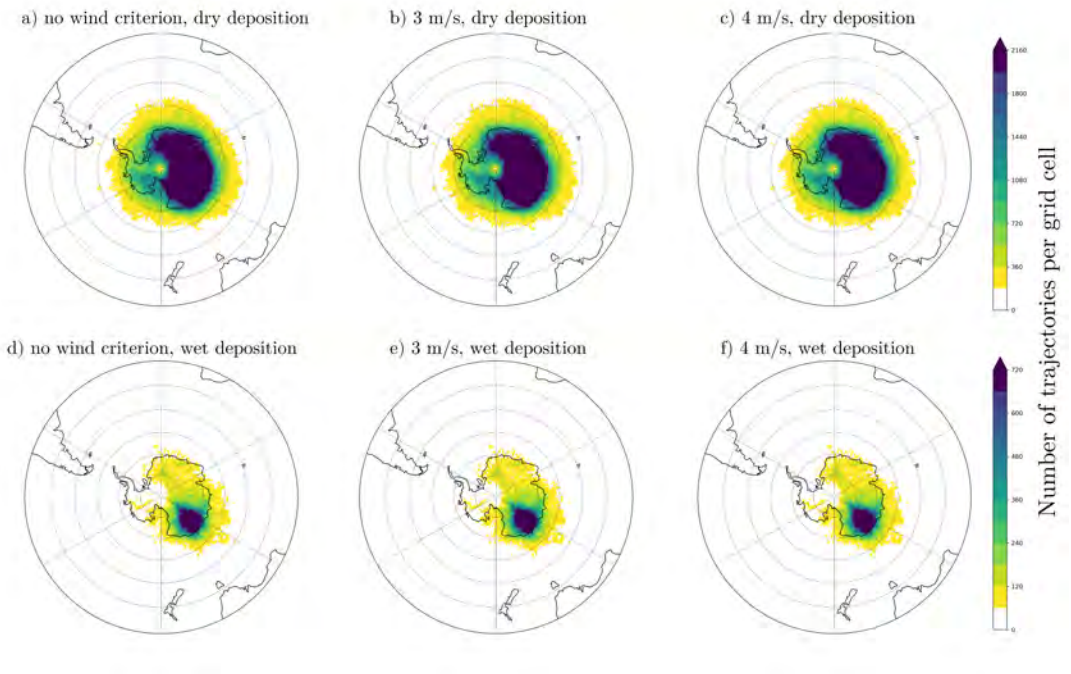

Figure 4.6: Formation criteria for dry (a to c) and wet (d to f) deposition over 15 years with no wind threshold, 4, and 3 m s^{-1}.

4.1.5 End height

With these filter criteria in place, i.e., the literature-given dry deposition criterion at Dome C of wind speed below 5 m s^{-1}, wet deposition at precipitation over 0.01 mm $hour^{-1}$, transport as long as cumulated precipitation over the last 24 hours is less than 3 mm day^{-1}, and height of trajectory below 2,500 m, the impact of the end height of a trajectory over Dome C is considered. We ran the FLEXTRA calculations from three designated end heights of 50 m, 500 m, and 1,500 m, with the intention to check the height sensitivity.

As is shown in Figure 4.7, showing the input points for the three heights, split into wet and dry deposition, it is clear that for the deposition types, source regions are comparable. The three heights contribute approximately evenly to the total number of trajectories (32 to 34% each in dry deposition and 29 to 36% in wet deposition). However, trajectories that are washed out over Dome C start 19% further away from it when they end at 50 m altitude compared to 1,500 m, while the dry-deposition trajectories all cover similar distances, independent of their end heights. Additionally, trajectories ending at 50 m can take up more aerosols, i.e. have more input points, according to the filtering, with an increase of 20% for wet deposition and 6% for dry deposition from 1,500 m to 50 m height. For the trajectories during the LGM, similar results have been obtained (cf. Appendix 7.1). As aerosols from any height can be deposited, we use all end heights.

4.2 Impact of temporal and spatial resolution on trajectories

As already mentioned in Section 3.1, the reanalysis ERA5 and the model CESM1.2 have different temporal resolutions: ERA5 data is resolved hourly, while CESM1.2 data is output every six hours. The effect of temporal resolution on the tracking of trajectories is tested by running FLEXTRA with 6-hourly ERA5 data and comparing the results to trajectories obtained with 1-hourly ERA5 data, both for 10 years. To make a fair comparison, we use only the 00, 06, 12, 18 GMT time steps of the trajectories based on 1-hourly data. The input points of trajectories show similar patterns (cf. Figure 4.8). The bulge in the Atlantic sector is present in both plots depicting the dry deposition, i.e., Figure 4.8a and b, and for

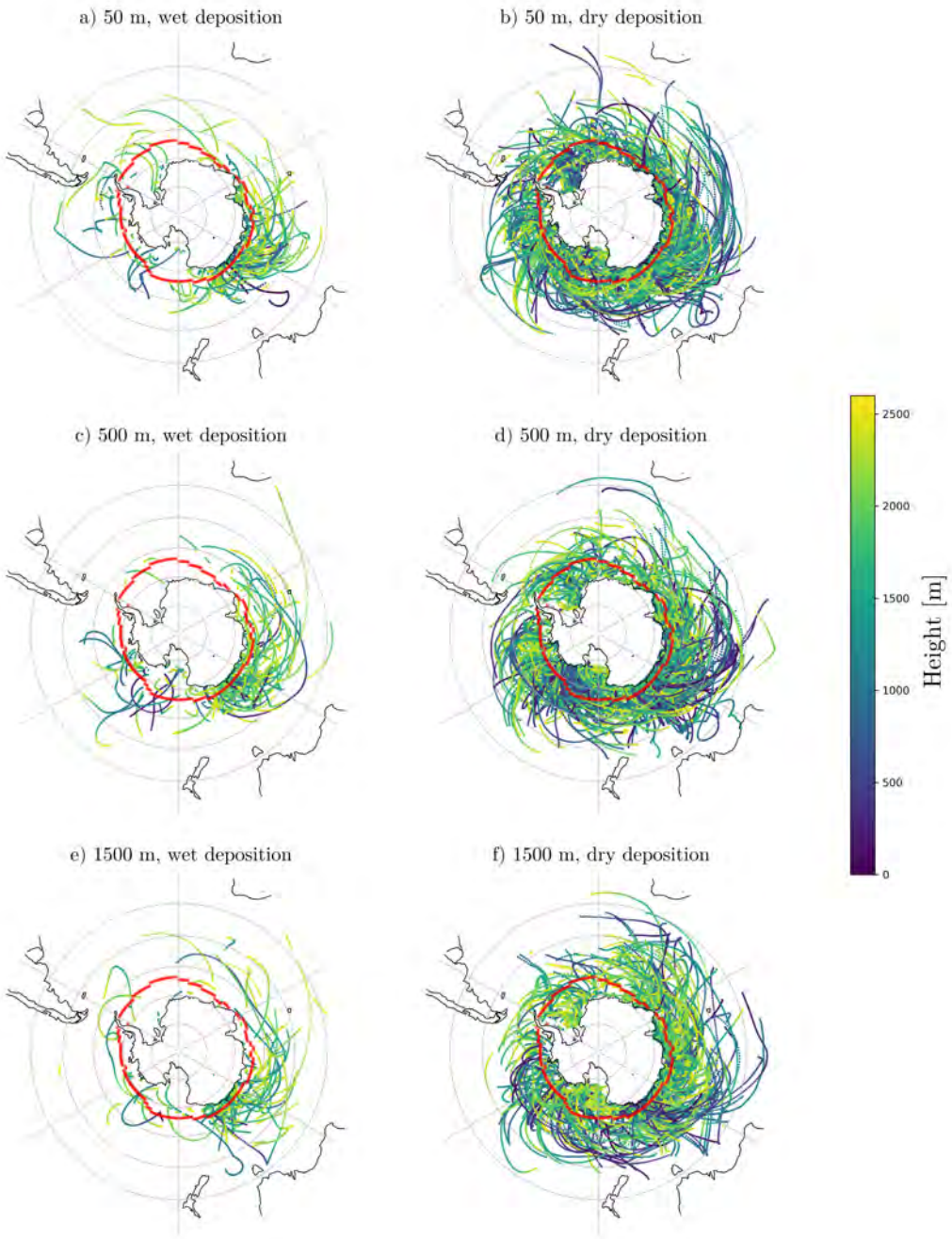

Figure 4.7: Input points for the different end heights over Dome C of 50 m (a and b), 500 m (c and d), and 1,500 m (e and f) for wet and dry deposition in the PI. The colors show the height of the trajectories, and the red line depicts the sea ice cover of 50%.

wet deposition, the highest number of input points originate off the coast of Dome C in the direction of Australia in Figure 4.8d and e. However, the difference plots Figure 4.8c and f show the pathways of trajectories are dependent on the temporal resolution of the input data, as they vary on a small scale. Both around the Antarctic coast and at lower latitudes, more of the 1-hourly trajectories are left. This is expected, as higher temporal resolution leads to more variability in the trajectory, resulting in more input points that can satisfy the criteria. This interpretation is supported by the number of trajectories that survive the filtering when they are calculated on 1-hourly resolution ($\#_{traj}(1h)$ =18,039) as opposed to 6-hourly ($\#_{traj}(6h)$ =14,669). The higher resolution, however, does not enlarge the trajectories, as the mean distances of the trajectories' starting points to Dome C are $\overline{d_{6h}}$ =3,467.7 km and $\overline{d_{1h}}$ =3,463.9 km. The time they spend in the air is also similar, with $\overline{t_{6h}}$ =175.0 hours and $\overline{t_{1h}}$ =174.8 hours. Overall, an impact of the input data's temporal resolution is present and influences the number of trajectories. However, the low resolution still reproduces the source regions and is sufficiently accurate for the purposes of this study.

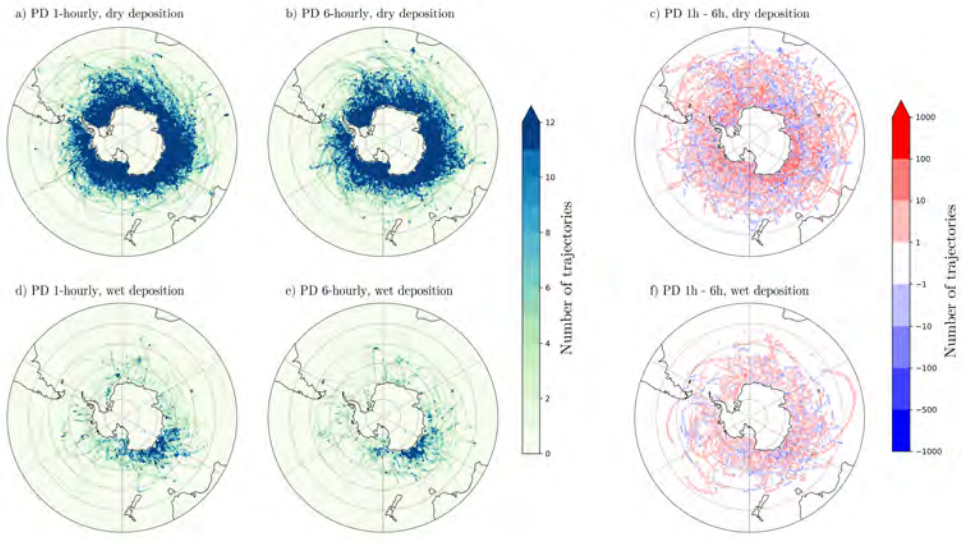

Figure 4.8: Amount of starting points per grid cell between every sixth trajectory of 1-hourly ERA5 PD scenario (a and d) and all trajectories of 6-hourly ERA5 PD (b and e) and their differences (c and f) of dry (a to c) and wet deposition (d to f).

The mother grid of ERA5 is a 0.25°×0.25° grid. To provide an overall analysis of the resolution's impact on FLEXTRA output, we studied not only temporal but also spatial influence. Exemplarily, owing to the large data size, only one summer and one winter month of high spatial resolution were compared to those months of 1° resolution. The summer month, January, shows great similarities in trajectories between the two spatial resolutions (cf. Figure 4.9). Both the pattern and the number of trajectories after filtering are very alike, this holding true for dry deposition (Figure 4.9a and b, $\#_{traj}(1°)$=791 and $\#_{traj}(0.25°)$=771), and wet deposition (Figure 4.9d and e, $\#_{traj}(1°)$=140 and $\#_{traj}(0.25°)$=143). The same is shown in Figure 4.10 for the winter month of June, where the differences between the two resolutions are more pronounced. It is striking that the number of trajectories differs strongly for dry deposition ($\#_{traj}(1°)$=265 and $\#_{traj}(0.25°)$=103) and wet deposition ($\#_{traj}(1°)$=93 and $\#_{traj}(0.25°)$=21), and in the high resolution, the trajectory number is reduced to approxi-

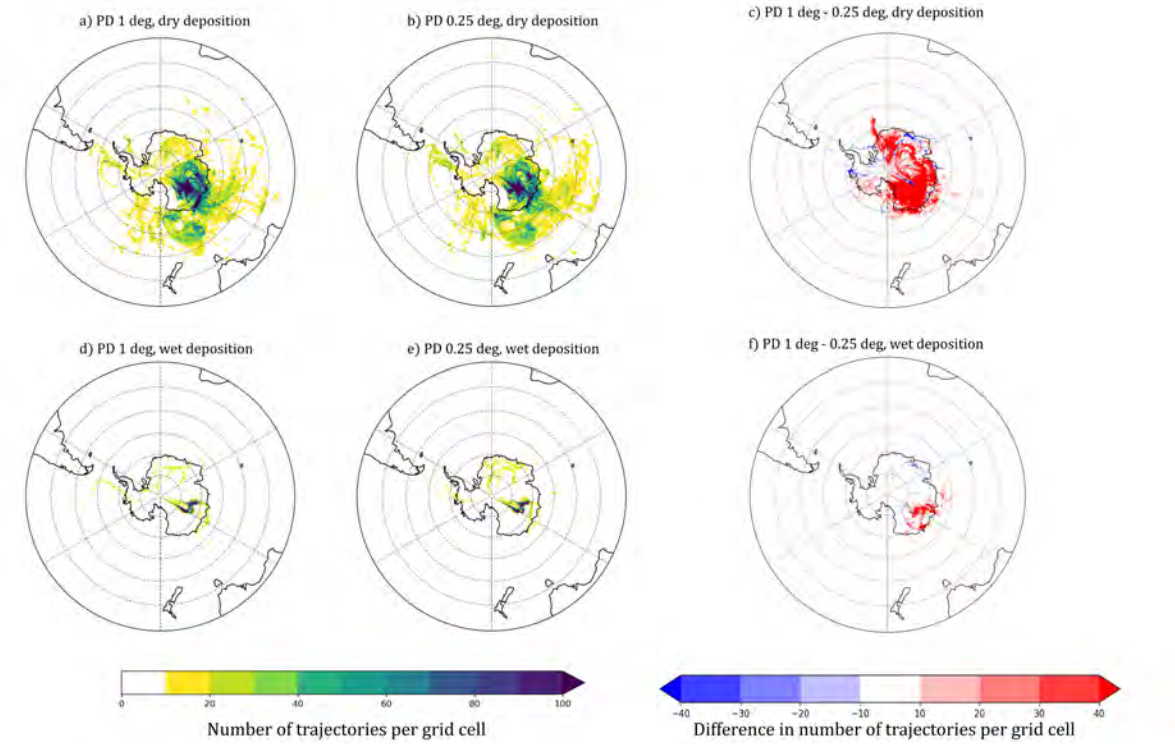

Figure 4.9: Number of trajectories of 1° input data (a and d) and 0.25° input data (b and e) and the differences in their input points (c and f) of dry and wet deposition for January 1990.

mately a third to fourth of the number of trajectories in low resolution. Moreover, for June, the differences between trajectories per grid point are less pronounced than for January, but this can also be attributed to the smaller number of overall trajectories potentially carrying aerosols in winter. In conclusion, we can state that in austral summer, the low-resolution trajectories behave similarly to the trajectories calculated from high-resolution data, while the number of trajectories is higher in the lower than in the high resolution in June.

Finally, as highlighted in Section 3.1, besides a variation in horizontal resolution, we deal with a drastic difference in vertical resolution as well. In particular, while ERA5 features a total of 137 levels, CESM1.2 uses only 30 levels. However, the effect of vertical resolution on FLEXTRA trajectories lies outside the scope of this work and was therefore not tested in this study and must be grouped together with the other differences between the datasets, which

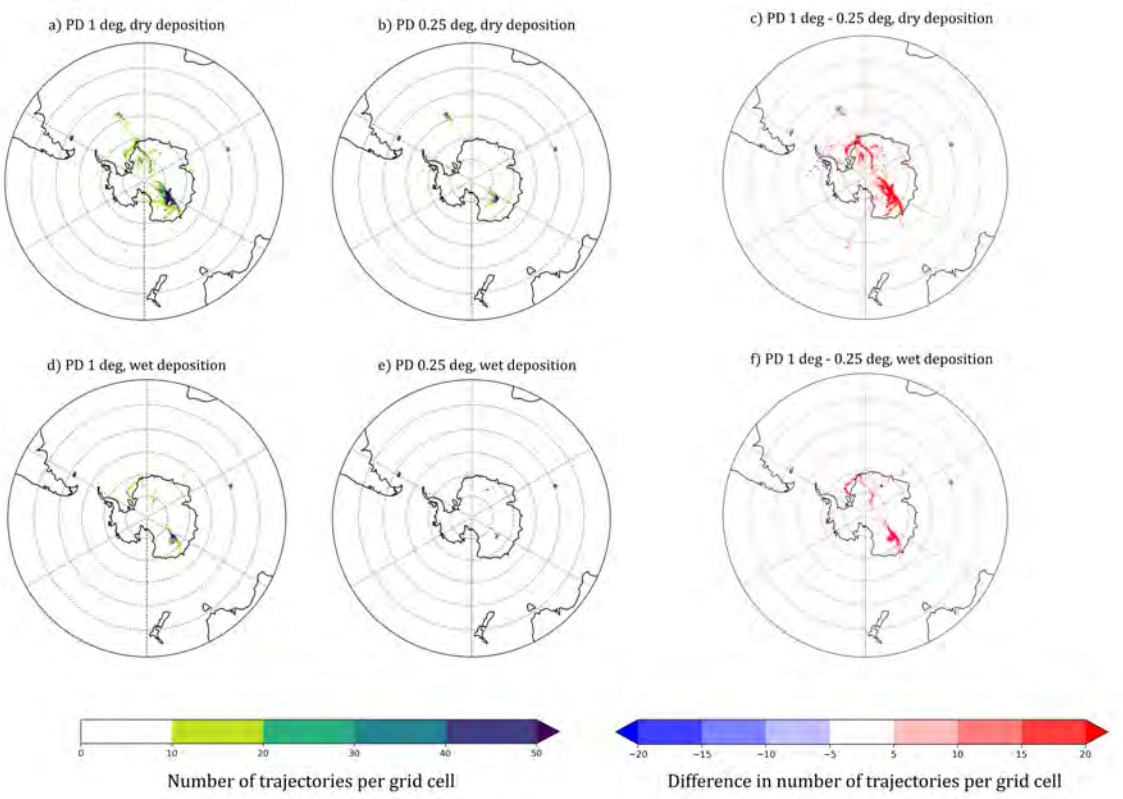

Figure 4.10: Number of trajectories for 0.25° input data (a to c) and 1° input data (d to f) for June 1990.

are listed in the following section.

4.3 Comparison of ERA5 and CESM1.2

Besides the impact of resolution differences analyzed in Section 4.2, the inherent biases of the CESM1.2 simulation that are described in Section 3.1.2 can also impact the trajectories calculated by FLEXTRA. Another effect is that CESM PI represents conditions of 1850, whereas the ERA5 PD reflects the period from 1990 to 2000. To estimate the effect that using different datasets for the trajectory calculation has on trajectories and input points, we compare trajectories from the two datasets, for ERA5 PD and CESM1.2 PI, both from 6-hourly data on a 1°×1° resolution, and for 10 years. To get a first overview, we assess the distance and time traveled by the air parcels in CESM1.2 PI and ERA5 PD. As indicated in Figure 4.11, the mean distances and time lengths of trajectories are very similar for CESM PI and ERA5 PD runs. However, since CESM PI trajectories cover a slightly smaller distance, their starting points are closer to Dome C, while the time spent in the air is minimally larger for dry and smaller for wet deposition. All in all, the respective differences between CESM PI and ERA5 PD are small.

To further investigate the changes in source regions between ERA5 and CESM1.2, we split

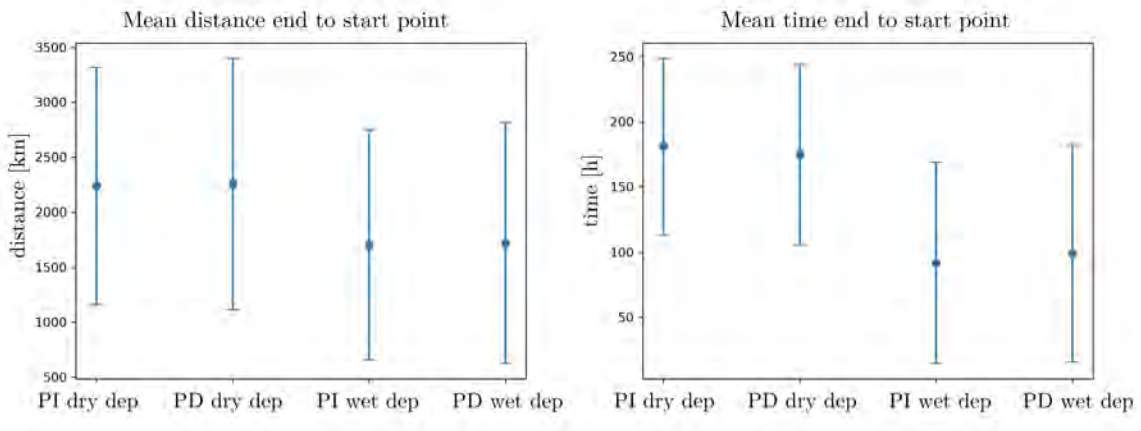

Figure 4.11: Mean distance and mean time difference and their standard deviations of trajectories between start and end points for CESM PI and ERA5 PD.

the trajectories into three regions, according to the input points' density patterns which are shown in Figure 4.12. Region 1, located in the direction of Australia and the Indian Ocean, also includes Dome C. Region 2 covers the sector of Africa and the Atlantic Ocean, while Region 3 covers the Pacific Ocean and includes New Zealand.

The correlations between the time series of the number of starting points of the regions already provide insight into the importance of the regions in generating potential sea salt aerosols. As there are so few wet deposition trajectories, we analyze dry deposition only. Figure 4.13 shows that in the ERA5 PD, the regions do not correlate strongly with each other. However, the correlation of each region with the total amount of starting points highlights the contribution of each region, which is highest in Region 2, followed by Region 1.

For CESM PI, the correlation is shown in Figure 4.14, where Region 1 has the largest impact on overall aerosol amount, with Regions 2 and 3 being significantly smaller, while the correlation between Region 1 and 3 is close to zero. Especially in the case of CESM PI, it must be taken into account that the regression is heavily influenced by a few outliers, and only serves as an estimation of the regions' influences on total aerosol flux.

The origin of the outliers and the reasons for the different influences of Region 1 and 2 can be inferred from Figure 4.15, where the annual cycle of total number of starting points from each region is depicted for ERA5 PD and CESM PI. For better comparability of the two times, the ERA5 PD data is the one with a 6-hourly resolution as in Section 4.2, so both simulations have the same temporal resolution, and a spatial resolution of $1°\times1°$. These resolutions are in place for the rest of the comparison of the two datasets. While the overall seasonal cycle is similar for both times for dry and wet deposition, it is much more pronounced in the CESM PI. Generally, dry-deposited SSAs are more likely to be transported to Dome C in the summer months (November, December, and January), while fewer trajectories reach Dome C in the months of June to September. CESM1.2 also represents the order of magnitude of wet deposition well compared to ERA5 PD, where wet deposition is about ten times smaller than that of the dry deposition, and the spike in wet deposition from June to September. However, the austral summer months are strongly overestimated in both dry and wet deposition, with peaks in December, January, and February. The overall amount of trajectories leaving from

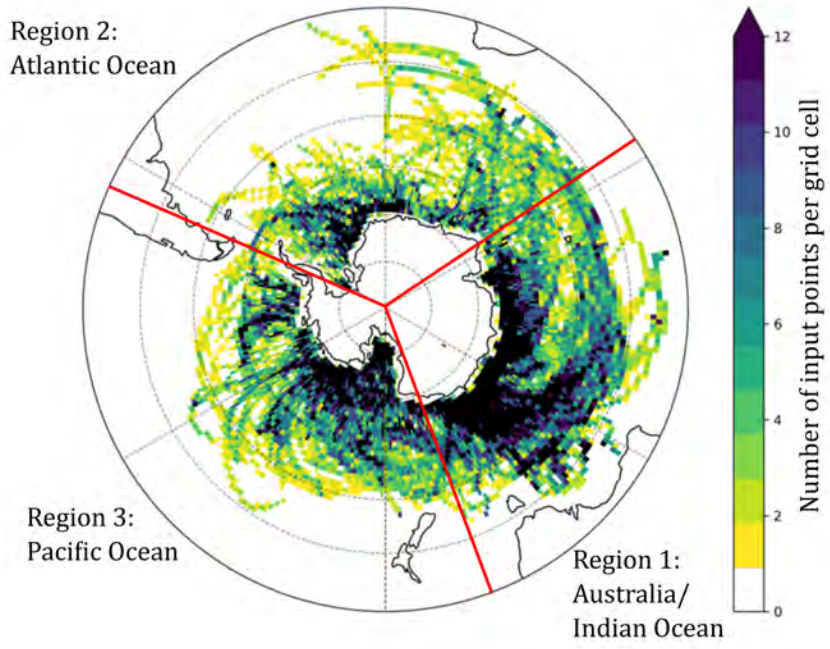

Figure 4.12: Locations of Region 1: Australia/Indian Ocean (from 54° E to 165° E), Region 2: Atlantic Ocean (from 70° W to 54° E), and Region 3: Pacific Ocean (from 70° W to 165° E). The shading gives the density of input points in CESM1.2 PI summer.

Region 2 agrees well between the two datasets, but in CESM1.2, Region 1 is mostly responsible for the peaks in austral summer, and Region 3 is strongly overestimated.

However, when analyzing the total number of input points per month, we get an entirely different picture, as can be gathered from Figure 4.16. Again, for both wet and dry deposition, most noticeable is the peak in austral summer. Besides that, the influence of the different regions is different in CESM1.2. Region 1 and 2 contribute the most aerosols into the trajectories in all months for dry deposition in the ERA5 PD, with Region 2 being a slightly stronger source. Over the course of a year, Region 3 constantly adds only low numbers of input points. For the dry deposition in the CESM PI, on the other hand, most of the input points are located in Region 1, while Regions 2 and 3 have similar, smaller contributions. The peaks are Region 3 in March, and Region 1 in August, which do not correspond with the

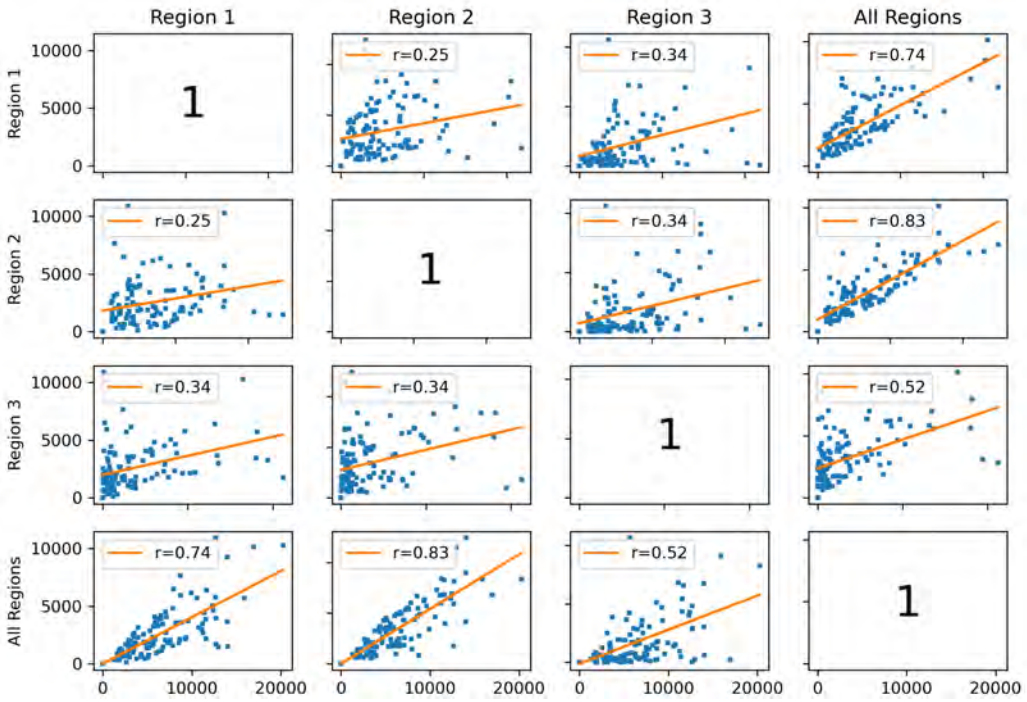

Figure 4.13: Correlations of the time series of the number of trajectories in Region 1, Region 2, Region 3, and all regions for ERA5 Present Day for dry deposition.

ERA5 PD, since the number of trajectories shows dips there. Overall, the two datasets show very different patterns. However, if one assumes the January peak to be a bias in the model, and smooths it out, there are three peaks in each ERA5 PD and CESM PI, respectively: one in autumn (April and March), winter (July and August), and spring (October and November). Besides that, though, the influence of the three regions is very different, with Region 2 being the main contributor in ERA5 PD, but the weakest in the CESM PI. Both Region 1 and 2 are underestimated in CESM1.2. However, based on the comparison with ERA5 PD, CESM1.2 proves more capable when simulating wet deposition than for dry deposition. Even though the model still underestimates Regions 1 and 2 and shows the peak in January and December, the large peak from June to October is present in both wet deposition plots, and a smaller peak in April.

The input of sea salt aerosols into trajectories in the ERA5 PD is relatively evenly distributed over the years (cf. Figure 4.17a). In the CESM PI, however, the strong influence of summer

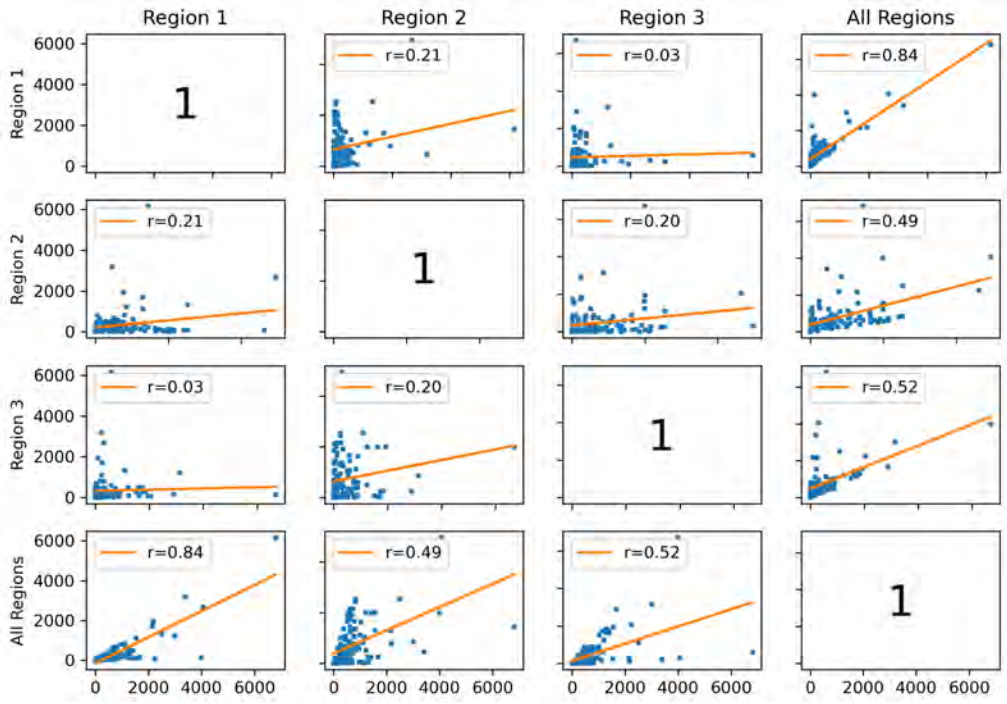

Figure 4.14: Correlations of the time series of the number of trajectories in Region 1, Region 2, Region 3, and all regions for CESM1.2 Preindustrial for dry deposition.

months, especially January, is shown in the strong peaks again, but not every year.

To assess the January bias in CESM1.2 PI, we investigate the atmospheric circulation by comparing geopotential height of mean January and the yearly mean in ERA5 PD and CESM PI (cf. Figure 4.18). While the four plots displaying total geopotential height all feature similar patterns, with the circumpolar trough around Antarctica and slightly higher pressure over Antarctica, the ERA5 January anomaly in Figure 4.18c depicts comparably high pressure over Antarctica and the surrounding Southern Ocean during the ERA5 PD. A more or less uniform increase in pressure leads to similar wind velocities as before, and thus ERA5 PD January trajectories behave similarly to the rest of the year. The CESM PI January anomaly, on the other hand, shows a strong positive pressure anomaly around Antarctica in January, while pressure over East Antarctica stays the same. This suggests a weakened circumpolar trough in January, leading to weakened westerly winds where it is easier for trajectories coming from the north to break through the otherwise strong winds and flow towards Antarctica.

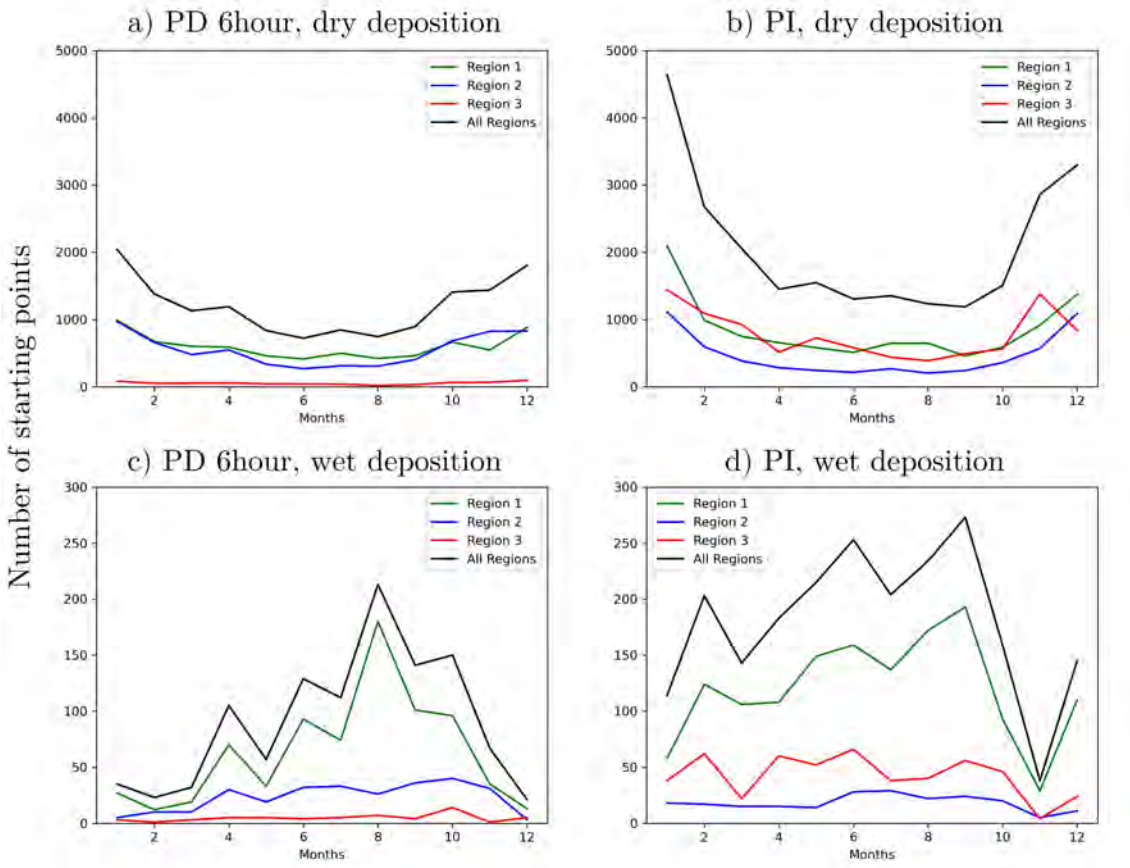

Figure 4.15: Mean annual cycle of starting points per region over 10 years in a) ERA5 PD, dry deposition, b) CESM1.2 PI, dry deposition, c) ERA5 PD, wet deposition, and d) CESM1.2 PI, wet deposition. The ERA5 PD is calculated on a 6-hourly resolution for the order of magnitude to be comparable.

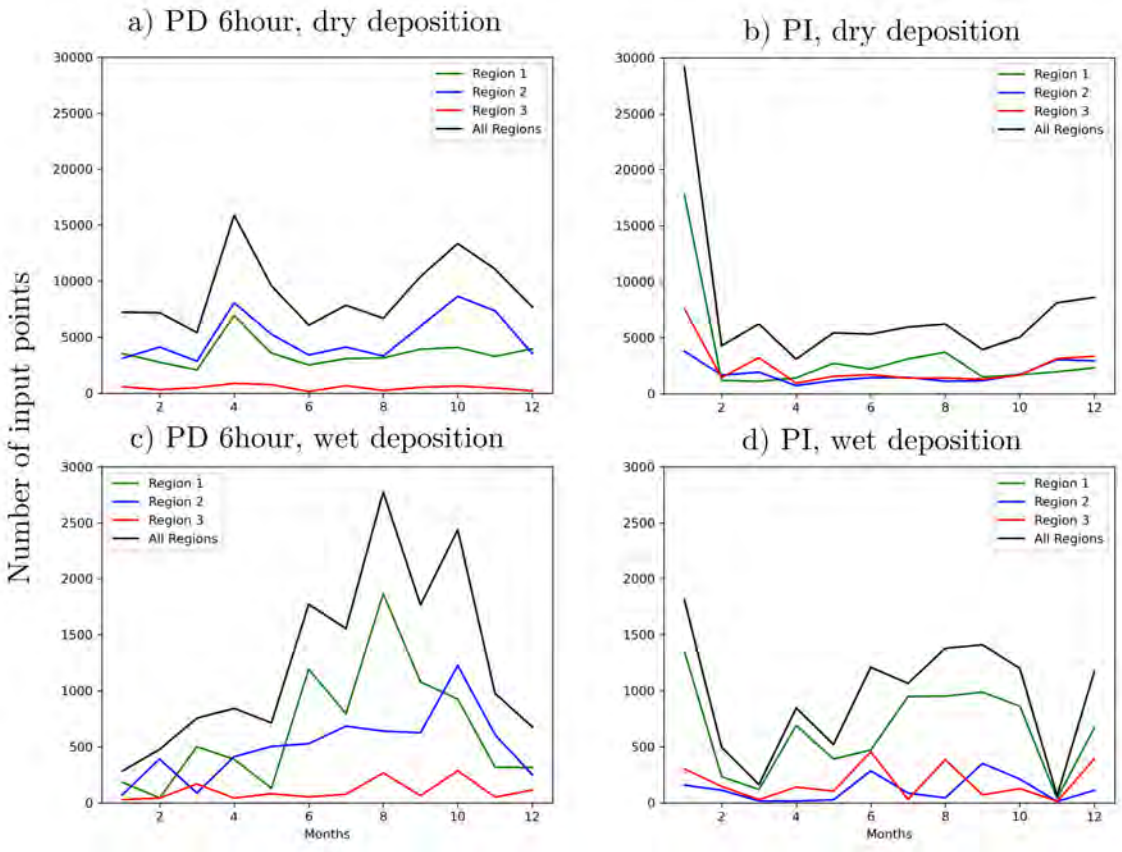

Figure 4.16: Mean annual cycle of input points per region over 10 years in a) ERA5 PD, dry deposition, b) CESM1.2 PI, dry deposition, c) ERA5 PD, wet deposition, and d) CESM1.2 PI, wet deposition. The ERA5 PD is calculated on a 6-hourly resolution for the order of magnitude to be comparable.

To find an answer as to why the peak in January only emerges in some years, we will analyze the geopotential in selected Januaries (cf. Figure 4.19). We have chosen January of the model years 4 and 3, months with the highest peak, and a regular peak in trajectory number, respectively, and their differences, both in geopotential height and the trajectories present. While at first glance, the patterns of geopotential height look similar, their differences underline a strong local increase in pressure in Region 3, the direction of the Pacific. The trajectories, coming from Region 1 and following the westerly winds, are blocked by the high-pressure area. Thus, the geostrophic wind, which aligns itself parallel to pressure lines, turns south-

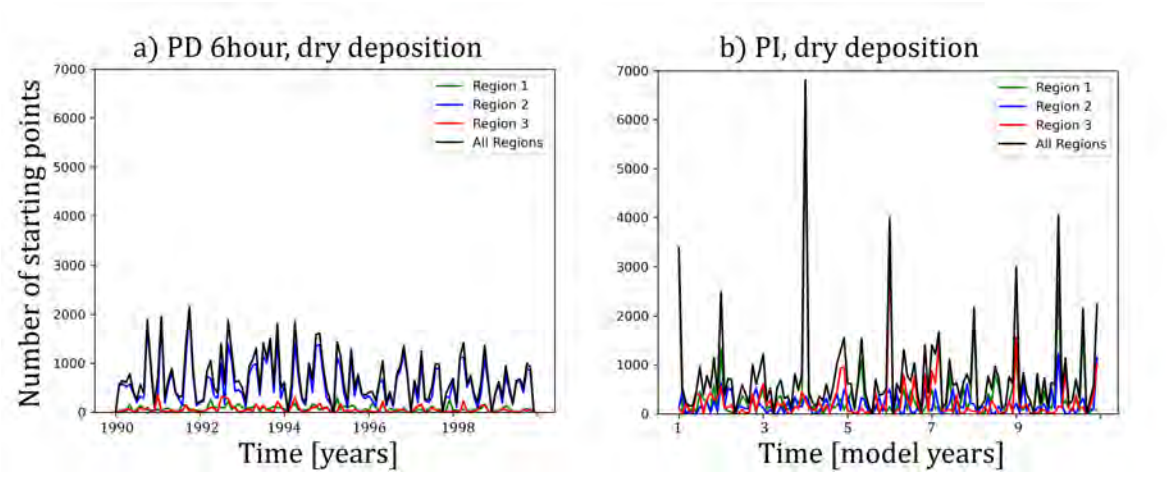

Figure 4.17: Monthly amount of input points for 10 years per region in a) ERA5 PD, dry deposition, and b) CESM1.2 PI, dry deposition. The ERA5 PD is calculated on a 6-hourly resolution for the order of magnitude to be comparable.

ward, enabling more trajectories to reach Dome C. This hypothesis also explains the number of trajectories (Figure 4.19d and e), but especially their differences (Figure 4.19f), where the strongest positive difference in trajectories is located between Antarctica and Australia, which is just west of the high-pressure region.

4.4 LGM and PI

The differences between the Preindustrial and the Last Glacial Maximum are presented in this chapter. For both time periods, CESM1.2 data is used, for 15 years in both cases. Keep in mind the CESM1.2 biases explored in the last section, and how they influence the resulting trajectories, especially the spike in trajectories in the summer months, and the underestimation of Regions 1 and 2. However, since we compare two simulations of the same model, the biases should be negligible when looking at the changes between the two.

4.4.1 Impact of LGM and PI on Sea Salt Aerosol trajectories

This section reports the changes in sea salt aerosol trajectories from the Last Glacial Maximum to the Preindustrial modeled by CESM1.2. The first characteristic we consider in the

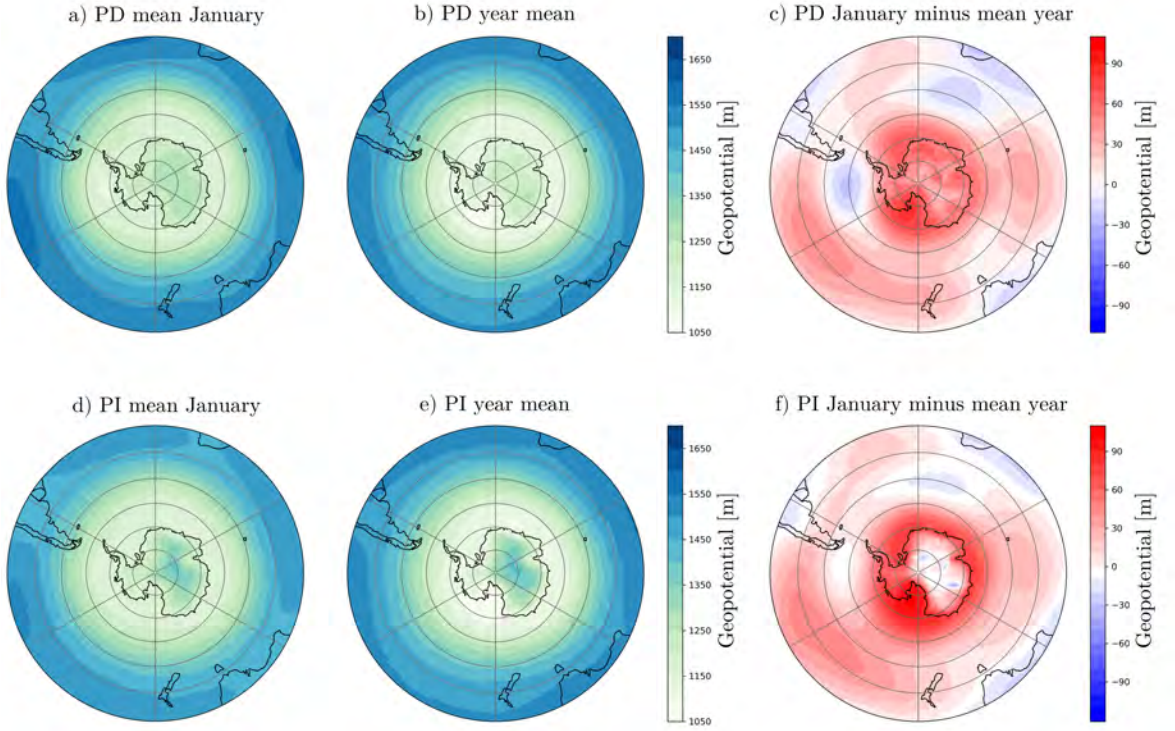

Figure 4.18: Mean 850 hPa geopotential ERA5 PD (a to c) and CESM1.2 PI (d to f) of January (a and d), the whole year (b and e), the effective change in geopotential in January compared to the whole year (c and f).

comparison between LGM and PI are the mean distance of the starting points to Dome C and the mean time of the air parcel spent in the air (cf. Figure 4.20). Both distance and time are slightly higher in the mean during the LGM than during the PI, for both wet and dry deposition. This is expected, as the climate was much drier in the LGM, and fewer aerosols were washed out of the air parcels on the trajectories. Additionally, the wet-deposition trajectories spend a significantly shorter time in the air than the dry-deposition trajectories, which is in agreement with our findings for ERA5 PD, since wet deposition generally occurs in periods of higher precipitation, where washing out is more likely (cf. Section 4.3).

Using the same regions as in Section 4.3, Figure 4.21 shows the number of starting points of the trajectories. The annual cycle for the dry-deposition trajectories is very similar during

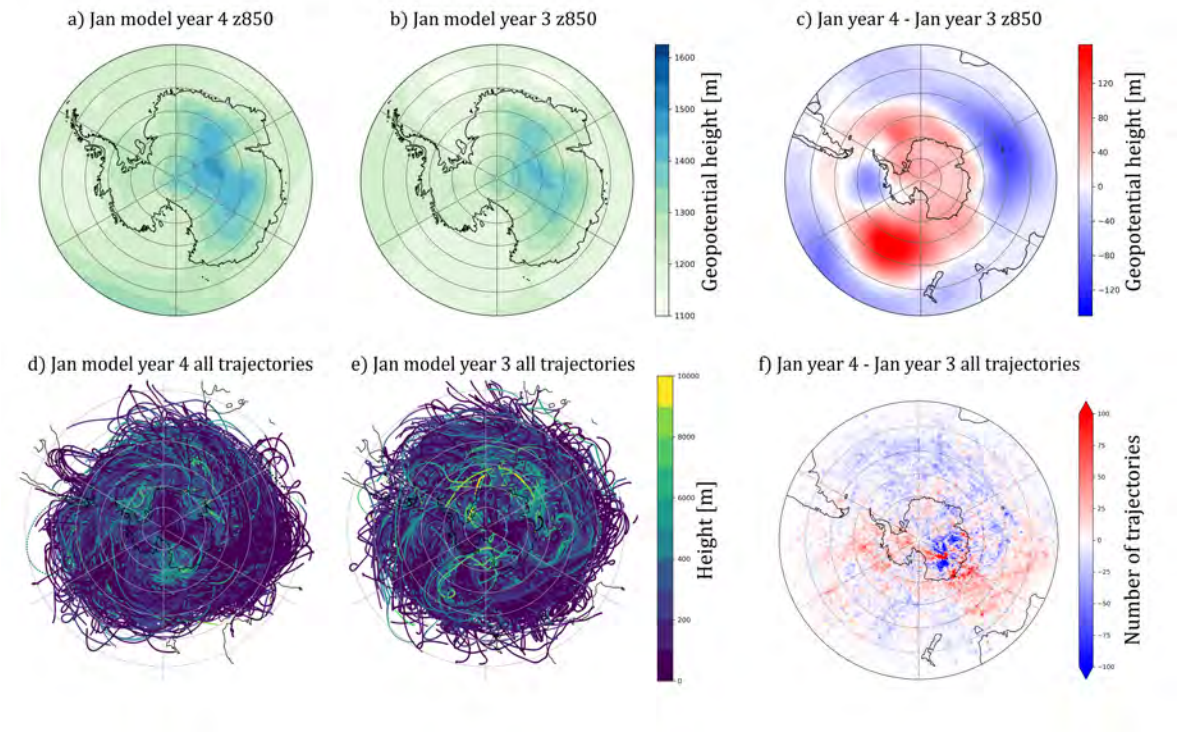

Figure 4.19: 850 hPa geopotential (a to c) and trajectory number (d to f) of January 1907, the month with the highest spike (a and d), January 1906, a month with trajectory number comparable to ERA5 PD (b and e), and their differences (c and f).

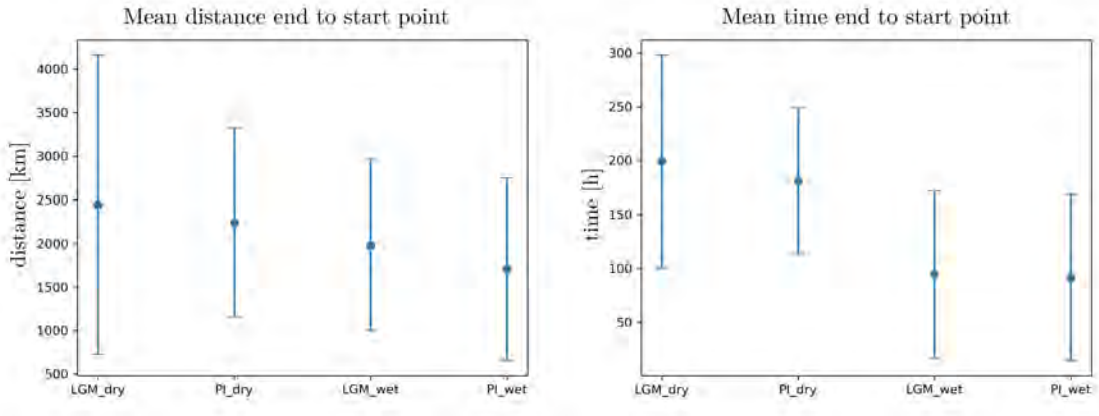

Figure 4.20: Mean distance and mean time difference and their standard deviations of trajectories between start and end points for LGM and PI.

the PI and the LGM, with maxima in summer and minima in winter (cf. Figure 4.21a and b). The small autumn peak shifts from May in the PI to April in the LGM, according to the seasonal shift outlined in Section 2.2. Each region adheres to the overall annual cycle, but we see more starting points in Regions 1 and 3 than in Region 2 in both the PI and the LGM. However, the number of selected trajectories reaching Dome C is slightly higher during the LGM for every month. The opposite holds true for wet deposition (Figure 4.21c and d), where the number of trajectories is an order of magnitude smaller in the LGM than in the PI, due to the aforementioned lower precipitation in the LGM, which reduces the total number of days where precipitation at Dome C is above the precipitation threshold. Aside from that, the peaks of the annual cycle are slightly shifted in the year, from June and September in the PI to May and August in the LGM. This shift in dry and wet deposition suits the orbitally induced change in season from LGM to PI very well. However, while all other peaks are shifted backward in the LGM, the strong peak in summer that was highlighted in Section 4.3 and seems inherent to CESM1.2, does not shift between the two time periods but shows maxima in January and December, and a relatively high value in November in both Figure 4.21a and b.

Figure 4.22 shows the number of points where aerosols can be taken up by air parcels per region. For dry deposition (Figure 4.22a and b), we find a strong peak in January, with secondary maxima being more variable. The PI displays spikes in March, and a longer peak from May to August, while LGM peaks appear in April and September. In both periods, PI and LGM, the autumn peak comes from Region 3, and the one in winter has its largest contribution from Region 1. From the orbital forcing, we would expect an autumn peak in February and continuous strong input from April to July in the LGM. Contrarily, however, the LGM peaks occur later in the year than the PI peaks. The number of SSA input points is also significantly higher during the LGM than the PI in all months except for January, which is not the most reliable month in CESM1.2. The number of input points of trajectories with wet deposition (Figure 4.22c and d) is similar to the initial points in Figure 4.21c and d, as the highest contributor of SSAs is Region 1, the summer peak is only present in the PI, but not in the LGM, and the LGM number of wet deposition is strongly reduced compared to the PI

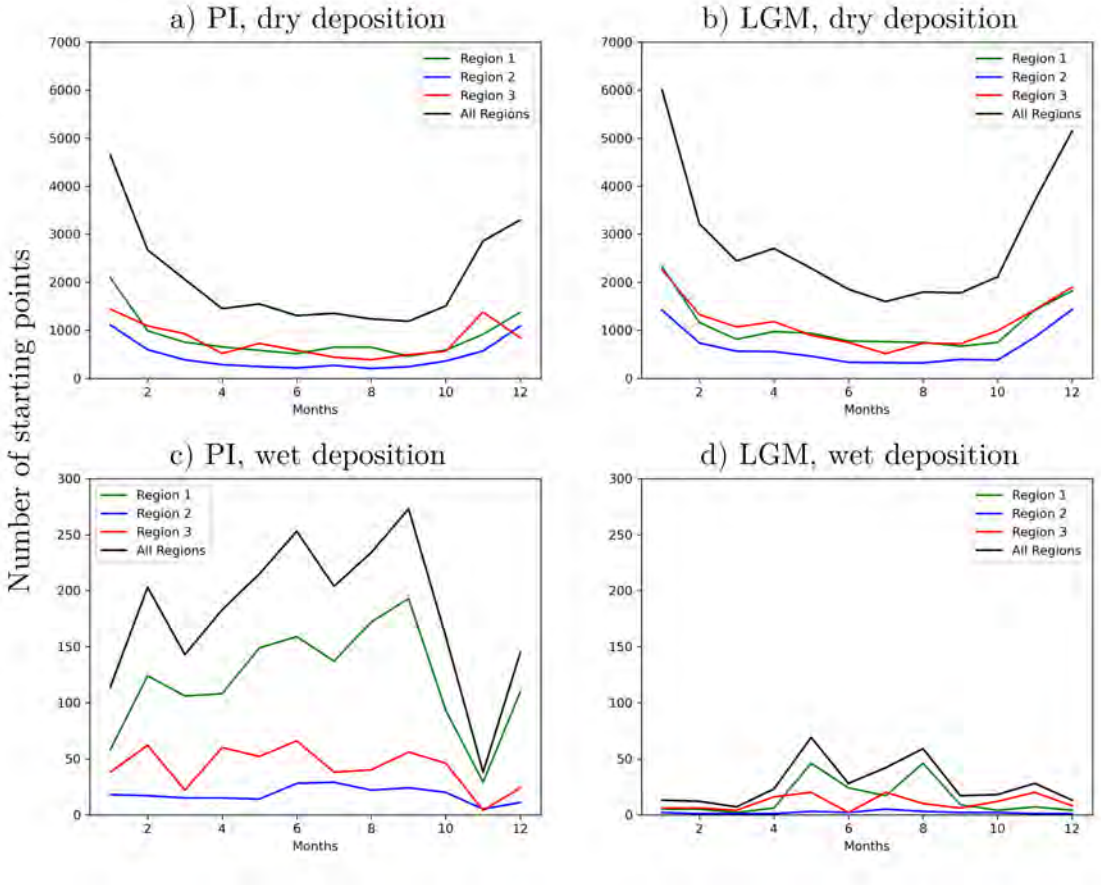

Figure 4.21: Annual cycle of starting points per region in a) PI, dry deposition, b) LGM, dry deposition, c) PI, wet deposition, and d) LGM, wet deposition.

number. Also, the seasonal shift is visible in the peaks, which occur in April and September in the PI, and in March and August in the LGM. However, the peak in June occurs in both PI and LGM and is not shifted according to seasonal climatic changes.

Since the trajectories vary strongly with the season, Figure 4.23 shows the trajectories for each season in the LGM (Figure 4.23a, c, e, and g) and in the PI (Figure 4.23b, d, f, and h). Note that the months for each season are changed in the LGM, due to the orbitally induced seasonal shift during the LGM, as explained in Section 2.2. The summer patterns (Figure 4.23a and b) show that not only do the summer months have the highest number of trajectories, but they also start further away from Antarctica. The sea ice extent (red line at 50% sea ice cover) is smallest in summer and autumn, so there are more opportunities for SSA

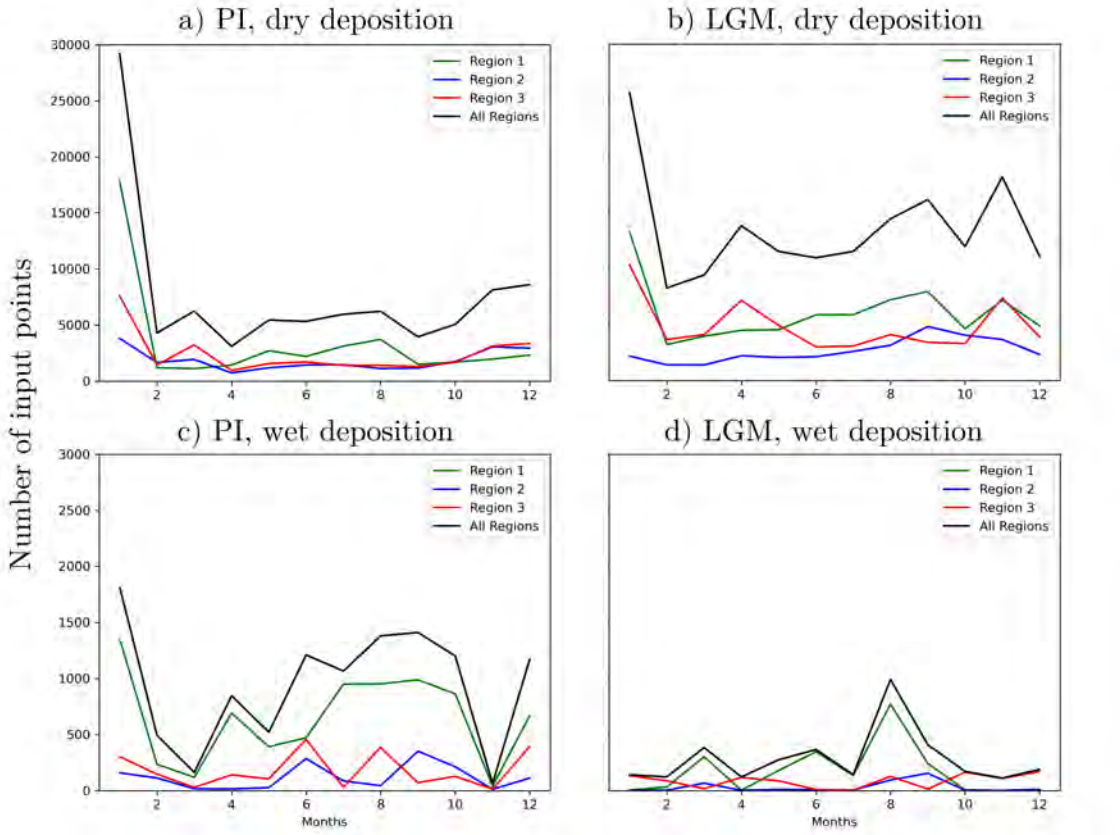

Figure 4.22: Annual cycle of input points per region in a) PI, dry deposition, b) LGM, dry deposition, c) PI, wet deposition, and d) LGM, wet deposition.

uptake over the open ocean. This explains why the January peak is even more pronounced in the input point plot (Figure 4.22) than in the starting point plots (Figure 4.21), because the trajectories spend more time over the ocean and thus consist of more potential input points. In both LGM and PI summer, a clear source region for open ocean sea salt (OOSS) aerosols, i.e., input points from outside the 50% sea ice cover line, is Region 1, e.g., the Southern Ocean in the direction of Australia. Other open ocean source regions include the Indian Ocean in the LGM, and in the PI, the Pacific the Atlantic via the Indian Ocean. We assume that while OOSS aerosols are dominant over oceans with less than 50% sea ice cover, SSAs formed on sea ice (SISS) are prevalent in areas of sea ice cover between 50 and 90%. The latter show different patterns in summer in the two time periods, primarily because of the significantly

larger sea ice extent in the LGM. Here, the SISS aerosols form a large region from the Pacific over Australia to the Indian Ocean, with more input points during the LGM than the PI, whereas a region with fewer input points is found in the Atlantic sector in the LGM. Since in PI summer, the sea ice extent is significantly smaller, potential SISS input regions are limited to the coastal areas and the Ross and Weddell Sea. Besides the large and diverse summer input, the distances of the trajectories vary more in the PI, where the autumn, winter, and spring months barely reach 50°S. However, despite the smaller distances in the PI, the smaller sea ice cover leads to a similar amount of open ocean input points, with input points all around the sea ice line, but slightly more concentrated in the Australian sector. In PI winter, the SISS area is so small that the amount of input points for SISS is negligible. In PI autumn and spring, however, the sea ice line of 90% retreats and leaves more SISS input points all around Antarctica, with the highest concentration again in the Australian direction. The LGM autumn is similar, except that sea ice lines, and thus the source regions themselves, are shifted away from Antarctica. The LGM winter and spring months, on the other hand, have pervasive sea ice extent of over 90%, where we assume no aerosols can be formed because too few water ridges splash seawater onto the ice floes, and the distance to 50% sea ice extent is so small that very few SISS input points remain. These few come from the Australian sector in winter and spring (cf. Figure 4.23e and g), but that input is only slightly higher than from all around the Antarctic 90% line. The few trajectories that have distances large enough to take up OOSS aerosols despite the extended sea ice extent in winter and spring, mostly come from south of Australia, but a smaller area south of Africa also contributes OOSS aerosols.

The wet deposition input points, on the other hand, are distributed very differently. As stated earlier, only very few selected trajectories end with wet deposition at Dome C in the LGM, but wet deposition is not overly common in the PI, either. Figure 4.24a suggests that the summer peak observed in every other CESM summer is missing from wet deposition in the LGM simply because there is not enough precipitation in summer to cross the precipitation threshold to be identified as wet deposition events at Dome C and constitute a summer peak. In the PI, conditions were wetter than in the LGM, leading to a higher contribution of wet deposition in every season (Figure 4.24b, d, f, and h). In both the LGM and PI, very little

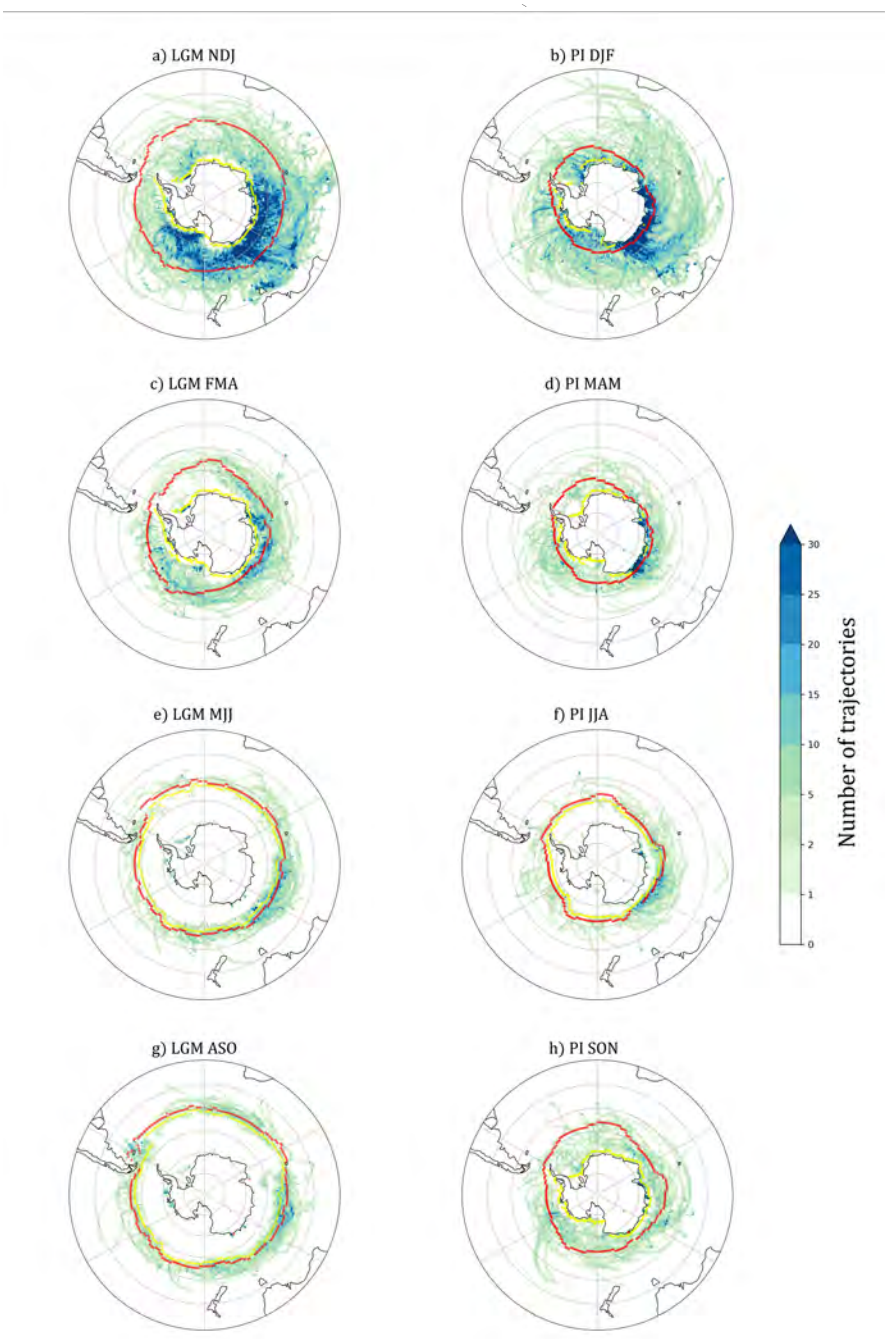

Figure 4.23: Input points of dry deposition for LGM and PI. The LGM seasons are shifted by one month so that they correspond to the maximal summer and winter seasons. The red line depicts a sea ice cover of 50% and the yellow line a sea ice cover of 90%.

seasonality occurs. The strongest seasonal change is evident in the sea ice extent, and thus the distance from Dome C to seawater. This is shortest in summer, where the area between 90% and 50% *ci* is the biggest, leading to a higher number of SISS aerosols. In the other seasons, namely autumn, winter, and spring, the prevalent source region is the open ocean, with an insignificant amount of SISS aerosols. All seasons display a main source region off the coast of Dome C, in the direction of Australia but this is most pronounced in the PI, where the higher concentration of aerosols allows identification of continuous regions rather than just separate, singular trajectories as is the case in the LGM.

As seen in Figure 4.22 and mentioned above, January has a higher number of input points. This signal is not shifted by a month as would be expected due to the change in orbital forcing, so we have a closer look at January in the LGM and PI, as compared to December and February, for dry deposition in Figure 4.25. Again, the red line depicts a sea ice cover of 50%, while the color of each point shows the height of the trajectory at that location. It is immediately visible that not only the number of summer aerosols is determined by the January trajectories, but also the prevalence of regions and the northward extent of input points. Both LGM and PI Januaries receive the strongest SSA contribution from Region 1, with input points close to the Southern coast of Australia. A large portion of trajectories features the westerly wind typical to the circumpolar trough where many trajectories originate in Region 2, are carried to Region 1, and then deposited at Dome C, or start in Region 1, are transported to Region 3, where they turn and subsequently reach Dome C via the Ross Sea. Only a few trajectories form in the Weddell Sea in January in the LGM and in the PI. December and February exhibit different patterns, with significantly fewer input points, and close to none from the Weddell Sea in the LGM December and February (Figure 4.25a and e), while PI December and February display very few input points in the direction of Australia and the Indian Ocean. Aside from the different patterns, the extended source regions, and the substantially higher number of input points, the comparably very low height of input points is remarkable in the January months.

Since in the LGM, wet deposition has a minor impact on overall deposition, the LGM summer months of wet deposition trajectories (Figure 4.26a, c, and e) shed very little light on reasons

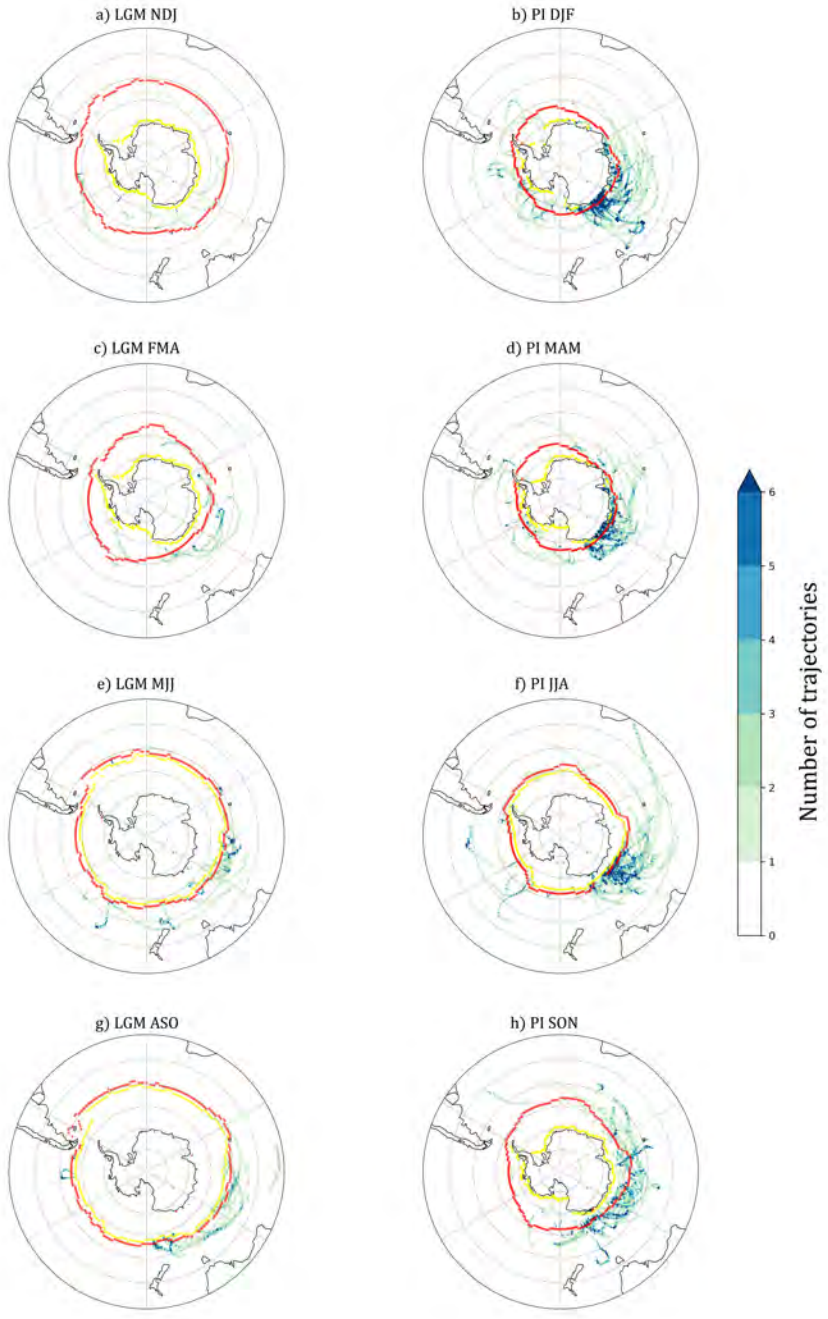

Figure 4.24: Input points of wet deposition for LGM and PI. The LGM seasons are shifted by one month so that they correspond to the maximal summer and winter seasons. The red line depicts a sea ice cover of 50% and the yellow line a sea ice cover of 90%.

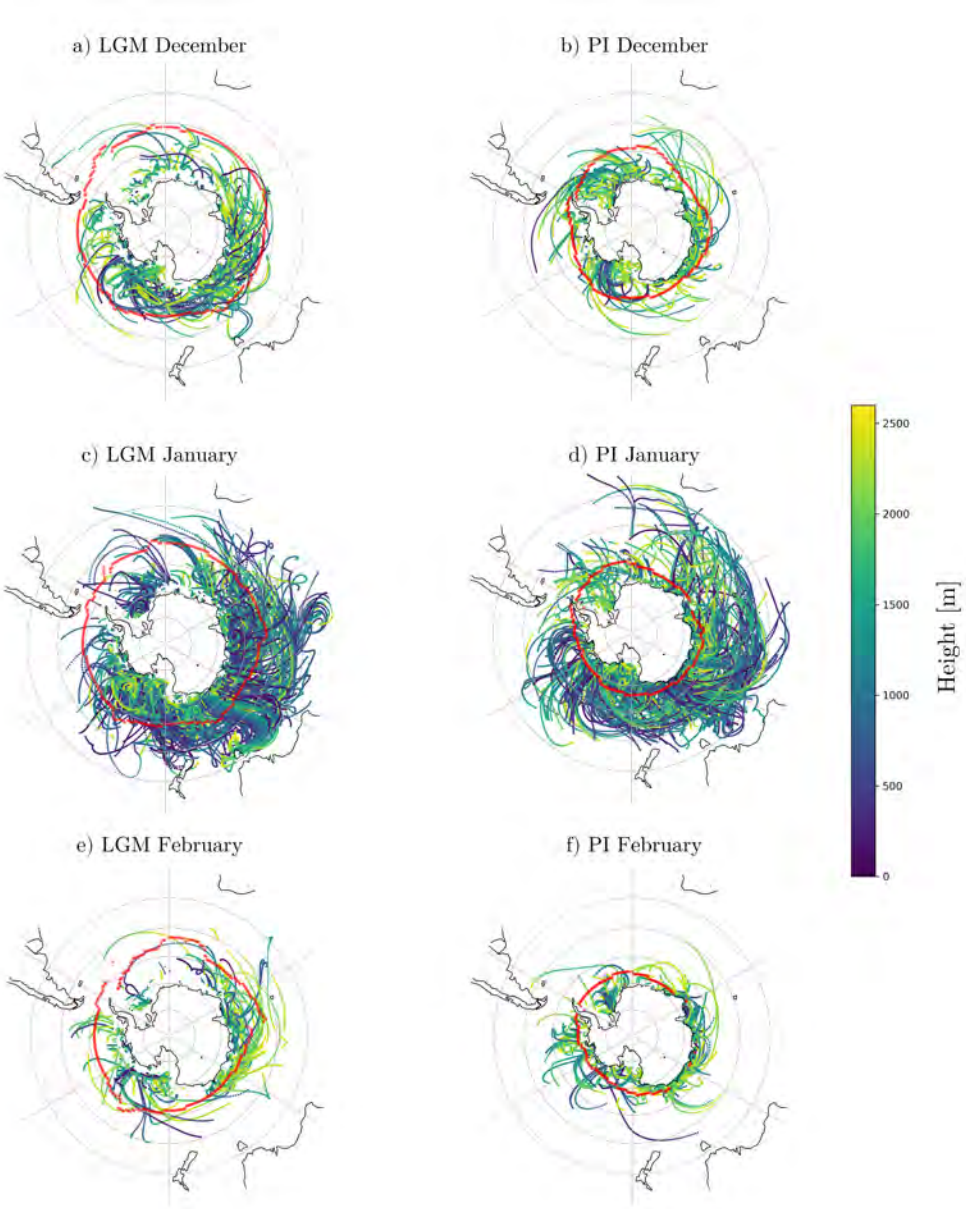

Figure 4.25: Input points for dry deposition for December (a and b), January (c and d), and February (e and f), in the LGM and PI. The color of each point shows the height of the trajectory at that location, while the red line represents the 50% sea ice cover, which is equal to the coastline off Dome C in plot f.

for the January peak. However, PI January (Figure 4.26d) exhibits comparably more low-height input points than its December and February counterparts. Other than the height and the number of input points, the January pattern resembles the other summer months, with a main source region from the sector of Australia, and a few trajectories from West Antarctica.

Figure 4.27 examines the reasons for peaks in the number of wet deposition trajectories in early winter and early spring, with dips in high winter, that are found in both the LGM and PI. Here, the seasonal shift of about four weeks is accounted for by comparing the LGM month to the following month in the PI. In this plot, LGM May (Figure 4.27a) is equivalent to PI June (Figure 4.27b). The peak months (LGM May, PI June, LGM August, and PI September) look similar, with very comparable heights and source regions, mostly from Region 1, except that LGM trajectories make it less far than PI ones, and end very close to the 50% sea ice line. The LGM month that displays a dip in the annual cycle of starting points (June in Figure 4.27c), has much lower trajectory heights than all other winter months shown here, and a very long trajectory. The corresponding month in the PI (Figure 4.27d) exhibits the same source region as the other PI months, similar heights, but shorter trajectories. Thus, there is no distinguishing feature visible that would explain the analogous peaks, except that in PI peak months, several very long, singular trajectories are not washed out. The months with the lowest precipitation in the PI are May, June, and July, which explains the peak of starting points in June, but not why it does not occur in July, nor why it peaks again in September. Also, the lowest precipitation in the LGM occurs in May, but the longest trajectory takes place in June. Even without providing a sound reason for the corresponding LGM and PI peaks in winter and spring, the plot emphasizes how rare input points under 1,000 m height are, and how distinguishable low altitude is in January (Figures 4.25 and 4.26).

Overall, input points of the wet deposition trajectories in the PI make up to 10% of the total input points for trajectories, while in the LGM, wet deposition contributes only 2% of the total. However, the total number of input points in the LGM ($\#_{input}(LGM)$ =159,447) is so much larger than in the PI ($\#_{input}(PI)$ =82,243), that the total atmospheric sea salt concentration over Dome C during the glacial is nearly twice as high than in preindustrial

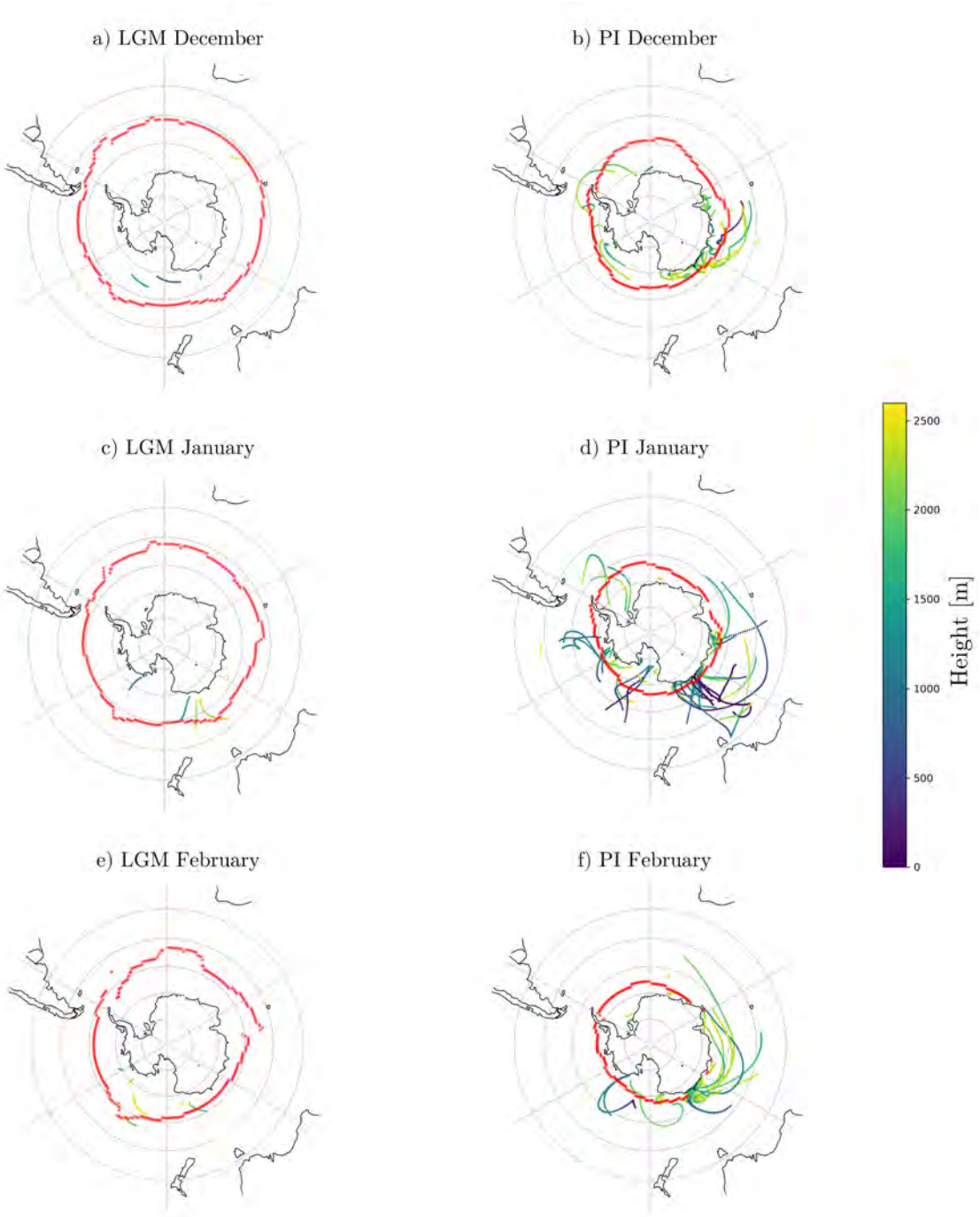

Figure 4.26: Input points for wet deposition for December (a and b), January (c and d), and February (e and f) in the LGM and PI. The red line represents the 50% sea ice cover.

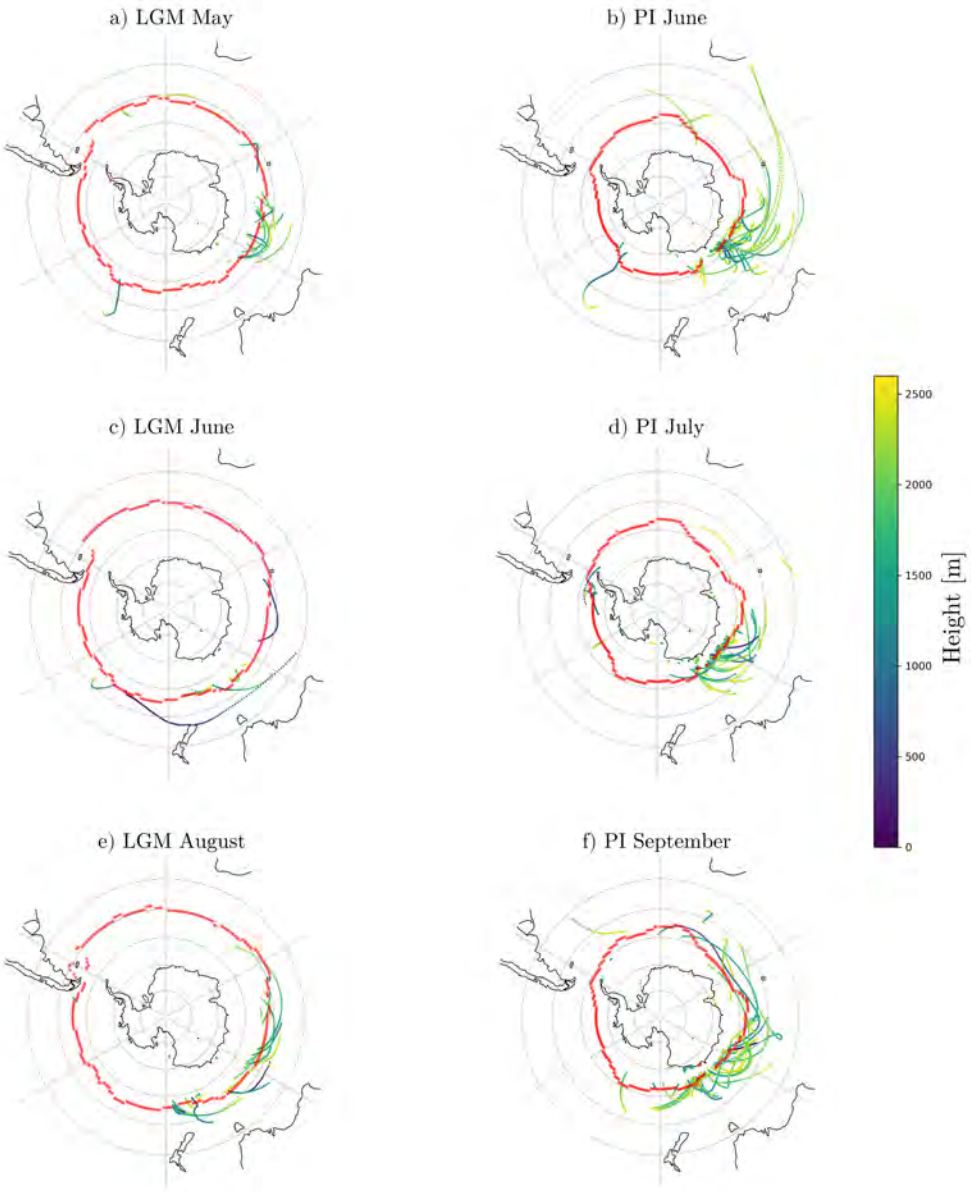

Figure 4.27: Input points for wet deposition for the corresponding months of May in the LGM (a) and June in the PI (b), June in the LGM (c) and July in the PI (d), and August in the LGM (e) and September in the PI (f). The first and last two months show a peak in the annual cycle, while the middle two show a dip in starting points, and a and b, as well as c and d, and e and f, can be equated as the same seasons due to the seasonal shift from LGM to PI. The red line represents the 50% sea ice cover.

times.

4.4.2 Impact of large-scale circulation patterns

The trajectories' differences and similarities pointed out in Section 4.4.1 are related to the underlying atmospheric circulation. In the following, we investigate the pressure fields and try to link them to the resulting trajectories.

Since the summer peaks in the LGM are even more prevalent than in the PI, as discussed for Figure 4.21, we analyze sea level pressure patterns in January and February, for both the LGM and the PI in Figure 4.28. The patterns in the single months (Figure 4.28a, b, d, and e) are all similar, although a large-scale lower pressure over the whole area in the PI months is visible in plots d and e compared to the LGM. The plots displaying the differences between January and February sea level pressure, Figure 4.28c and f, show slightly reduced pressure gradients between Antarctica and the surrounding Southern Ocean, and between the coastal regions of the Southern Ocean and the Southern Ocean at around 50°S. This is more pronounced in the LGM, and present nearly all around Antarctica, while the pressure change over Antarctica and the coastal Southern Ocean between January and February is weaker in the PI, and the reduction is only visible in the region between South America, over the south of Africa, to the coast off Dome C. In both LGM and PI Januaries, in the regions between the relative high and low-pressure systems, the reduced gradient leads to weaker westerly winds, allowing them to change directions more easily, and enabling more trajectories from further north to break through the usually strong winds. In Region 3, a relative high-pressure anomaly is found in January, which leads to winds coming from the east changing southward toward Dome C.

To quantify the large-scale pressure differences between the LGM and the PI, the sea level pressures of a summer and a winter month are analyzed separately (Figure 4.29). In both January and June, the mean pressure difference between LGM and PI is around 15 hPa. The higher pressure in the LGM is related to the colder temperatures, leading to denser air, and thus higher pressure. Besides the overall large pressure anomaly, the differences in January display a dipole, with a regional low in the Southern Pacific and over Antarctica,

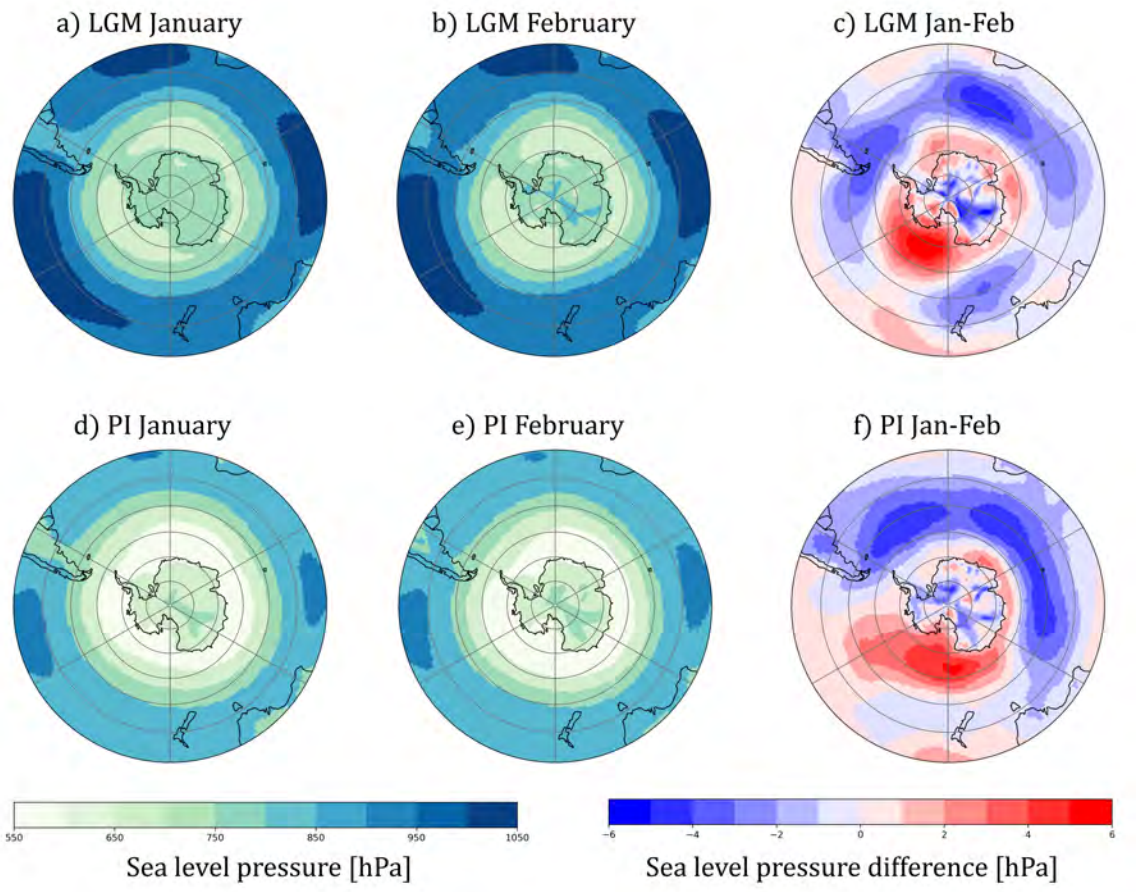

Figure 4.28: Mean sea level pressure in January and February, and their differences in the LGM (a to c) and the PI (d to f).

and a regional high in the Australian sector (cf. 4.29c). In June, a weak wave pattern anomaly is present in the Southern Ocean, with three relative low-pressure regions, while the pressure over the continent stays constant for the two time periods (cf. Figure 4.29f). However, no continuous pattern anomalies exist during the whole year, therefore an overall change in pressure patterns that could cause the strong increase in sea salt aerosols in the LGM compared to the PI is not found.

For a more trajectory-specific analysis of the pressure patterns, we look at the mean pressure fields at the time of deposition, dependent on which region the trajectories originate. This strategy only works for the dry deposition trajectories, since there are so few wet deposited

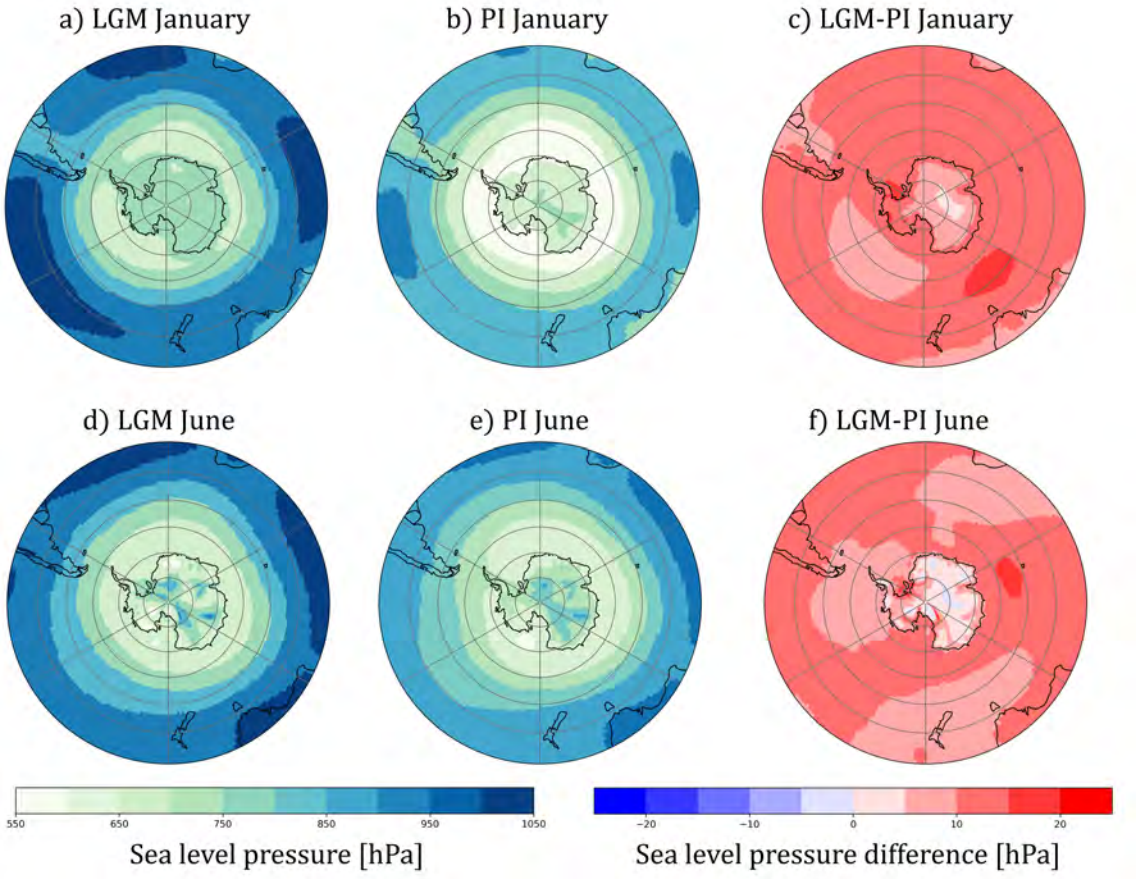

Figure 4.29: Mean sea level pressure of January and June in the LGM (a and d), PI (b and e), and their differences (c and f).

SSAs, that they merely show pressure fields corresponding to the pressure of the monthly mean pressure rather than the specific pressure of input points. As shown in Section 4.4.1, the impact of wet deposition at Dome C is negligible, and thus an analysis of only dry deposition is sufficient to study the impact of the mean atmospheric circulation. The dry deposition points are plentiful enough that we can take the mean of all input points' pressure fields per region and month, and subtract the monthly mean pressure field from that, to get the specific pattern of input points. For June (Figure 4.30), all regions exhibit relatively low pressure over East Antarctica, strengthening the low over the continent, but the low is least pronounced for trajectories in Region 3 in both the LGM and PI.

This low over East Antarctica, together with a small increase in pressure in the Ross Sea in

Figure 4.30a, c, d and f, leads air masses along the pressure lines to Dome C, thus resulting in sea salt aerosol deposition over the station.

However, the method of mean pressure per region is dependent on the month. In January (cf. Figure 4.31), for example, the large number of input points more or less cancel any patterns that might exist here. This implies that it is not just lower pressures that lead to trajectories being carried to Dome C, but also relative high-pressure systems. This is shown in Figure 4.31d, where the mean low-pressure region over Antarctica is increased by a few hPa, inducing anti-clockwise geostrophic winds around the high, and thereby transporting SSAs to Dome C. The annual mean of pressure per region (cf. Appendix Figure 7.4) shows that a relative high over Antarctica is the prevalent pressure pattern in most months, but even more so in the LGM than in the PI. This emphasizes that no singular pressure patterns prevailing over Antarctica are responsible for carrying sea salt aerosols to Dome C, but that the sea level pressure patterns at the time of deposition are diverse for each region.

Also, although the anomalies in Figures 4.30 and 4.31 are small, they do display a pattern and not a random signal. This is shown in Figures 4.32 and 4.33, which depicts surface pressure in LGM and PI June at the time of deposition and two and four days before the deposition. The patterns are strongest for the time at which the trajectories reach Dome C, while with increasing time before deposition, the pressure anomalies weaken, and are thus more equilibrated. This makes sense, the trajectories have different lengths of time to reach Dome C from their source regions, and the points before deposition do not necessarily signify any common positions between trajectories. Different pressure patterns likely lead to different trajectory routes that could not be resolved in the very coarse distinction between source regions.

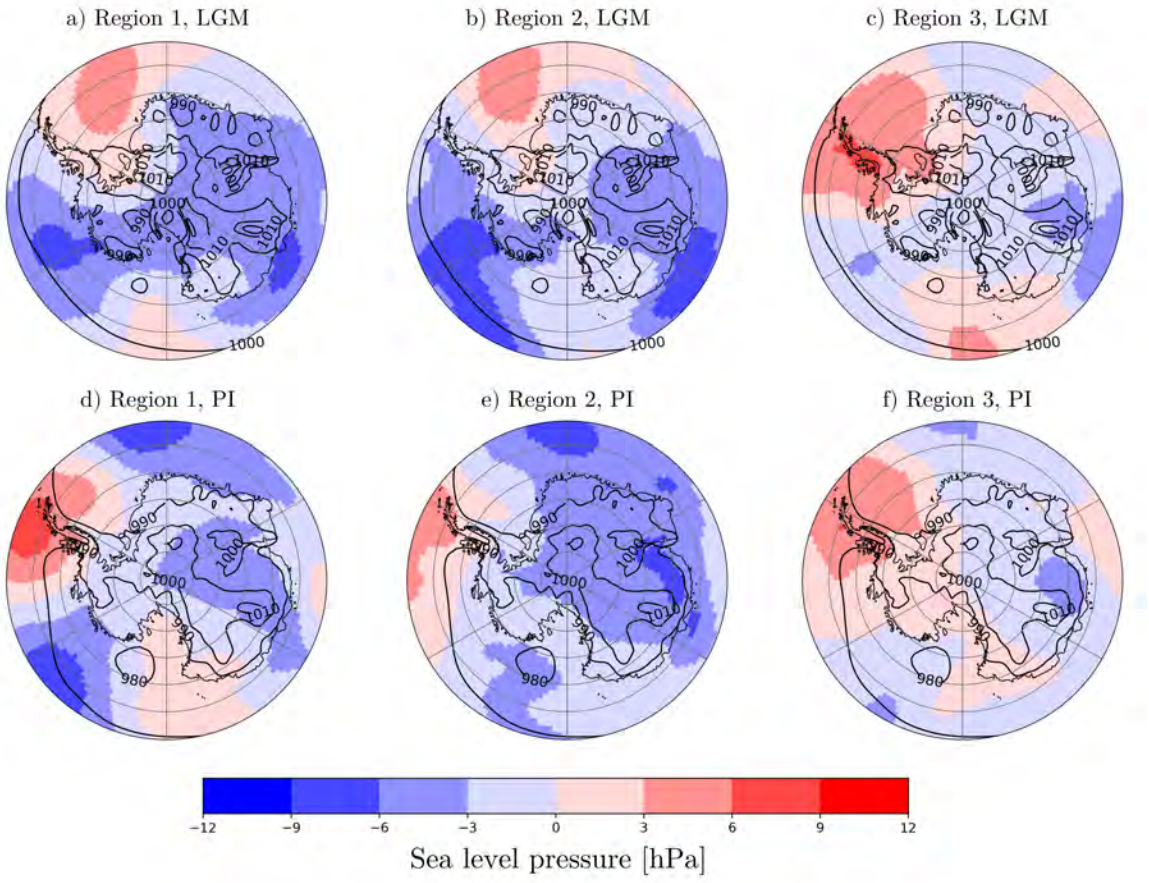

Figure 4.30: Mean sea level pressure in June from each time step that a sea salt aerosol is deposited in Dome C, split by the region in which aerosols can be taken up, minus June's mean sea level pressure field, for LGM (a to c) and PI (d to f). Contoured in black is the monthly mean pressure that was subtracted.

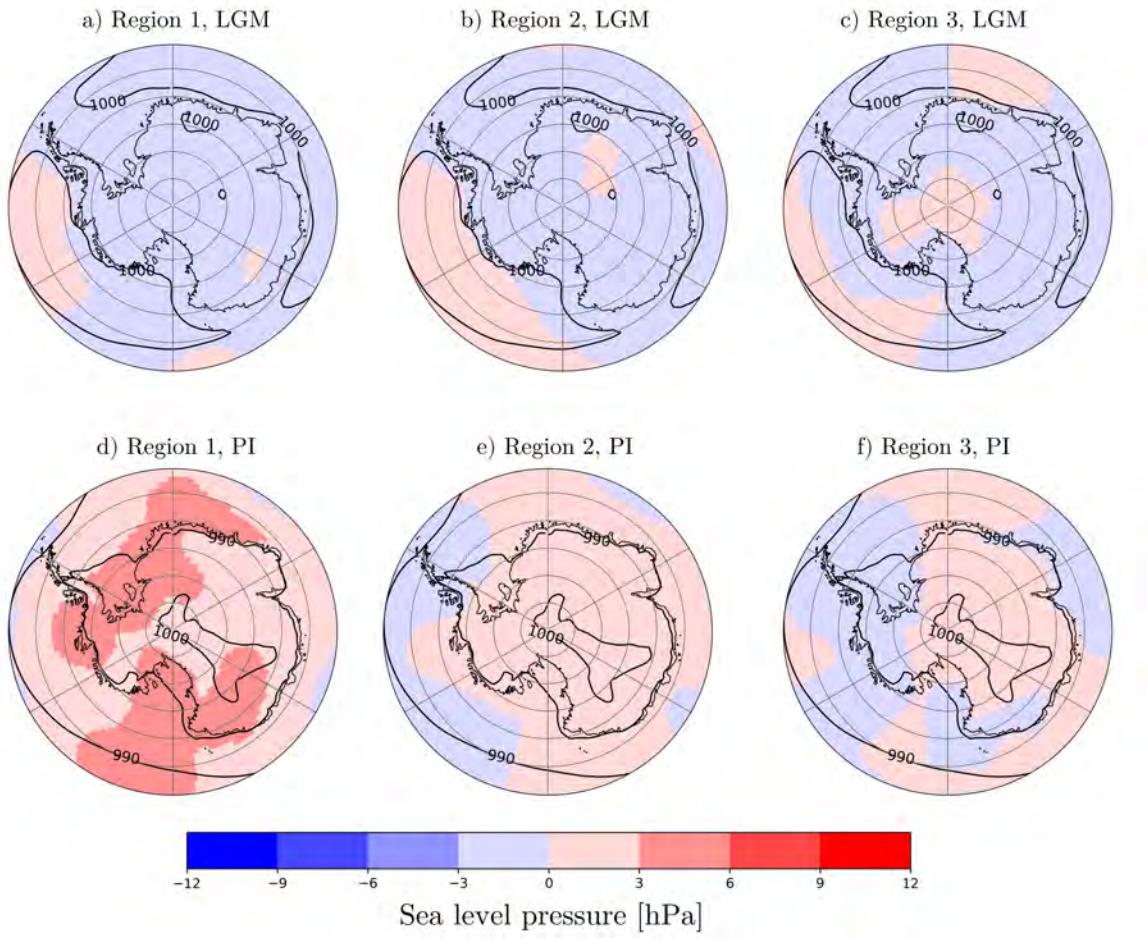

Figure 4.31: Mean sea level pressure in January from each time step that a sea salt aerosol is deposited in Dome C, split by the region in which aerosols can be taken up, and subsequently subtracted by January's mean sea level pressure field, for LGM (a to c) and PI (d to f). Contoured in black is the monthly mean pressure that was subtracted.

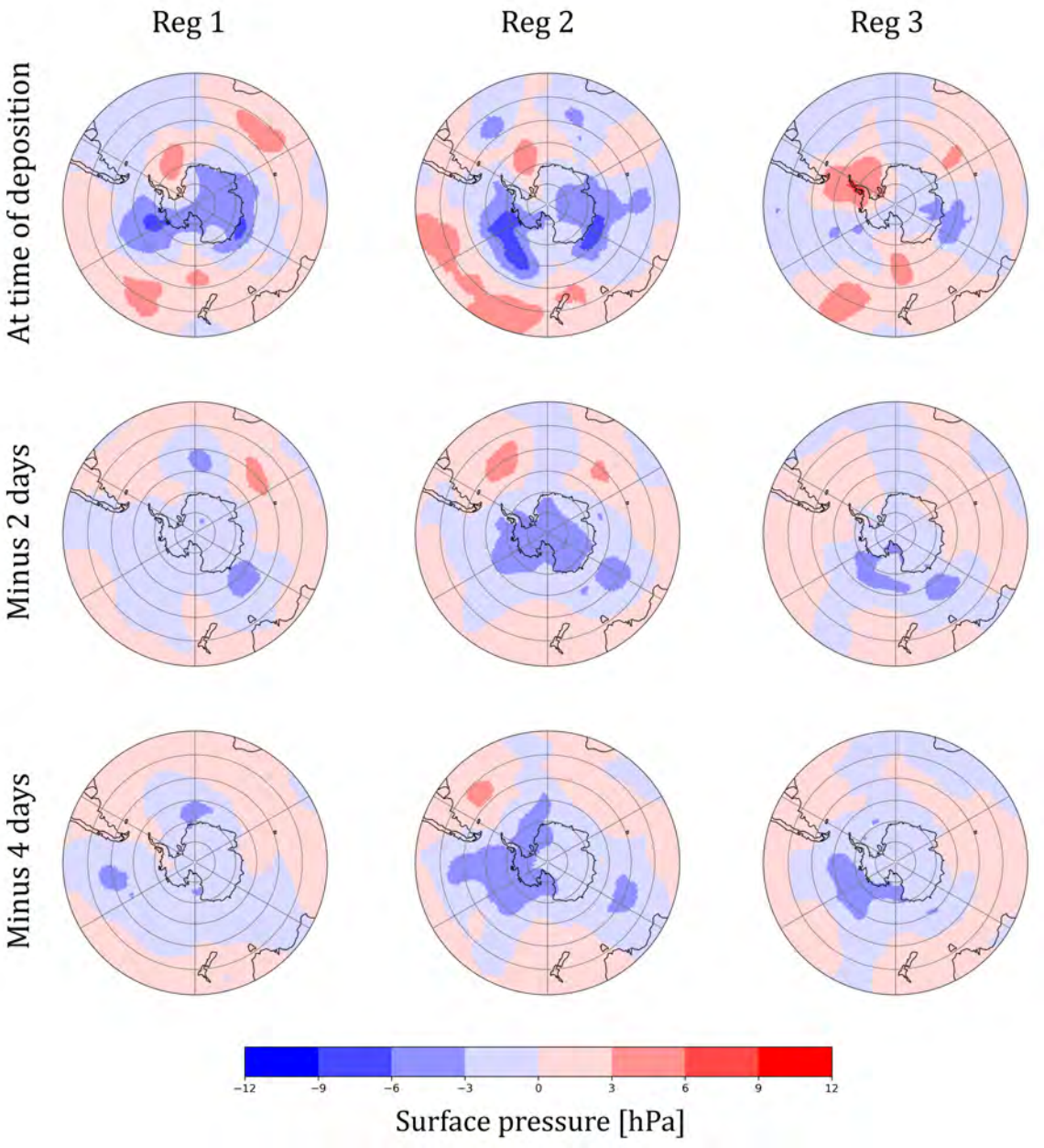

Figure 4.32: Mean sea level pressure in LGM Junes from each time step at the time of deposition, and 2, and 4 days before the deposition, split by the region in which aerosols can be taken up, minus June's mean sea level pressure field.

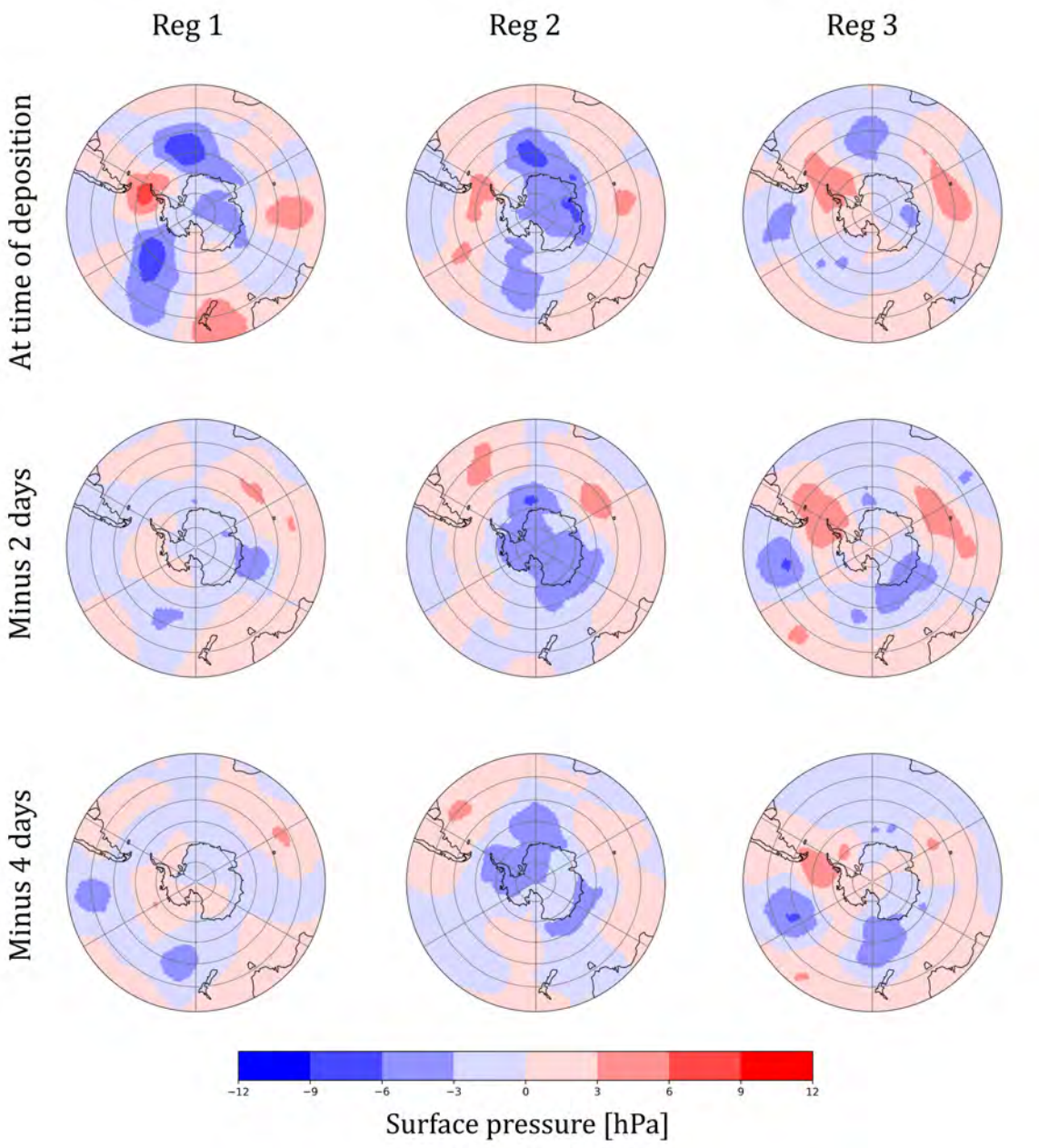

Figure 4.33: Mean sea level pressure in PI Junes from each time step at the time of deposition, and 2, and 4 days before the deposition, split by the region in which aerosols can be taken up, minus June's mean sea level pressure field.

Chapter 5

Discussion

In this chapter, we will recapitulate the most important findings. Then, we discuss their implications and agreement with existing literature.

As a conclusion of the sensitivity analysis that was performed with trajectories calculated over 10 years from ERA5 hourly data, and on a $1^\circ \times 1^\circ$ horizontal resolution, we chose the threshold that leaves the most remaining trajectories in every case. For the local wet deposition criterion at Dome C, the tested thresholds were 0.01, 0.02, and 0.04 mm hour^{-1}, which showed high sensitivity of trajectories, and led to the threshold of 0.01 mm hour^{-1} being chosen, because of its consistency with customary meteorologic precipitation thresholds. For the transport criterion, instead of hourly precipitation data which left nearly no trajectories, cumulative thresholds over 24 hours, namely 0.5, 1, and 3 mm day^{-1} were tested, resulting in a strong difference in the number of left-over trajectories, and a final threshold of 3 mm day^{-1}. The input height of aerosols was restricted by the input height criterion, where sensitivity was checked for 1,000, 1,500, 2,000, and 2,500 m, which showed less sensitivity in the number of trajectories than the previous criteria, and where 2500 m was chosen for trajectory filtering. The formation of aerosols revealed only small differences between the thresholds of 4 and 3 m s^{-1}, and no formation criterion, leading to the omission of this criterion. The trajectories' end heights of 50, 500, and 1,500 m, exhibited a low sensibility in the number of trajectories per height but revealed that 50-m-trajectories travel longer distances, and thereby have more input points. Since aerosols can be deposited from any height, we used all end heights. Besides

the fact that the least restrictive thresholds left more trajectories to be analyzed, the choice of thresholds is also justified by the rather low resolution of the input data in CESM1.2, whereby all data points describe conditions in a 1°×1° grid cell and are not representative for the small air parcel carrying the aerosols.

The impact of temporal resolution on trajectories is found to be comparably small, with an overall good representation of trajectories in the lower resolution of 6 hours compared to 1-hourly resolution. The lower temporal resolution does, however, lead to a loss of about 19% of total sea salt aerosol trajectories after filtering, but the composition of source regions stays similar. In summer, the spatial resolution of 1°×1° produces trajectories that are very similar to the 0.25°×0.25° trajectories in both amount and pattern, but in winter, the representation of trajectories in the low resolution substantially deviates from the high resolution, since the low-resolution results in nearly three times the number of trajectories compared to the higher resolution. Note that the analysis was carried out on only one summer and winter month each, so the interpretation is difficult. An analysis of several seasons might result in a more coherent interpretation.

Compared to ERA5, CESM1.2 represents both the amount and the annual distribution of trajectories well, except for the summer peak which, though present in ERA5 as well, is much more prominent in CESM1.2. This has been attributed to a reduced gradient in pressure from Antarctica to the circumpolar trough, leading to weaker zonal winds around the continent, which allow for trajectories from further north to penetrate through the usually strong winds more often and deposit aerosols at Dome C. This summer peak shows up mostly in dry deposition, where ERA5 and CESM1.2 both also display a smaller peak in autumn and spring.

Wet deposition, on the other hand, is highest in winter, and lowest in summer in both reanalysis and model, corresponding to the yearly precipitation pattern in CESM1.2. The two datasets agree less on the origins of sea salt aerosols, which is important for this study. While Region 1, the highest contributing region, matches between ERA5 and CESM1.2, Region 2 is slightly underestimated in CESM1.2 but has the same seasonal cycle as in ERA5, and Region 3 is severely overestimated, as in ERA5 almost no trajectories come from this region

while CESM1.2 shows an input from Region 3 that is nearly as high as input from Region 1. Any CESM1.2 results depicting large contributions from Region 3 should thus be viewed with caution.

Comparing sea salt aerosols in the LGM and the PI, mean LGM trajectories are longer than trajectories in the PI. This is expected in a drier climate where less *en route* washing-out of the aerosols takes place [*Levine et al.*, 2014].

Aside from the shift of one month between the LGM and PI due to changes in orbital parameters, the seasonality of dry deposition is similar for the two time periods, but more pronounced and stronger in the LGM, with the summer peak, and smaller peaks in autumn and spring. Wet deposition, on the other hand, is more prevalent in the PI, but the PI peaks in June and September correlate with the LGM peaks in May and August. However, the January peak that is visible in all other CESM1.2 runs is not present in LGM wet deposition, which is likely due to too few wet trajectories being deposited over Dome C in the LGM. The summer peak observed in our study is supported by some studies over the Antarctic continent, while others found a different annual cycle. *Weller and Wagenbach* [2007] and *Jourdain et al.* [2008] measured atmospheric SSA particles in continental Antarctica in 2006, and found peaks in winter, citing the large sea ice contribution as a source process. However, *Weller et al.* [2011] reported a high SSA load in summer at Dumont d'Urville Station, and *Hall and Wolff* [1998] at Halley Station, which they attribute to the smaller sea ice extent in summer. Dumont d'Urville and Halley are coastal stations, while *Jourdain et al.* [2008] and *Weller and Wagenbach* [2007] conducted their study in stations on the Antarctic Plateau, meaning our results should agree with the studies performed at inland stations over the coastal regions. However, both *Weller and Wagenbach* [2007] and *Jourdain et al.* [2008] cover aerosol sampling for only one winter each in low resolution, so the seasonality of sea salt aerosol concentration over the Antarctic plateau is not very well studied yet. Additionally, it is not only CESM1.2 that shows the peak in summer but also the reanalysis ERA5, even if the peak is less pronounced there. Moreover, *Levine et al.* [2014] suggested that the annual variability of aerosol concentration is influenced more by weather and meteorology than by sea ice extent. In winter, circumpolar zonal wind speeds are generally higher than in summer, leading to less

meridional variation which makes it less likely for trajectories coming from lower latitudes to get into the circumpolar jet or escape it and to enter the Antarctic continent. Thus, it makes sense meteorologically that more trajectories arrive at Dome C in summer. *Jourdain et al.* [2008] and *Legrand et al.* [2017] also noted that the observed winter peak consists of more large sea salt aerosols than during the rest of the year, which contribute comparably more sea salt mass than smaller particles. This could be a mechanism that leads to a peak in sea salt aerosol concentration at the deposition location despite the peak in trajectories occurring in a different season.

In the LGM, the highest sea salt aerosol contribution comes from sea ice (63%), especially in summer, where the area of sea ice between 50% and 90% is especially large. The summer SISS aerosols are mostly from regions off the coast of East Antarctica, or from the Ross Sea, which falls in Region 3 and is likely overestimated, while OOSS come from all around Antarctica, but especially from south of Australia. In the other seasons, both SISS and OOSS originate from all around Antarctica, but have a peak originating off the East Antarctic coast. While the total input of SSAs from sea ice cover over 50% is 63% in the LGM, it is only 35% in the PI, where SISS aerosols only originate from very close to Antarctica's coast, mostly from off the East Antarctic coast. This supports the hypothesis of *Legrand et al.* [2017] that the contribution of sea ice aerosols increases in glacial times as opposed to present day. The largest OOSS input is in summer, and from all around Antarctica, although the largest contribution comes from between Dome C and Australia. The LGM wet deposition constitutes only 2% of the total amount of LGM trajectories and is negligible, but in the PI, wet-deposited trajectories comprise 10% of the total trajectory number and mostly carry OOSS aerosols from the East Antarctic coast that start close to the sea ice line. Nonetheless, the fact that in winter, sea ice and open ocean contribute aerosols in approximately equal parts, as shown by *Legrand et al.* [2017], holds true for both the PI and LGM, even though the overall ratio of sea ice and open ocean are very different for the two periods.

Besides the average LGM trajectory being 205 km longer for dry deposition and 275 km longer for wet deposition, the overall number of trajectories in the LGM is also higher ($\#_{traj}(LGM)$ = 27,962 and $\#_{traj}(PI)$ =22,686), and the number of input points in the

LGM is nearly twice as high as in the PI ($\#_{input}(LGM)$ =159,447 and $\#_{input}(PI)$ =82,243). This is supported by *Albani et al.* [2018], who showed an increase in sea salt emission in high latitudes during the LGM. *Schüpbach et al.* [2018] showed that in the Northern Hemisphere, SSA emissions are enhanced by 50% only, which they attribute to sea ice expansion, but this plays less of a role in Antarctica because the sea ice extent decreases to a near-PI extent in austral summer, which is when most SSAs are emitted.

Aerosol concentration in the ice is proportional to $A\epsilon+v_{dry}$, with A denoting the accumulation, ϵ the scavenging rate, and v_{dry} the dry deposition. Scavenging rate and dry deposition depend on the aerosol species and are given by *Schüpbach et al.* [2018] for sea salt aerosols with ϵ =2,000±800 g_{air} g_{snow}^{-1} and v_{dry} =4.1±2.2 m hr^{-1}. With the mean PI accumulation of 2.5 cm yr^{-1}, this gives a wet deposition velocity of 5,000±2,000 cm yr^{-1}, and dry deposition velocity of $4\times10^6\pm2\times10^6$ cm yr^{-1}, resulting in a factor of about 1 to 1,000 for the input of wet to dry deposition. Here, the wet deposition velocity encompasses separate snow events over the year that amass to the total wet deposition velocity, while the dry deposition occurs constantly. This suggests that the difference between the two is significantly larger than anticipated from our number of trajectories or input points, and confirms that the contribution of wet deposition is negligible for the total flux of SSA.

Assuming that both atmospheric SSA concentration and the deposition rate are considered in the amount of sea salt aerosols taken up by trajectories that can deposit them over Dome C, and that the atmospheric load of SSA depends on the number of input points, i.e., possibilities for air parcels to take up SSAs, the input points are proportional to the sea salt fluxes at Dome C, as shown in Equation 2.5. Given that the wet deposition contribution is significantly smaller than the dry deposition, we will only consider the amount of dry deposition input points, given by $\#_{input}(LGM)$ =155925 and $\#_{input}(PI)$ =74051, resulting in a LGM SSA flux which is two times higher than the PI flux, matching with the fluxes at Dome C calculated by *Fischer et al.* [2007] that are 2 to 3 times higher during the LGM than today. For the calculation of sea salt concentration in ice, we need to divide the input points by the accumulation rates (cf. Equation 2.5), which are A_{PI} =2.5 cm yr^{-1} and A_{LGM} =1.5 cm yr^{-1}. This shows that the amount of sea salt aerosols deposited in the ice in the Preindustrial

are 28% of the concentration deposited during the Last Glacial Maximum. This scale of magnitude compares well with the measurements in Dome C ice cores, where the ratio of the concentration of SSA in LGM ice, compared to the Holocene is approximately 5 [*Fischer et al.*, 2007].

Jourdain et al. [2008] suggested a connection between local low pressure and peaks in atmospheric sea salt aerosols which we can see in singular months (e.g., June) but not in a general pressure pattern. This might again be attributable to *Jourdain et al.* [2008] analyzing the mass of atmospheric aerosols, while we look at the number of input points. We do see a definite correlation between pressure and properties of trajectories, as the strength of the summer peak can be attributed to an increase of pressure in the circumpolar trough around Antarctica and a reduction of Southern Ocean pressure. This leads to a lower gradient and less intense westerly winds that allow more meridional exchange of air masses and make it possible for trajectories from mid-latitudes to reach Dome C. The same effect on trajectories is visible during the Last Glacial Maximum, as pressure over the Southern Ocean increases and weakens the overall meridional gradient between Antarctica and the Southern Ocean, reducing geostrophic wind speeds all around the continent.

Chapter 6

Conclusion and outlook

In this study, we analyzed the pathways of air parcels and the aerosols' source regions by calculating back-trajectories using the FLEXTRA trajectory method. We compared the trajectories and source regions for the preindustrial period and the Last Glacial Maximum, with model data from CESM1.2, and validated the accuracy of the data and studied temporal and spatial resolution impact with the reanalysis ERA5. The main findings are that an increase in temporal resolution from 1-hourly to 6-hourly data produces 23% more trajectories than the lower resolution. However, a change in spatial resolution from 1°×1° to 0.25°×0.25° is found to have very little impact on trajectories. The summer peak in the number of trajectories and input points is increased for CESM1.2 data but also appears in ERA5. The peak is caused by a lower meridional pressure gradient, an accompanying lower geostrophic wind speed, and a large area covered by 50 to 90% sea ice. While wet deposition is shown to contribute little sea salt to Dome C in the PI, with 10% of total deposition, this is even more pronounced in the LGM, with only 2% wet deposition. The total sea salt aerosol flux in the PI, calculated from the number of input points, is only at 47% of the flux in the LGM, and the corresponding sea salt concentration in the ice is about 4 times smaller in the PI than in the LGM. Both are due to the higher precipitation rate in the Holocene. Sea ice contributes by nearly two-thirds of the total input points in the LGM, as opposed to one-third in the PI. The main sea ice source region stretches from the Ross Sea to the Amery Ice Shelf, with the area being confined close to the coast in the PI, and reaching until 50°S

off the East Antarctic coast in the LGM. The open ocean aerosols largely originate from the Southern Ocean between Antarctica and Australia, with smaller source regions all around the Antarctic continent.

For future research, a more in-depth study of the seasonal variation and the development of a tool to estimate the aerosol amount per trajectory would help in explaining the difference in annual patterns between on-site measurements at the site and our modeling-based approach. To obtain more specific source regions, it would be interesting to apply a cluster analysis to the trajectories, that takes into account the pathways of trajectories, the number of input points per trajectory, or the cumulative precipitation along the way, and subsequently analyze the atmospheric circulation patterns associated to the clusters, to better understand the underlying processes of the trajectories.

Additionally, this analysis could benefit from using CESM2 data, where a mushy layer is implemented on sea ice that represents the mixture of sea ice and salty water necessary for sea ice aerosol production which would prove helpful in identifying the amount of sea ice aerosols taken up by trajectories.

Chapter 7

Appendix

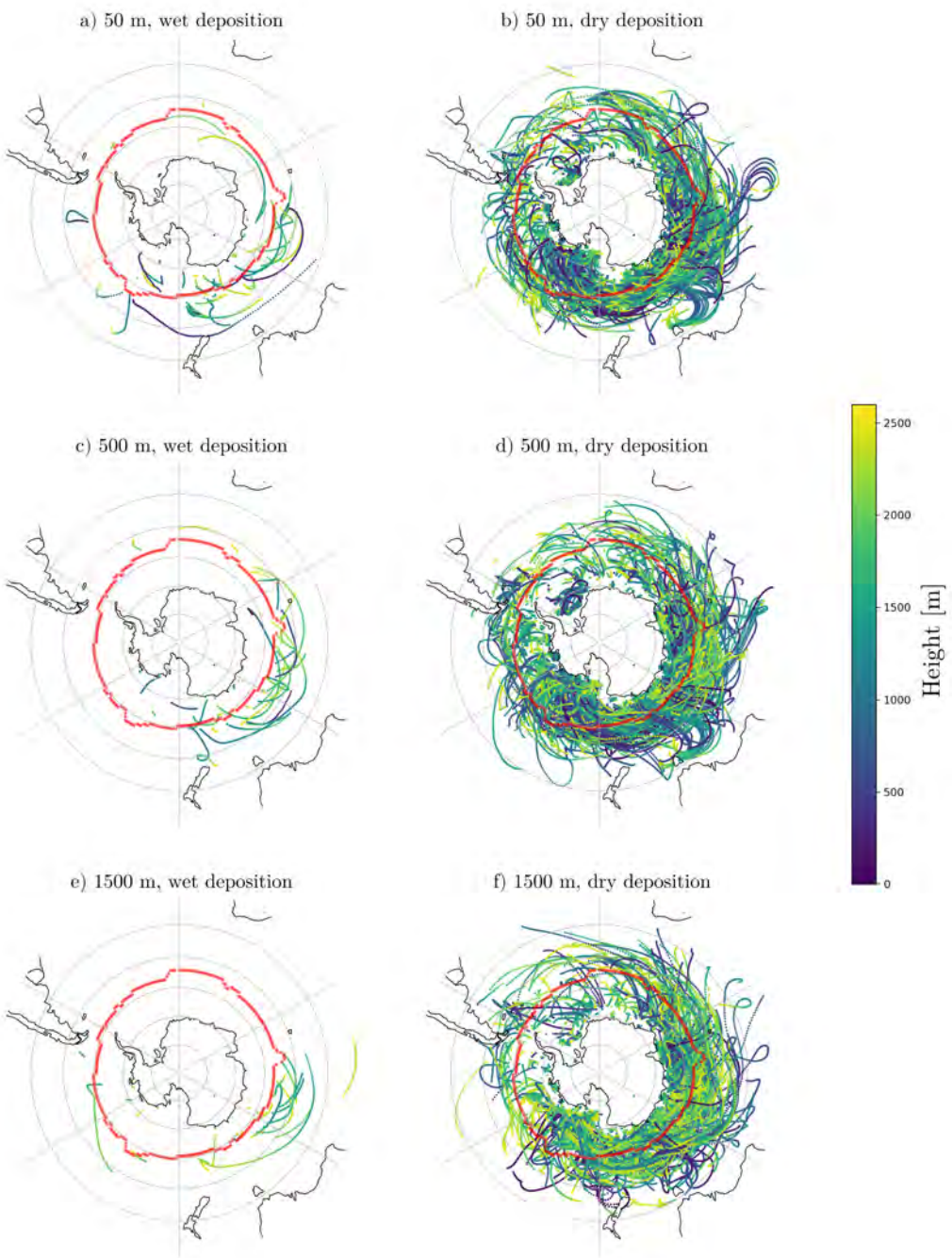

Figure 7.1: Input points for the different end heights over Dome C of 50 m (a and b), 500 m (c and d), and 1,500 m (e and f) for wet and dry deposition in the LGM. The shading shows the height of trajectories at the input point, while the red line shows sea ice cover of 50%.

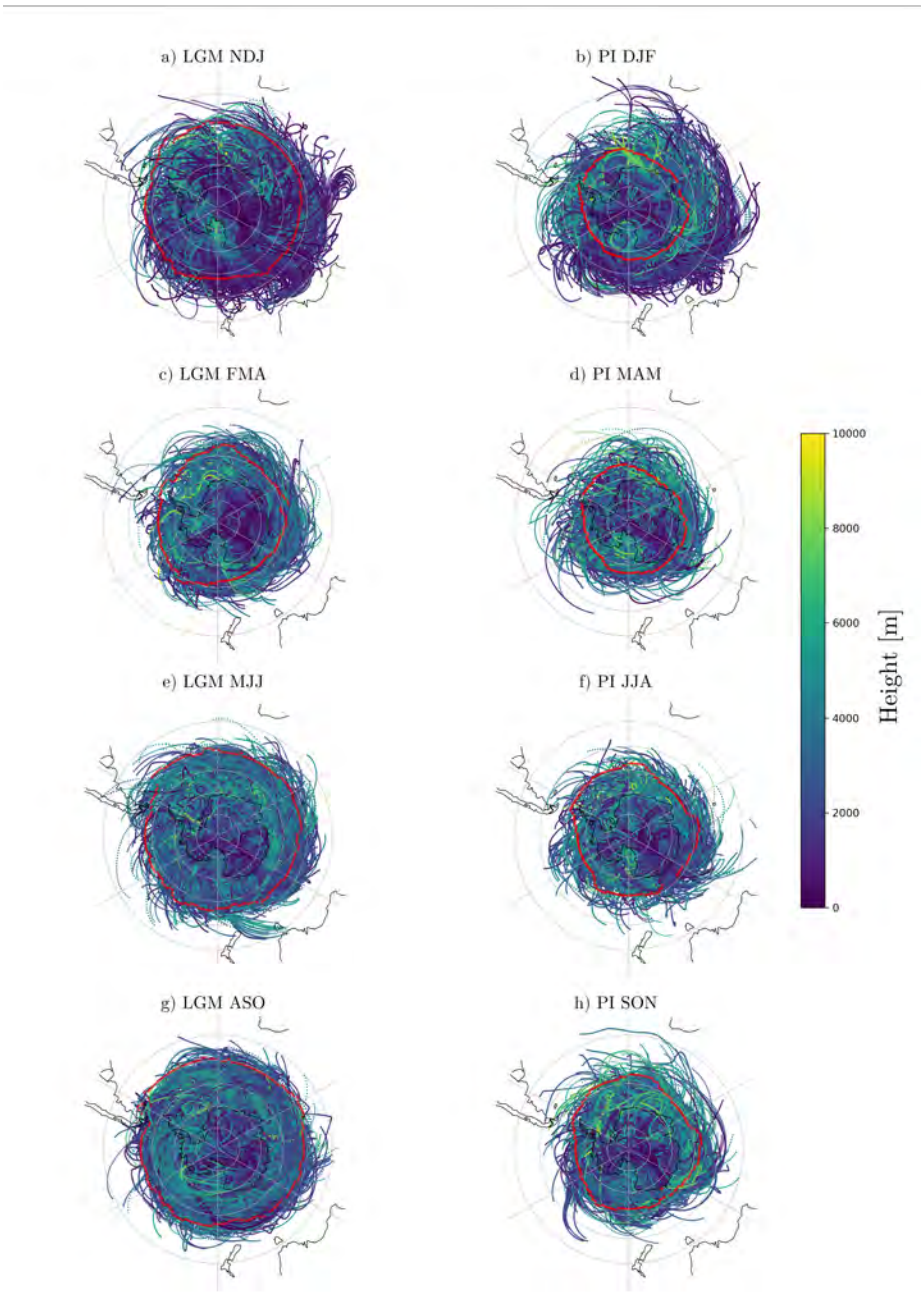

Figure 7.2: Input points of dry deposition for LGM and PI. The LGM seasons are shifted by one month so that they correspond to the maximal summer and winter seasons. The red line depicts a sea ice cover of 50 %, and the shading shows the height of trajectories at the input points.

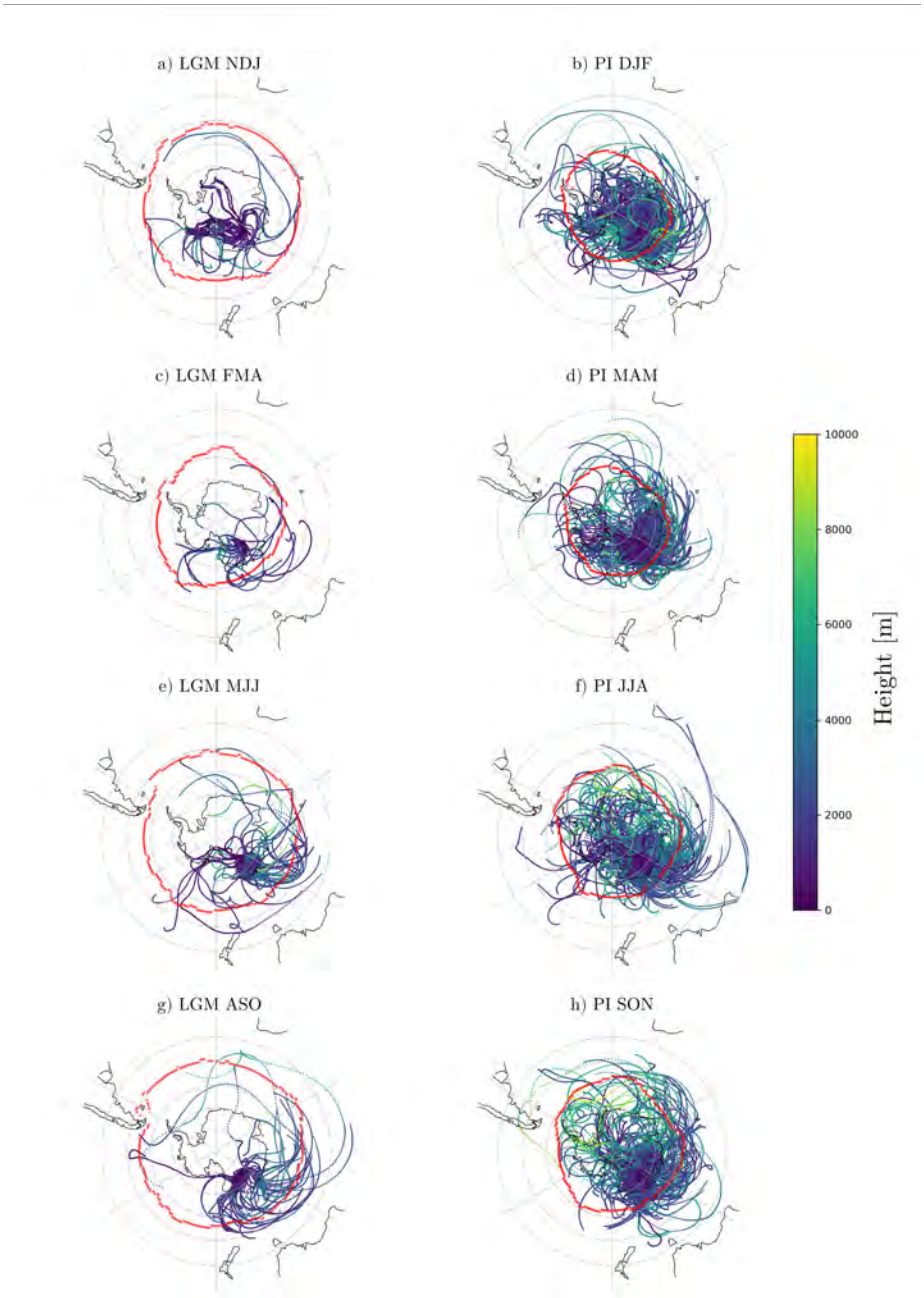

Figure 7.3: Input points of wet deposition for LGM and PI. The LGM seasons are shifted by one month so that they correspond to the maximal summer and winter seasons. The red line depicts a sea ice cover of 50 %, and the shading shows the height of trajectories at the input points.

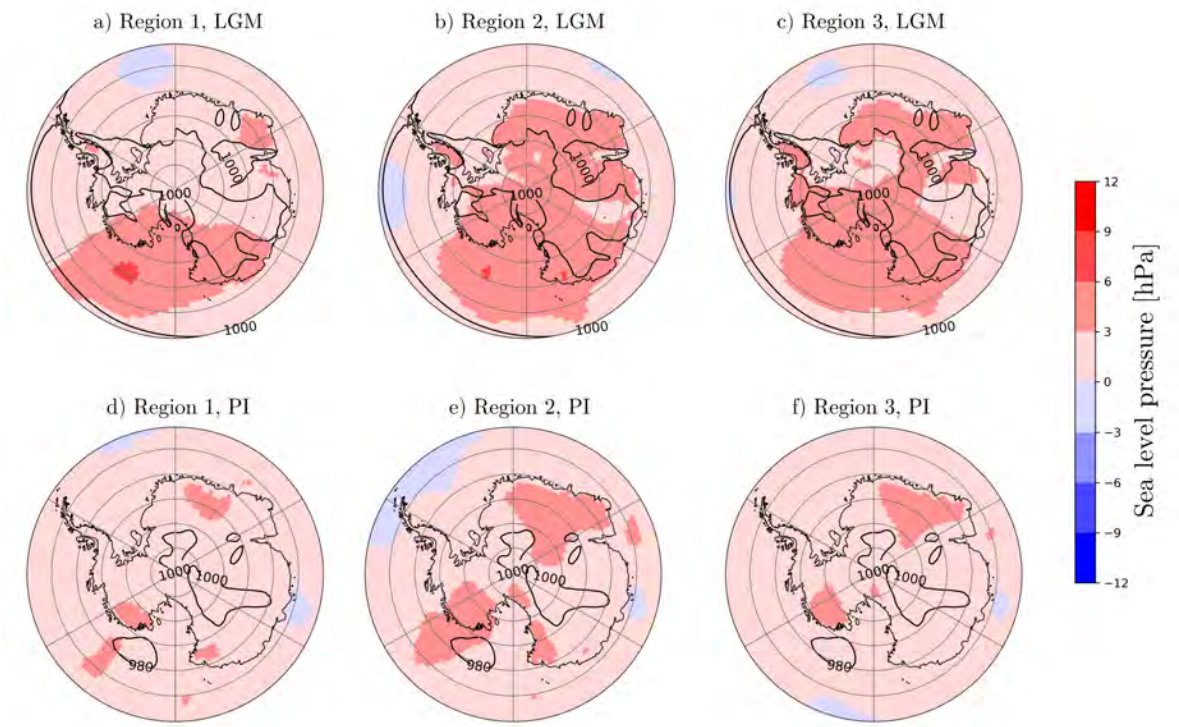

Figure 7.4: Mean annual surface pressure from each time step that a sea salt aerosol is deposited in Dome C, split by the region in which aerosols can be taken up, taken from each month, and subsequently subtracted by each month's mean surface pressure field, for LGM (a to c) and PI (d to f). Contoured in cyan is the monthly mean pressure that was subtracted.

Acknowledgements

I would like to thank Christoph Raible for his ideas, feedback, input, and motivational pushes during the time of my Master thesis, and for helping me understand every last parameter (well, probably not all) that plays into atmospheric circulation and its interactions with the cryosphere. A big thank you goes to Martina Messmer for being there for any coding and climate-related questions I had and for supporting me with structuring my work and considering my well-being. My time at KUP was made more enjoyable by my office colleagues Santos Gonzalez and Onno Doensen with small laughter breaks in between which I am very grateful for. On top of that, I want to thank Jonathan Buzan for the CESM1.2 runs, explanations and plots, and excellent book recommendations when I needed to take my mind off the thesis. Furthermore, I very much appreciated Hubertus Fischer for his co-supervision and feedback. And, finally, many thanks go out to my friends and family for emotional support, proofreading, and forcing me to go outside or play a round of Tichu.

Bibliography

Albani, S., Y. Balkanski, N. Mahowald, G. Winckler, V. Maggi, and B. Delmonte, Aerosol-climate interactions during the Last Glacial Maximum, *Current Climate Change Reports, 4*, 99–114, 2018.

Bannister, R., *Elementary 4D-VAR, DARC Technical Report No. 2*, University of Reading, UK, Reading, UK, 2001/2007.

Barber, J., G. Thomas, G. Kerstiens, and K. Jones, Current issues and uncertainties in the measurement and modelling of air-vegetation exchange and within-plant processing of POPs, *Environmental pollution (Barking, Essex : 1987), 128*, 99–138, 2004.

Bian, H., K. Froyd, D. M. Murphy, J. Dibb, A. Darmenov, M. Chin, P. R. Colarco, A. da Silva, T. L. Kucsera, G. Schill, H. Yu, P. Bui, M. Dollner, B. Weinzierl, and A. Smirnov, Observationally constrained analysis of sea salt aerosol in the marine atmosphere, *Atmospheric Chemistry and Physics, 19*, 10773–10785, 2019.

Bluestein, H., *Synoptic-dynamic meteorology in midlatitudes: Volume 1, principles of kinematics and dynamics*, Volume 1, Oxford University Press, Oxford, England, 1992.

British Antarctic Survey, 2015, Landsat Image Mosaic Of Antarctica (LIMA), Online at https://lima.usgs.gov/download.php; accessed 24-February-2023.

Buzan, J., E. Russo, W. M. Kim, and C. Raible, Winter sensitivity of glacial states to orbits and ice sheet heights in CESM1.2, *EGUsphere, submitted*, 1–30, 2023.

Cao, J., B. Wang, and J. Liu, Attribution of the Last Glacial Maximum climate formation, *Climate Dynamics, 53*, 1661–1679, 2019.

Carslaw, K. S., Chapter 5 - Aerosol processes, in *Aerosols and Climate*, edited by K. S. Carslaw, pp. 135–185, Elsevier, 2022.

Casado, M., A. Landais, G. Picard, T. Münch, T. Laepple, B. Stenni, G. Dreossi, A. Ekaykin, L. Arnaud, C. Genthon, A. Touzeau, V. Masson-Delmotte, and J. Jouzel, Archival processes of the water stable isotope signal in East Antarctic ice cores, *The Cryosphere, 12*, 1745–1766, 2018.

Caton Harrison, T., S. Biri, T. J. Bracegirdle, J. C. King, E. C. Kent, E. Vignon, and J. Turner, Reanalysis representation of low-level winds in the Antarctic near-coastal region, *EGUsphere, 3*, 1–42, 2022.

Cherrier, G., E. Belut, F. Gerardin, A. Tanière, and N. Rimbert, Aerosol particles scavenging by a droplet: Microphysical modeling in the Greenfield gap, *Atmospheric Environment, 166*, 519–530, 2017.

Chow, F. K., C. Schär, N. Ban, K. A. Lundquist, L. Schlemmer, and X. Shi, Crossing multiple gray zones in the transition from mesoscale to microscale simulation over complex terrain, *Atmosphere, 10*, 274, 2019.

Collins, W., P. Rasch, B. Boville, J. Hack, J. McCaa, D. Williamson, and J. Kiehl, Description of the NCAR Community Atmosphere Model (CAM 3.0), *NCAR Technical Note, TN-464+STR*, 21–72, 2004.

Cucchi, M., G. Weedon, A. Amici, N. Bellouin, S. Lange, H. Müller Schmied, H. Hersbach, and C. Buontempo, WFDE5: bias adjusted ERA5 reanalysis data for impact studies, *Earth System Science Data, 12*, 2097–2120, 2020.

Danabasoglu, G., J.-F. Lamarque, J. Bacmeister, D. Bailey, A. Duvivier, J. Edwards, L. Emmons, J. Fasullo, R. Garcia, A. Gettelman, C. Hannay, M. Holland, W. Large, P. Lauritzen, D. Lawrence, J. Lenaerts, K. Lindsay, W. Lipscomb, M. Mills, and

W. Strand, The Community Earth System Model version 2 (CESM2), *Journal of Advances in Modeling Earth Systems, 12*, e2019MS001916, 2020.

Déry, S., and M. Yau, Simulation of blowing snow in the Canadian Arctic using a double-moment model, *Boundary-Layer Meteorology, 99*, 297–316, 2001.

ECMWF, 2017, 20 years of 4D-Var: better forecasts through a better use of observations, Online at https://www.ecmwf.int/en/about/media-centre/news/2017/20-years-4d-var-better-forecasts-through-better-use-observations; accessed 2022-02-23.

Emerson, E. W., A. L. Hodshire, H. M. DeBolt, K. R. Bilsback, J. R. Pierce, G. R. McMeeking, and D. K. Farmer, Revisiting particle dry deposition and its role in radiative effect estimates, *Proceedings of the National Academy of Science, 117*, 26076–26082, 2020.

EPICA Community Members, Eight glacial cycles from an Antarctic ice core, *Nature, 429*, 623–628, 2004.

Fischer, H., M.-L. Siggaard-Andersen, U. Ruth, R. Röthlisberger, and E. Wolff, Glacial/interglacial changes in mineral dust and sea-salt records in polar ice cores: Sources, transport, and deposition, *Reviews of Geophysics, 45*, RG1002, 2007.

Fogt, R. L., and G. J. Marshall, The Southern Annular Mode: Variability, trends, and climate impacts across the Southern Hemisphere, *WIREs Climate Change, 11*, e652, 2020.

Frey, M., S. Norris, I. Brooks, P. Anderson, K. Nishimura, X. Yang, A. Jones, M. Nerentorp Mastromonaco, D. Jones, and E. Wolff, First direct observation of sea salt aerosol production from blowing snow above sea ice, *Atmospheric Chemistry and Physics Discussions, 20*, 1–53, 2019.

Glantz, P., E. Nilsson, and W. von Hoyningen-Huene, Estimating a relationship between aerosol optical thickness and surface wind speed over the ocean, *Atmospheric Research, 92*, 58–68, 2009.

Hall, J., and E. Wolff, Causes of seasonal and daily variations in aerosol sea-salt concentrations at a coastal Antarctic station, *Atmospheric Environment, 32*, 3669–3677, 1998.

Haywood, J., V. Ramaswamy, and B. Soden, Tropospheric aerosol climate forcing in clear-sky satellite observations over the oceans, *Science, 283*, 1299–1303, 1999.

Hersbach, H., B. Bell, P. Berrisford, S. Hirahara, A. Horányi, J. Muñoz Sabater, J. Nicolas, C. Peubey, R. Radu, D. Schepers, A. Simmons, C. Soci, S. Abdalla, X. Abellan, G. Balsamo, P. Bechtold, G. Biavati, J. Bidlot, M. Bonavita, and J.-N. Thépaut, The ERA5 global reanalysis, *Quarterly Journal of the Royal Meteorological Society, 146*, 1999–2049, 2020.

Hunke, E., and W. Lipscomb, CICE: The Los Alamos sea ice model documentation and software user's manual version 4.0, LA-CC-06-012, *Los Alamos National Laboratory,*, 1–115, 2010.

Hurrell, J., M. Holland, P. Gent, S. Ghan, J. Kay, P. Kushner, J.-F. Lamarque, W. Large, D. Lawrence, K. Lindsay, W. Lipscomb, M. Long, N. Mahowald, D. Marsh, R. Neale, P. Rasch, S. Vavrus, M. Vertenstein, D. Bader, and S. Marshall, The Community Earth System Model: A framework for collaborative research, *Bulletin of the American Meteorological Society, 94*, 1339–1360, 2013.

Jansen, E., J. Overpeck, K. Briffa, J.-C. Duplessy, F. Joos, V. Masson-Delmotte, D. Olago, B. Otto-Bliesner, W. Peltier, S. Rahmstorf, R. Ramesh, D. Raynaud, D. Rind, O. Solomina, R. Villalba, and D. Zhang, Palaeoclimate, in *Climate Change 2007: Synthesis Report. Contribution of Working Groups I, II and III to the Fourth Assessment Report of the Intergovernmental Panel on Climate Change*, edited by S. Solomon, D. Qin, M. Manning, Z. Chen, M. Marquis, K. Averyt, M. Tignor, and H. Miller, Book section 6, pp. 433–498, Cambridge University Press, Cambridge, United Kingdom and New York, NY, USA, 2007.

Jiangping, Z., A. Xie, X. Qin, Y. Wang, B. Xu, and Y. Wang, An assessment of ERA5 reanalysis for antarctic near-surface air temperature, *Atmosphere, 12*, 217, 2021.

Jourdain, B., S. Preunkert, O. Cerri, H. Castebrunet, R. Udisti, and M. Legrand, Year-round record of size-segregated aerosol composition in central Antarctica (Concordia station): Implications for the degree of fractionation of sea-salt particles, *Journal of Geophysical Research, 113*, 1–9, 2008.

Jouzel, J., and V. Masson-Delmotte, 2007, EPICA Dome C Ice Core 800kyr deuterium data and temperature estimates, Supplement to: J. Jouzel, V. Masson-Delmotte, O. Cattani, G. Dreyfus, S. Falourd, G. Hoffmann, B. Minster, J. Nouet, J.-M. Barnola, J. A. Chappellaz, H. Fischer, J. C. Gallet, S. J. Johnsen, M. C. Leuenberger, L. Loulergue, D. Luethi, H. Oerter, F. Parrenin, G. M. Raisbeck, D. Raynaud, A. Schilt, J. Schwander, E. Selmo, R. A. Souchez, R. Spahni, B. Stauffer, J. P. Steffensen, B. Stenni, T. F. Stocker, J.-L. Tison, M. Werner, E. W. Wolff (2007): Orbital and millennial Antarctic climate variability over the past 800,000 years. Science, 317(5839), 793-797, https://doi.org/10.1126/science.1141038.

Jouzel, J., F. Vimeux, N. Caillon, G. Delaygue, G. Hoffmann, V. Masson-Delmotte, and F. Parrenin, Magnitude of isotope/temperature scaling for interpretation of central Antarctic ice cores, *Journal of Geophysical Research: Atmospheres, 108*, JD002677, 2003.

Kageyama, M., S. Albani, P. Braconnot, S. P. Harrison, P. O. Hopcroft, R. F. Ivanovic, F. Lambert, O. Marti, W. R. Peltier, J.-Y. Peterschmitt, D. M. Roche, L. Tarasov, X. Zhang, E. C. Brady, A. M. Haywood, A. N. LeGrande, D. J. Lunt, N. M. Mahowald, U. Mikolajewicz, K. H. Nisancioglu, B. L. Otto-Bliesner, H. Renssen, R. A. Tomas, Q. Zhang, A. Abe-Ouchi, P. J. Bartlein, J. Cao, Q. Li, G. Lohmann, R. Ohgaito, X. Shi, E. Volodin, K. Yoshida, X. Zhang, and W. Zheng, The PMIP4 contribution to CMIP6 – part 4: Scientific objectives and experimental design of the PMIP4-CMIP6

Last Glacial Maximum experiments and PMIP4 sensitivity experiments, *Geoscientific Model Development, 10*, 4035–4055, 2017.

Kaplan, M., J. Strelin, J. Schaefer, C. Peltier, M. Martini, E. Flores, G. Winckler, and R. Schwartz, Holocene glacier behavior around the northern Antarctic Peninsula and possible causes, *Earth and Planetary Science Letters, 534*, 116077, 2020.

Kim, S.-J., J. Lü, and B. M. Kim, The Southern Annular Mode (SAM) in PMIP2 simulations of the Last Glacial Maximum, *Advances in Atmospheric Sciences, 31*, 863–878, 2014.

Legrand, M., S. Preunkert, E. Wolff, R. Weller, B. Jourdain, and D. Wagenbach, Year-round records of bulk and size-segregated aerosol composition in central Antarctica (Concordia site) – part 1: Fractionation of sea-salt particles, *Atmospheric Chemistry and Physics, 17*, 14039–14054, 2017.

Levine, J., X. Yang, A. Jones, and E. Wolff, Sea salt as an ice core proxy for past sea ice extent: A process-based model study, *Journal of Geophysical Research: Atmospheres, 119*, 5737–5756, 2014.

Lewis, E. R., and S. E. Schwartz, 2004, *Introduction*, Chapter 1, pp. 1–7. American Geophysical Union (AGU).

Lhuissier, H., and E. Villermaux, Bursting bubble aerosols, *Journal of Fluid Mechanics, 696*, 5–44, 2012.

Lin, S.-J., and R. B. Rood, An explicit flux-form semi-lagrangian shallow-water model on the sphere, *Quarterly Journal of the Royal Meteorological Society, 123*, 2477–2498, 1997.

Liu, S., C.-C. Liu, K. Froyd, G. Schill, D. Murphy, T. Bui, J. Dean-Day, B. Weinzierl, M. Dollner, G. Diskin, G. Chen, and R.-S. Gao, Sea spray aerosol concentration modulated by sea surface temperature, *Proceedings of the National Academy of Sciences, 118*, e2020583118, 2021.

lv, C., N. Tsona, and L. Du, Sea spray aerosol formation: Results on the role of different parameters and organic concentrations from bubble bursting experiments, *Chemosphere, 252*, 126456, 2020.

Maciel, P., T. Quintino, U. Modigliani, P. Dando, B. Raoult, W. Deconinck, F. Rathgeber, and C. Simarro, The new ECMWF interpolation package MIR, *ECMWF newsletter, 152*, 36–39, 2017.

Mann, G., P. Anderson, and S. Mobbs, Profile measurements of blowing snow at Halley, Antarctica, *Journal of Geophysical Research, 105*, 24491–24508, 2000.

Matsui, H., D. Hamilton, and N. Mahowald, Black carbon radiative effects highly sensitive to emitted particle size when resolving mixing-state diversity, *Nature Communications, 9*, 3446, 2018.

Monahan, E., D. Spiel, and K. Davidson, 1986, *A Model of Marine Aerosol Generation Via Whitecaps and Wave Disruption*, pp. 167–174. Springer Dordrecht.

Murphy, D., K. Froyd, H. Bian, C. Brock, J. Dibb, J. DiGangi, G. Diskin, M. Dollner, A. Kupc, E. Scheuer, G. Schill, B. Weinzierl, C. Williamson, and P. Yu, The distribution of sea-salt aerosol in the global troposphere, *Atmospheric Chemistry and Physics, 19*, 4093–4104, 2019.

Myhre, G., D. Shindell, F.-M. Bréon, W. Collins, J. Fuglestvedt, J. Huang, D. Koch, J.-F. Lamarque, D. Lee, B. Mendoza, T. Nakajima, A. Robock, G. Stephens, T. Takemura, and H. Zhang, Anthropogenic and natural radiative forcing, in *Climate Change 2013: The Physical Science Basis. Contribution of Working Group I to the Fifth Assessment Report of the Intergovernmental Panel on Climate Change*, edited by T. Stocker, D. Qin, G.-K. Plattner, M. Tignor, S. Allen, J. Boschung, A. Nauels, Y. Xia, V. Bex, and P. Midgley, Book section 8, pp. 659–740, Cambridge University Press, Cambridge, United Kingdom and New York, NY, USA, 2013.

Neale, R. B., A. Gettelman, S. Park, A. J. Conley, D. Kinnison, D. Marsh, A. K. Smith, F. Vitt, H. Morrison, P. Cameron-Smith, W. D. Collins, et al., 2010, Description of the NCAR Community Atmosphere Model (CAM 5.0), Tech. Note NCAR/TN-486+STR, Technical report, National Center for Atmospheric Research (NCAR), USA.

Obbard, R., H. Roscoe, E. Wolff, and H. Atkinson, Frost flower surface area and chemistry as a function of salinity and temperature, *Journal of Geophysical Research, 114*, D20305, 2009.

O'Dowd, C., and G. de Leeuw, Marine aerosol production: A review of the current knowledge, *Philosophical transactions. Series A, Mathematical, physical, and engineering sciences, 365*, 1753–1774, 2007.

Oleson, K. W., D. M. Lawrence, G. B, M. G. Flanner, E. Kluzek, P. J, S. Levis, S. C. Swenson, E. Thornton, J. Feddema, C. L. Heald, et al., Technical description of version 4.0 of the Community Land Model (CLM), *National Center for Atmospheric Research, Tech. Rep.*, Boulder, Colorado, USA, 2010.

Park, T.-W., Y. Deng, M. Cai, J.-H. Jeong, and Z. Renjun, A dissection of the surface temperature biases in the Community Earth System Model, *Climate Dynamics, 43*, 1–17, 2013.

Peltier, W., D. Argus, and R. Drummond, Space geodesy constrains ice age terminal deglaciation: The global ICE-6G_C (VM5a) model, *Journal of Geophysical Research: Solid Earth, 120*, 450–487, 2014.

Perovich, D. K., and J. A. Richter-Menge, Surface characteristics of lead ice, *Journal of Geophysical Research: Oceans, 99*, 16341–16350, 1994.

Petit, J.-R., J. Jouzel, D. Raynaud, N. Barkov, J.-M. Barnola, I. Basile-Doelsch, M. Bender, J. Chappellaz, M. Davis, G. Delaygue, M. Delmotte, V. Kotlyakov, M. Legrand, V. Lipenkov, C. Lorius, L. Pepin, C. Ritz, E. Saltzman, and M. Stieve-

nard, Climate and atmospheric history of the past 420,000 years from the Vostok ice core, Antarctica, *Nature, 399*, 429–436, 1999.

Petterssen, S., Weather analysis and forecasting, a textbook on synoptic meteorology, *Quarterly Journal of the Royal Meteorological Society, 67*, 205–206, 1941.

Petty, C., Sea salt aerosols, *Goddard Space Flight Center, Tech. Rep.*, Greenbelt, Maryland, US, Online at https://svs.gsfc.nasa.gov/10390; accessed 14-March-2022, 2009.

Prijith, S., M. Aloysius, and M. Mohan, Relationship between wind speed and sea salt aerosol production: A new approach, *Journal of Atmospheric and Solar-Terrestrial Physics, 108*, 34–40, 2013.

Rankin, A., and E. Wolff, A year-long record of size-segregated aerosol composition at Halley, Antartica, *Journal of Geophysical Research, 108*, DJ03993, 2003.

Reynhout, S. A., E. A. Sagredo, M. R. Kaplan, J. C. Aravena, M. A. Martini, P. I. Moreno, M. Rojas, R. Schwartz, and J. M. Schaefer, Holocene glacier fluctuations in Patagonia are modulated by summer insolation intensity and paced by Southern Annular Mode-like variability, *Quaternary Science Reviews, 220*, 178–187, 2019.

Rhodes, R., X. Yang, E. Wolff, J. Mcconnell, and M. Frey, Sea ice as a source of sea salt aerosol to Greenland ice cores: A model-based study, *Atmospheric Chemistry and Physics, 17*, 9417–9433, 2017.

Richter, D., and F. Veron, Ocean spray: An outsized influence on weather and climate, *Physics Today, 69*, 34–39, 2016.

Riffenburgh, B., Antarctica and the Arctic circle: A geographic encyclopedia of the Earth's polar regions, *Polar Record, 51*, 463–464, 2014.

Roscoe, H., B. Brooks, A. Jackson, M. Smith, S. Walker, R. Obbard, and E. Wolff, Frost flowers in the laboratory: Growth, characteristics, aerosol, and the underlying sea ice, *Journal of Geophysical Research, 116*, D12301, 2011.

Roussel, M. L., F. Lemonnier, C. Genthon, and G. Krinner, Brief communication: Evaluating Antarctic precipitation in ERA5 and CMIP6 against CloudSat observations, *The Cryosphere, 14*, 2715–2727, 2020.

Saral, A., *Gravity Settlers - Performance Models*, Yıldız Technical University, Istanbul, 2018.

Schüpbach, S., H. Fischer, M. Bigler, T. Erhardt, G. Gfeller, D. Leuenberger, O. Mini, R. Mulvaney, N. Abram, L. Fleet, M. Frey, E. Thomas, A. Svensson, D. Dahl-Jensen, E. Kettner, H. Kjær, I. Seierstad, J. Steffensen, S. Rasmussen, and E. Wolff, Greenland records of aerosol source and atmospheric lifetime changes from the Eemian to the Holocene, *Nature Communications, 9*, 1–10, 2018.

Silvestri, G., A. Berman, P. Braconnot, and O. Marti, Long-term trends in the Southern Annular Mode from transient Mid- to Late Holocene simulation with the IPSL-CM5A2 climate model, *Climate Dynamics, 59*, 903–914, 2022.

Smith, R., and P. Gent, The Parallel Ocean Program (POP) reference manual, *Los Alamos Unclassified Report LA-UR-02-2484,*, 68–100, 2010.

Stohl, A., The Flextra Trajectory Model Version 3.0 user guide, pp. 1–19, 2000.

Stohl, A., and H. Sodemann, Characteristics of atmospheric transport into the Antarctic troposphere, *Journal of Geophysical Research, 115*, D02305, 2010.

Stohl, A., G. Wotawa, P. Seibert, and H. kromp kolb, Interpolation errors in wind fields as a function of spatial and temporal resolution and their impact on different types of kinematic trajectories, *Journal of Applied Meteorology, 34*, 2149–2165, 1995.

Thomas, M., A. Devasthale, and M. Kahnert, Marine aerosol properties over the Southern Ocean in relation to the wintertime meteorological conditions, *Atmospheric Chemistry and Physics, 22*, 119–137, 2022.

Trewby, M., *Antarctica: An encyclopedia from Abbott Ice Shelf to zooplankton*, Firefly Books, Toronto, 2002.

Veron, F., Ocean spray, *Annual Review of Fluid Mechanics, 47*, 507–538, 2015.

Veron, F., C. Hopkins, E. Harrison, and J. Mueller, Sea spray spume droplet production in high wind speeds, *Geophysical Research Letters, 39*, L16602, 2012.

Wagner, T., B. Dix, C. von Friedeburg, U. Frieß, S. Sanghavi, R. Sinreich, and U. Platt, MAX-DOAS O4 measurements: A new technique to derive information on atmospheric aerosols—principles and information content, *Journal of Geophysical Research, 109*, D22205, 2004.

Wang, H., A. R. Klekociuk, W. J. R. French, S. P. Alexander, and T. A. Warner, Measurements of cloud radiative effect across the Southern Ocean (43° S–79° S, 63° E–158° W), *Atmosphere, 11*, 949, 2020.

Weller, R., and D. Wagenbach, Year-round chemical aerosol records in continental Antarctica obtained by automatic samplings, *Tellus B, 59*, 755–765, 2007.

Weller, R., D. Wagenbach, M. Legrand, C. Elsässer, X. Tian-Kunze, and G. König-Langlo, Continuous 25-yr aerosol records at coastal Antarctica - I: Inter-annual variability of ionic compounds links to climate indices, *Tellus B: Chemical and Physical Meteorology, 63*, 901 – 919, 2011.

Werner, M., M. Heimann, and G. Hoffmann, Isotopic composition and origin of polar precipitation in present and glacial climate simulations, *Tellus B: Chemical and Physical Meteorology, 53*, 53–71, 2001.

Wikipedia contributors, 2022a, Dome C - Wikipedia, the free encyclopedia, Online at https://en.wikipedia.org/w/index.php?title=Dome_C&oldid=1076302669; accessed 14-March-2022.

Wikipedia contributors, 2022b, Frost flower (sea ice) - Wikipedia, the free encyclopedia, Online at https://en.wikipedia.org/w/index.php?title=Frost_flower_(sea_ice)&oldid=1074668972; accessed 24-June-2022.

Wolff, E., H. Fischer, F. Fundel, U. Ruth, B. Twarloh, G. Littot, R. Mulvaney, R. Röthlisberger, M. Angelis, C. Boutron, M. Hansson, U. Jonsell, M. Hutterli, F. Lambert, P. Kaufmann, B. Stauffer, T. Stocker, J. Steffensen, M. Bigler, and V. Gaspari, Southern Ocean sea-ice extent, productivity and iron flux over the past eight glacial cycles, *Nature, 440*, 491–496, 2006.

Wu, Z., Q. Yin, Z. Guo, and A. Berger, Comparison of Arctic and Southern Ocean sea ice between the last nine interglacials and the future, *Climate Dynamics, 59*, 519–529, 2022.

Xu, L., L. Russell, and S. Burrows, Potential sea salt aerosol sources from frost flowers in the pan-Arctic region: Salt aerosol sources from frost flowers, *Journal of Geophysical Research: Atmospheres, 121*, 10,840–10,856, 2016.

Yang, Q., R. C. Easter, P. Campuzano-Jost, J. L. Jimenez, J. D. Fast, S. J. Ghan, H. Wang, L. K. Berg, M. C. Barth, Y. Liu, M. B. Shrivastava, B. Singh, H. Morrison, J. Fan, C. L. Ziegler, M. Bela, E. Apel, G. S. Diskin, T. Mikoviny, and A. Wisthaler, Aerosol transport and wet scavenging in deep convective clouds: A case study and model evaluation using a multiple passive tracer analysis approach, *Journal of Geophysical Research: Atmospheres, 120*, 8448–8468, 2015.

Yoav, L., I. Koren, E. Boss, B.-A. Y, and O. Altaratz, Estimating the maritime component of aerosol optical depth and its dependency on surface wind speed using satellite data, *Atmospheric Chemistry and Physics, 10*, 6711–6720, 2010.

Yu, Q.-R., F. Zhang, J. Li, and J. Zhang, Analysis of sea-salt aerosol size distributions in radiative transfer, *Journal of Aerosol Science, 129*, 71–86, 2019.

Zíková, N., and V. Ždímal, Precipitation scavenging of aerosol particles at a rural site in the Czech Republic, *Tellus B: Chemical and Physical Meteorology, 68*, 27343, 2016.

Declaration of consent

on the basis of Article 30 of the RSL Phil.-nat. 18

Name/First Name: Bühler, Linnea

Registration Number: 20-120-317

Study program: M.Sc. Climate Sciences

Bachelor ☐ Master ☑ Dissertation ☐

Title of the thesis: Source Regions of Sea Salt Aerosols in Dome C Under Present Day and Last Glacial Maximum Conditions

Supervisor: Prof. Dr. C. C. Raible
Prof. Dr. H. Fischer

I declare herewith that this thesis is my own work and that I have not used any sources other than those stated. I have indicated the adoption of quotations as well as thoughts taken from other authors as such in the thesis. I am aware that the Senate pursuant to Article 36 paragraph 1 litera r of the University Act of 5 September, 1996 is authorized to revoke the title awarded on the basis of this thesis.
For the purposes of evaluation and verification of compliance with the declaration of originality and the regulations governing plagiarism, I hereby grant the University of Bern the right to process my personal data and to perform the acts of use this requires, in particular, to reproduce the written thesis and to store it permanently in a database, and to use said database, or to make said database available, to enable comparison with future theses submitted by others.

Köln, 17.04.2023

Place/Date

Signature